Gesellschaft für Anlagen- und Reaktorsicherheit (GRS) mbH

Modelling of Field-Scale Pollutant Transport

Final Report

GRS - 231

Gesellschaft für Anlagen- und Reaktorsicherheit (GRS) mbH

Modelling of Field-Scale Pollutant Transport

Final Report

Eckhard Fein
Klaus Peter Kröhn
Ulrich Noseck
Anke Schneider

August 2008

Remark:

This report was prepared under contract No. 02 E 9934 with the Federal Ministry of Economics and Technology (BMWi).

The work was conducted by the Gesellschaft für Anlagen- und Reaktorsicherheit (GRS) mbH.

The authors are responsible for the content of this report.

GRS - 231
ISBN 978-3-939355-05-2

Deskriptoren:

Computer Code, Dichteströmung, Modellierung, pH-Wert, Schadstofftransport, Salzwasserintrusion, Sorption, Strömung, Umweltbelastung

Abstract

Both software packages d^{3}f and r^{3}t are suited for the modelling of field-scale problems in density-driven flow and pollutant transport, respectively. Both utilise the most advanced numerical algorithms like adaptive grids controlled by a-posteriori error estimators, multigrid techniques, and can be run on workstations, PC-clusters, and massively parallel computers. The objective of this project was to demonstrate the manageability and the validity of both codes.

To this end four different test cases were modelled applying a large part of the capabilities of d^{3}f and r^{3}t. For instance the test cases were concerned with modelling of almost stagnant flow regimes, of pH-dependent adsorption, of non-constant degradation rates as function of other pollutants. In one case stochastic flow modelling was required. Nevertheless each test case demanded both flow and transport modelling.

The first test case deals with a freshwater lens below the East Frisian Island of Langeoog. Besides the transport of chloride and potassium the scenario of inundation and its consequences for the freshwater lens was examined. In this case it was harked back to data collected by the Technical University of Braunschweig.

In the second test case data gathered at the Krauthausen test site operated by the Jülich research centre, North Rhine-Westphalia, were used. Here the transport of uranine, lithium, and bromide was determined. The flow was modelled stochastically, while non-linear sorption isotherms were taken into consideration for uranine and lithium.

The third test case dealt with the zinc transport at a sewage plant at Cape Cod, Massachusetts, USA. There was evidence that the zinc transport depends on pH-values. Hence both zinc and hydrogen transport was modelled and sorption of zinc as a function of the hydrogen concentration was analysed.

The fourth test case addressed the problem of gasoline spills. Ethanol serves as additive to gasoline and suppresses the anaerobic biodegradation of benzene. Therefore the degradations (decay) rate of benzene has to be modelled in dependence on the ethanol concentration. This capability was newly integrated into r^{3}t. The Borden site in Canada was selected as example for a highly permeable sandy aquifer in which the migration of water-soluble contaminants is increased due to increased flow and de-

creased sorption of the contaminant onto sands relative to clay and organic matter-rich sediments /GLE 99/.

Contents

1 Introduction

In the course of long-term safety analyses for repositories for radioactive waste in deep geological formations the burden to the biosphere due to potential releases of pollutants is assessed for relevant scenarios. The migration of pollutants from the repository to man is divided into three almost independent parts: the near field, the far field, and the biosphere. For long-term safety assessments of entire repository systems one employs in Germany the software package EMOS /STO 96/. By use of the EMOS code a repository system can be handled both deterministically and probabilistically. It comprises modules to simulate the near field, the far field, and the biosphere.

In long-term safety analyses carried out so far the transport of pollutants through the far field was simulated one-dimensionally. The reason was that the available computer codes were not able to consider every relevant retention effect for large sites three-dimensionally. One-dimensional transport modelling requires the determination of the appropriate migration path from three-dimensional velocity fields with particle tracking techniques. In the simulations of transport along representative, one-dimensional migrations paths radioactive decay, longitudinal dispersion and retention by adsorption were considered beside advection and diffusion. To this end linear as well as non-linear sorption isotherms were used.

To simulate the above described one-dimensional transport of pollutants through the far field the modules CHET (**CHE**mie und **T**ransport) /KÜH 96/, /LÜH 96/, and TRAPIC (**TRA**nsport of **P**ollutants **I**nfluenced by **C**olloids) /LÜH 98/, /LÜH 99/ were available. Due to modelling the migration path one-dimensionally dilution was taken into account in a simplified way. In doing so the concentration-dependent (non-linear) sorption and precipitation processes were in particular reproduced inadequately.

In order to overcome such deficiencies the software package r^3t was recently developed within the framework of the BMWA-funded project “Entwicklung eines Programms zur dreidimensionalen Modellierung des Schadstofftransportes” /FEI 04/. The objective was to allow simulations of pollutant transport through large and heterogeneous areas over long time periods.

Until now the newly developed computer code r^3t has only been used to perform easy test case simulations. The results were compared with well-known analytical solutions.

Additionally easy and small-scaled problems were attacked. In the present final report of the project “Modelling of Field-Scale Pollutant Transport (MOST)”, results of applications of d^3f and r^3t to realistic problems are given. Here numerous options for modelling provided within d^3f and r^3t were used with actual hardware from workstations to massively parallel computers.

2 Overall Task

2.1 State of Science and Technology

In the framework of deterministic and probabilistic long-term safety analyses the computer code EMOS /STO 96/ is used. Using pollutant release from the near field calculated with EMOS, pollutant transport through the far field and subsequent radiation exposures in the biosphere can be simulated. For the one-dimensional transport through the far field the modules CHETLIN /KÜH 96/ and CHETLIN /LÜH 96/ are applied, whereas the code TRAPIC /LÜH 98/, /LÜH 99/ is used for colloidal transport. By virtue of the one- or two-dimensional modelling the dilution of pollutants is only approximately described. Hence the concentration-dependent sorption and precipitation processes are reproduced inadequately.

In long-term safety analyses performed in other countries the transport through the far field was generally simulated with one-dimensional transport models, cf. /NAG 94/. Depending on the host formation the applied computer codes were adapted both for porous /GOO 94/ and for fractured media /NAG 94/, /SKI 91/, /SVE 92/, /VIE 92/, /VIE 96/. Each code considered advective and dispersive/diffusive transport as well as linear sorption and radioactive decay even allowing for nuclear decay chains. The codes for fractured media were based on double-porosity models and additionally considered matrix diffusion.

The two-dimensional pollution transport modelling was performed for the WIPP site /DOE 96/. Due to in comparison to one-dimensional simulations increased computing times probabilistic transport was not simulated for each relevant nuclide but only for one radionuclide. The radiation exposures of the remaining radionuclides were deduced from these single nuclide results.

In the recently developed computer code r^3t /FEI 04/ the geometrical resolution of heterogeneities was obtained by application of unstructured grids and effective solver algorithms as it was the case in the density-driven flow model d^3f (**d**istributed **d**ensity **d**riven **f**low) /FEI 99/. For both codes adaptive procedures controlled by a-posteriori error estimators were developed, whereby the calculation grid is locally refined or coarsened according to the proceeding physical processes. Again the new effective solving

algorithms can be applied to linear and as well as to non-linear problems even on parallel computer architectures.

In the course of the project „Entwicklung eines Programms zur dreidimensionalen Modellierung des Schadstofftransportes" /FEI 04/ first test simulations were performed on the basis of standard problems with well-known analytical solutions in order to verify the r^3t code.

2.2 Subgoals

During the processing of the test cases each time the following works were performed:

- data acquisition for the geometrical and hydrogeological characterisation of the modelled areas,
- generation of two- and three-dimensional geometrical models with a level of abstraction as far as possible,
- implementation of hydrogeological and retention parameters,
- configuration of the solver algorithms,
- performing of two- and three-dimensional flow simulations,
- subsequent two- and three-dimensional transport modelling if required first for non-sorbing and second for sorbing pollutants,
- the comparison with measured values or external modelling results (where applicable),
- parameter variations,
- calculations using refined grids to check the numerical results,
- graphical conditioning, analyses and interpretation of results, and
- checking the results by plausibility.

In the following the four test cases will be roughly described.

2.2.1 Chloride and Potassium Transport at the Langeoog Island

For most islands monitoring and protection of the water quality of freshwater lenses are a fundamental part of the social security. Hence recently one tries to better understand the behaviour of freshwater lenses by performing model simulations. At the Institute of

Environmental Geology of the Technical University of Braunschweig a structural model of the aquifer system of the Langeoog Island was set-up. Measured data, which form the model basis /PET 03/ were used within this project.

2.2.2 Pollutant Transport at the Krauthausen Groundwater Measuring Field

The examined aquifer consists of three layers with different hydraulic conductivities and different clay contents /VER 00/. The region is hydrogeologically very well characterised. The tracer experiments considered here are performed with uranine, lithium, and bromide. The first two are reactive tracers while the last one is an ideal one. The tracers were injected through inoculation wells. The propagation of the tracers was monitored over a period of approximately 1.25 y. The retardation of uranine and lithium is non-linear and can be described with Freundlich isotherms. The parameters of the isotherm were defined with data from batch experiments performed at FZ Jülich. Since the sorption behaviour depends on clay content, the Freundlich parameters are different for the different layers.

2.2.3 Zinc Transport in the Vicinity of Cape Cod, Massachusetts

Since nearly 60 years sewage effluent emanating from a sewage treatment facility that serves the Massachusetts Military Reservation contaminated a near surface aquifer /KEN 00/. Only in December 1995 the pollution was stopped after implementation of a new plant. The spatial and temporal spreading of the pollutant plume is well known from a dense grid of measuring points. Non-reactive components of the plume were found even at a distance of 5 500 m from the source and in a depth of about 30 m. In contrast to that zinc was detected only at a distance of approximately 400 m and even in a 2 m to 4 m thick zone at the surface of the plume. In lower lying domains zinc has migrated less than 100 m. Moreover, it penetrated only up to 15 m in depth. This different and locally limited propagation is caused by pH-dependent sorption processes.

2.2.4 Benzene Transport and Biodegradation at the Borden Site

Methyl tertiary-butyl ether (MTBE) and ethanol are used as gasoline additives to replace the lead as an octane-enhancing additive and to reduce the reliance on oil imports. Environmental hazards come from oil production sites and underground storage

tanks, respectively. During gasoline spills among others benzene is released. Benzene is known to be carcinogen and implies health risks. The potential for ethanol to decrease the biodegradation of BTEX either by serving as a preferred substrate or through the release of acetic acid during ethanol metabolism requires additional considerations. Therefore transport modelling was carried out to anticipate the consequences of ethanol on the biodegradation and transport of benzene through contaminated aquifers.

3 Software Used

Throughout this project the computer codes d^3f for flow and r^3t for contaminant transport simulations were used. Both codes are specially developed to model large three-dimensional regions with complex geometries over long time periods. The hydrogeology of the modelled area can comprise strong heterogeneities and anisotropies. The basic prerequisites for use are:

- the porous media are fluid saturated,
- the aquifer systems are confined,
- the porous media and the fluid are incompressible.

Both computer codes consist of three parts: the preprocessors, the simulators and the postprocessor. The latter is identical for both program packages and is based on the GRAPE software /RUM 90/, /GRA 94/. It is designed to analyse and to plot the results of the simulations. The task of the preprocessors is the preparation of the input data, which itself consists of two different parts: the data describing the model, and the data controlling the numerical algorithms. The model data are subsumed in five and seven different files, respectively. In case of d^3f these are: geometry, hydrogeology, initial, boundary, and source, whereas the input files for r^3t are: geometry, pollutant, retention, initial, boundary, flow, and sourceterm. The controlling of the simulator is managed by script files which can be altered by means of an interactive graphical user interface. The simulators of d^3f and r^3t are based on the numerical library UG (unstructured Grids) /BAS 97/. The UG library comprises robust solvers for numerical simulations on hierarchical grid structures. These multigrid solvers were used successfully in d^3f as well as in r^3t. All numerical algorithms applied for solving density-driven flow or radionuclide transport problems are based on finite volume methods. Together with an appropriate discretisation of boundary conditions, all numerical schemes meet the condition of mass preserving on a local and a global level. In case of r^3t the decay reactions can be described by very high decay rates that result in impracticable restrictions on the size of time steps. To overcome this difficulty, the exact solution of ordinary differential equations describing the decay reactions was implemented. Too long time steps may yield unphysical oscillations in numerical solutions. To overcome such situations, a new second-order explicit discretisation scheme for the convection equation with flux limiter was developed and implemented. This method was extended, together with a special local flux limiter to avoid unphysical oscillations for unstructured grids as required by r^3t.

Even if the reaction equations are solved exactly, they can only be combined by means of the so-called “operator splitting approach”. This works very well if the two involved operators commute. For systems of convection equations with extremely different retardation factors coupled by decay reactions, large time splitting errors can occur. So a new explicit second-order discretisation method was developed and implemented for this type of equations.

A new flux-based method of characteristics for the convection-dominated transport, and later on also for coupled systems of convection equations was developed and implemented. Moreover, the flux-based method of characteristics for systems of transport equations includes in a natural way the treatment of decay reactions, avoiding the time splitting error of standard operator splitting methods.

The computational results of d^{3}f in form of data describing the velocity and the density fields can be directly saved within d^{3}f. Afterwards, they can be imported by r^{3}t and used for the numerical modelling of the convective transport of radionuclides.

In the following both programs are briefly described.

3.1 Density Driven Flow and Pollutant Transport

The transport modelling of radionuclides (pollutants) shall be valid for potential flow as well as for density driven flow. The notation used is described in chapter 0. Density driven flow is described by the following equations, the flow equation and the equation for the transport of salt /FEI 99/:

$$\frac{\partial}{\partial t}\ \phi\rho_f\ +\nabla\cdot\ \boldsymbol{q}\rho_f\ =s_f \qquad (3.1)$$

$$\frac{\partial}{\partial t}\ \phi\rho_f\chi_s\ +\nabla\cdot\ \boldsymbol{q}\rho_f\chi_s-\boldsymbol{D}_s\rho_f\nabla\chi_s\ =s_s \qquad (3.2)$$

Similarly the transport of pollutants with negligible impact on fluid density is described by:

$$\frac{\partial}{\partial t}\ \phi\rho_f\chi_i\ +\nabla\cdot\ \boldsymbol{q}\rho_f\chi_i-\boldsymbol{D}\rho_f\nabla\chi_i\ =Q_i \qquad (3.3)$$

3.1.1 Definition of Concentrations

Different ways to define concentrations are valid. The most important used in connection with the modelling of radionuclide (pollutant) transport based on density driven flow are compiled in this section.

The mass m_i of i^{th} pollutant is given by:

$$m_i = n_i \cdot M_i \quad \text{kg}$$

where n_i is the mole number and M_i is the molecular weight.

The fluid density ρ_f in which salt and pollutants j are dissolved is stated as

$$\rho_f = \frac{m_{NaCl} + m_{H_2O} + \sum_j m_j}{V_{por}} \left[\text{mol m}^{-3}\right]$$

If the impact of dissolved pollutants on the fluid density ρ_f is negligible the fluid density is:

$$\rho_f \approx \frac{m_{NaCl} + m_{H_2O}}{V_{por}} \left[\text{mol m}^{-3}\right]$$

The mass fraction of the component i is given by:

$$\chi_i = \frac{m_i}{m_{NaCl} + m_{H_2O} + \sum_j m_j} \approx \frac{m_i}{m_{NaCl} + m_{H_2O}} \quad \left[\text{kg kg}^{-1}\right]$$

The concentration of the radionuclide i referred to the pore volume reads

$$\sigma_i = \frac{m_i}{V_{por}} = \rho_f \cdot \chi_i \quad \left[\text{kg m}^{-3}\right]$$

or:

$$C_i = \frac{n_i}{V_{por}} \quad \left[\text{mol m}^{-3}\right]$$

From that the following relation between $\chi_i, C_i,$ and σ_i arises:

$$C_i = \frac{\sigma_i}{M_i} = \rho_f \frac{\chi_i}{M_i} \quad \left[\text{mol m}^{-3}\right]$$

In an analogous manner one obtains the concentration C_i^{ad} for a sorbed pollutant from the bulk density ρ_{rock} and the mass fraction χ_i^{ad} of the pollutant i relating to the rock mass:

$$\rho_{rock} = \frac{m_r}{V_{rock}} \quad \left[\text{kg m}^{-3}\right]$$

and

$$\chi_i^{ad} = \frac{m_i^{ad}}{m_r + \sum_j m_j^{ad}} \approx \frac{m_i^{ad}}{m_r} \quad \left[\text{kg kg}^{-1}\right]$$

$$\sigma_i^{ad} = \frac{1-\phi}{\phi} \rho_{rock} \chi_i^{ad} = \frac{m_i^{ad}}{V_{rock}} \quad \left[\text{kg m}^{-3}\right]$$

In d^{3}f for any time relative salt concentrations are used:

$$C = C_{rel} = \frac{C_s}{C_{s,\max}} \quad \text{with} \quad C_s = \frac{m_s}{m_s + m_{H_2O}} \qquad (3.4)$$

3.2 Flow Modelling Using the Code d^{3}f

Density-driven flow is described by the time-dependent partial differential equations (3.1) for fluid flow and (3.2) for salt transport /FEI 99/. The salt content governs the density and the dynamical viscosity of the fluid. Both can be modelled as arbitrary functions of the salt concentration. These fluid properties again are influencing the flow. Hence both equations are coupled.

It is assumed that Darcy's law is valid:

$$\boldsymbol{q} = -\frac{\boldsymbol{k}}{\mu}\,\nabla p - \rho_f \boldsymbol{g} \quad \text{where} \quad \begin{matrix} \rho_f = \rho_f\ C_s \\ \mu = \mu\ C_s \end{matrix} \qquad (3.5)$$

Here $\boldsymbol{q}$ is the Darcy (apparent) velocity, $\boldsymbol{k}$ the permeability tensor, μ the dynamical viscosity of the fluid, p the hydrodynamic pressure, ρ_f the fluid density and $\boldsymbol{g}$ the gravitation vector.

As already described in eq. (3.4) relative salt concentrations are used so that always $0 \le C_s \le 1$ is valid. There exist some predefined functions to describe the fluid density and dynamical viscosity of NaCl solution, but the user is free to define other appropriate relations.

Hydrodynamic dispersion is expressed by Scheidegger's approximation

$$\boldsymbol{D} = |\boldsymbol{q}|\,\alpha_T \boldsymbol{I} + \frac{\alpha_L - \alpha_T}{|\boldsymbol{q}|}\boldsymbol{q}\boldsymbol{q}^T \qquad (3.6)$$

Here $|\boldsymbol{q}|$ denotes the absolute value of Darcy's velocity and $\boldsymbol{q}^T$ the transposed velocity vector, so that $\boldsymbol{q}\boldsymbol{q}^T$ stands for the dyadic product. α_L and α_T are the longitudinal and transversal dispersion lengths, respectively. Permeability and porosity can be modelled either as constants, or as temporal or spatial functions. In addition permeability can be isotropic or anisotropic and stochastic, respectively.

3.3 Transport Modelling Using the Code r^{3}t

The transport of radioactive or chemical pollutants through porous or equivalent-porous media is described by time-dependent partial differential equations. In addition to transport processes these equations characterise first-order reactions, for instance radioactive decay, chemical and biological degradation and kinetically controlled sorption. By the description of these reactions the appropriate differential equations are generally non-linearly coupled. Equilibrium sorption as well as kinetically controlled sorption can be applied. In both cases isotherms after Henry, Langmuir, and Freundlich can be used, respectively. Additional options are immobile pore waters after Coats-Smith and

element-specific solubility limits. It is assumed that the distribution in the various phases (solved, adsorbed and precipitated) will not be affected by the radioactive decay and degradation processes, respectively. That means that no additional coupling between the phases exists.

Allowing for precipitation and sorption one ends up with

$$\frac{\partial}{\partial t}\left(\phi\rho_f \chi_i^l + \phi\rho_f \chi_i^p + \phi\frac{1-\phi}{\phi}\rho_{rock}\chi_i^{ad} \right) + \nabla\cdot\ \boldsymbol{q}\rho_f \chi_i^l - \boldsymbol{D}\rho_f \nabla\chi_i^l \ = Q_i \qquad (3.7)$$

If the source or sink terms $\bar{Q}_i$ are given with dimension [mol m^{-3} s^{-1}] it has the form

$$\bar{Q}_i = \bar{Q}_i^d - \lambda_i\phi C_i + \sum_{k\ i}\lambda_k\phi C_k \qquad (3.8)$$

With the aid of the flow equation (3.1) the transport equation (3.2) can be converted.

$$\begin{aligned} &\phi\rho_f \frac{\partial}{\partial t}\chi_i^l + \frac{\partial}{\partial t}\left(\phi\rho_f \chi_i^p + \phi\frac{1-\phi}{\phi}\rho_{rock}\chi_i^{ad} \right) \\ &\quad + \boldsymbol{q}\rho_f \nabla\chi_i^l - \nabla\boldsymbol{D}\rho_f \nabla\chi_i^l = Q_i \end{aligned} \qquad (3.9)$$

In order to combine equations (3.8) and (3.9) they must have the same units. For practical reasons the unit mol m^{-3} is chosen. Dividing by the molecular weight M_i and by appropriate expansion with ρ_f equation (3.9) can be converted to:

$$\begin{aligned} &\phi\rho_f \frac{\partial}{\partial t}\left(\frac{1}{\rho_f}\frac{\chi_i^l}{M_i}\rho_f \right) + \frac{\partial}{\partial t}\left(\phi\frac{\rho_f \chi_i^p}{M_i} + \phi\frac{1-\phi}{\phi}\rho_{rock}\frac{\chi_i^{ad}}{M_i} \right) \\ &+\boldsymbol{q}\rho_f \nabla\left(\frac{1}{\rho_f}\frac{\chi_i^l \rho_f}{M_i} \right) - \nabla\boldsymbol{D}\rho_f \nabla\left(\frac{1}{\rho_f}\frac{\chi_i^l \rho_f}{M_i} \right) \\ &= \frac{Q_i}{M_i} \end{aligned} \qquad (3.10)$$

With $C_i^l = \rho_f \frac{\chi_i^l}{M_i}$, $C_i^p = \rho_f \frac{\chi_i^p}{M_i}$, $C_i^{ad} = \frac{\chi_i^{ad}}{M_i}$, and $\tilde{Q}_i = \frac{Q_i}{M_i}$ one gets

$$\begin{aligned}
&\phi\rho_f \frac{\partial}{\partial t}\left(\frac{1}{\rho_f} C_i^l\right) + \frac{\partial}{\partial t}\left(\phi C_i^p + \phi \frac{1-\phi}{\phi} \rho_{rock} C_i^{ad}\right) \\
&+\boldsymbol{q}\rho_f \nabla\left(\frac{1}{\rho_f} C_i^l\right) - \nabla \boldsymbol{D} \rho_f \nabla\left(\frac{1}{\rho_f} C_i^l\right) \\
&= \tilde{Q}_i
\end{aligned} \qquad (3.11)$$

Finally, taking into account the immobile part of pollutants the coupled transport equations for N radionuclides (pollutants) read:

$$\begin{aligned}
&\phi\rho_f \frac{\partial}{\partial t}\left(\frac{1}{\rho_f} C_i^l\right) + \frac{\partial}{\partial t}\left(\phi C_i^p + g\phi \frac{1-\phi-\phi_{im}}{\phi} \rho_{rock} C_i^{ad}\right) \\
&+\boldsymbol{q}\rho_f \nabla\left(\frac{1}{\rho_f} C_i^l\right) - \nabla\left(\boldsymbol{D}\rho_f \nabla\left(\frac{1}{\rho_f} C_i^l\right)\right) \\
&= -\lambda_i \left(\phi C_i^l + \phi C_i^p + g\phi \frac{1-\phi-\phi_{im}}{\phi} \rho_{rock} C_i^{ad}\right) \\
&+\sum_{k\ i} \lambda_k \left(\phi C_k^l + \phi C_k^p + g \frac{1-\phi-\phi_{im}}{\phi} \rho_{rock} C_k^{ad}\right) \\
&-\alpha^{e\ i}\ \ C_i^l - G_i^l \\
&+\tilde{Q}_i^d
\end{aligned} \qquad (3.12)$$

3.3.1 Diffusion and Dispersion

$\boldsymbol{D}$ denotes the tensor of diffusion and dispersion. In general it is composed of the element-specific molecular diffusion coefficient and the dispersion tensor. Analogue to d^{3}f Scheidegger's approach is used.

$$\boldsymbol{D}^{e\ i} = \phi D_m^{e\ i} \boldsymbol{I} + \alpha_T |\boldsymbol{q}| \boldsymbol{I} + \frac{\alpha_L - \alpha_T}{|\boldsymbol{q}|} \boldsymbol{q}\boldsymbol{q} \qquad (3.13)$$

3.3.2 Equilibrium Sorption

Equilibrium sorption is expressed element-specifically with isotherms.

$$C_i^{ad} = K_d^{e\ i} C_i^l \qquad \textbf{Henry} \qquad (3.14)$$

$$C_i^{ad} = \frac{b\kappa}{1 + bC_{e\,i}^{l}} C_i^{l} \qquad \textbf{Langmuir} \qquad (3.15)$$

$$C_i^{ad} = K_{nl} \left(C_{e\,i}^{l} \right)^{p-1} C_i^{l} \qquad \textbf{Freundlich} \qquad (3.16)$$

Relating to the isotherm after Freundlich attention should be paid to the fact that formally the term $\left(C_{e\,i}^{l} \right)^{p-1}$ has to be dimensionless. It is achieved by formally dividing through the appropriate unit of concentration but with tacit understanding this will never be expressed in the formulae.

With an appropriate $K^{e\,i} \left(C_{e\,i}^{l} \right)$ all of the three isotherms can be expressed as follows:

$$C_i^{ad} = K^{e\,i} \left(C_{e\,i}^{l} \right) C_i^{l} \qquad (3.17)$$

Each of the parameters in equations (3.14) through (3.17) is element specific.

In the case of equilibrium sorption a so-called retardation factor R_f can be defined, as long as flow conservation is not explicitly taken into account.

$$R_f = 1 + \frac{1-\phi}{\phi} \rho_{rock} K^{e\,i} \left(C_{e\,i}^{l} \right) \qquad (3.18)$$

3.3.3 Kinetically Controlled Sorption

In analogy to equilibrium sorption the following formulations for kinetically controlled sorption are used:

Henry

$$\frac{\partial}{\partial t} C_i^{ad} = k_{\alpha}^{e\,i} \left(K_d^{e\,i} C_i^{l} - C_i^{ad} \right) - \lambda_i C_i^{ad} + \sum_k \lambda_k C_k^{ad} \qquad (3.19)$$

Langmuir

$$\frac{\partial}{\partial t} C_i^{ad} = k_\alpha^{e\,i} \left(\frac{b\kappa}{1 + bC_{e\,i}^{l}} C_i^{l} - C_i^{ad} \right) - \lambda_i C_i^{ad} + \sum_k \lambda_k C_k^{ad} \qquad (3.20)$$

Freundlich

$$\frac{\partial}{\partial t} C_i^{ad} = k_\alpha^{e\,i} \left(K_{nl} \; C_{e\,i}^{l} \;^{p-1} C_i^{l} - C_i^{ad} \right) - \lambda_i C_i^{ad} + \sum_k \lambda_k C_k^{ad} \qquad (3.21)$$

It is assumed that radioactive decay does not affect the phases of the radionuclides (solved, adsorbed and precipitated).

3.3.4 Precipitation

If the concentration of an element $C_{e\,i}^{l}$ exceeds the element-specific solubility limit $L^{e\,i}$ the pollutant precipitates as long as the concentration of the element reaches the element-specific solubility limit. Accordingly the concentration C_i^p of the precipitated pollutant increases. On the other hand, when the concentration of the element $C_{e\,i}^{l}$ falls below the element-specific solubility limit $L^{e\,i}$, the pollutant dissolves.

$$\left.\begin{array}{l} C_{e\,i}^{l} \le L^{e\,i} \\ C_{e\,i}^{l} > L^{e\,i} \end{array}\right\} \Rightarrow \quad C_i^p = \begin{cases} 0 \\ \dfrac{C_i^l}{C_{e\,i}^{l}} \; C_{e\,i}^{l} - L^{e\,i} \end{cases}$$

and (3.22)

$$\left.\begin{array}{l} C_{e\,i}^{l} \le L^{e\,i} \\ C_{e\,i}^{l} > L^{e\,i} \end{array}\right\} \Rightarrow \quad C_i^l = \begin{cases} C_i^l \\ \dfrac{C_i^l}{C_{e\,i}^{l}} L^{e\,i} \end{cases}$$

3.3.5 Immobile Pore Water

If pores filled with immobile water exist, pollutants possibly can intrude and be adsorbed. Instead of matrix diffusion which can be modelled by effective sorption parameters the approach after Coats-Smith /COA 64/ has been used. It yields a much better agreement with experimental results, especially for the description of the tailing

/DAW 98/. The approach after Coats-Smith is described by the local concentration difference between mobile and immobile pore space.

$$\begin{aligned}&\frac{\partial}{\partial t}\left(\phi_{im}G_i^l + (1-g)(1-\phi-\phi_{im})\rho_{rock}G_i^{ad}\right)\\&= \alpha^{e\,i}\left(C_i^l - G_i^l\right) - \lambda_i\left(\phi_{im}G_i^l + (1-g)(1-\phi-\phi_{im})\rho_{rock}G_i^{ad}\right)\\&+ \sum_{k\,i}\lambda_k\left(\phi_{im}G_k^l + (1-g)(1-\phi-\phi_{im})\rho_{rock}G_k^{ad}\right)\end{aligned} \qquad (3.23)$$

3.3.6 Impact of Complexing Agents

There exist substances which affect sorption features and solubility limits if they are dissolved in ground water. They are called complexing agents. Only the K_d-coefficients and solubility limits L are allowed to be modified by complexing agents.

$$K_d^{e\,i}\left(C^1,\ldots,C^M\right) = K_d^{e\,i}\, f\left(C^1,\ldots,C^M\right) \qquad (3.24)$$

$$L^{e\,i}\left(C^1,\ldots,C^M\right) = L^{e\,i}\, h\left(C^1,\ldots,C^M\right) \qquad (3.25)$$

where $f(0) = h(0) = 1$.

The functional dependency on the concentration of the complexing agents is limited to simple functions, like step functions, power series, rational functions, exponentials, etc. Here the concentrations $C^1, C^2, \ldots, C^M$ describe the concentration of M complexing agents and not the concentrations of pollutants.

Agents can enter into the modelled area on different ways:

- by release from mine workings (analogue to pollutants),
- by release from a special source,
- as initial concentration distribution which is transported,
- as instantaneous, constant concentration distribution independent of time.

3.4 Initial and Boundary Conditions

To obtain unique solutions of eqs. (3.1) to (3.3) it is essential to define besides the equations and the parameters for flow and transport initial and boundary conditions for pressure and salt concentration and on the other hand for pollutant concentration.

3.4.1 Initial conditions

For flow modelling the initial salt concentration $C_s \ \boldsymbol{x}, t \ \big|_{t=t_0}$ has to be given, whereas the hydrostatic pressure $p^0 \ \boldsymbol{x}, t \ \big|_{t=t_0}$ as second condition is consistently determined by the initial salt concentration.

In case of pollutants transport again initial conditions $C_i^l \ \boldsymbol{x}, t \ \big|_{t=t_0}$ have to be specified for N pollutants and, if required for M complexing agents $i = 1, \ldots, N+M$. If kinetically controlled sorption or immobile pore water regions are modelled, corresponding initial conditions $C_i^{ad} \ \boldsymbol{x}, t \ \big|_{t=t_0}$ and $G_i^l \ \boldsymbol{x}, t \ \big|_{t=t_0}$ have to be given. In order to avoid the presetting of N+M separate initial conditions, first of all initial conditions are fixed which are valid for each pollutant and agent. Subsequently for individual substances exceptions can be defined. The sequence of input is $C_i^l \ \boldsymbol{x}, t \ \big|_{t=t_0}$, $C_i^{ad} \ \boldsymbol{x}, t \ \big|_{t=t_0}$ and $G_i^l \ \boldsymbol{x}, t \ \big|_{t=t_0}$. It is assumed that in the area of immobile pore water always equilibrium sorption is valid. In the case of precipitation it is assumed that the initial concentration of precipitated substances is always zero.

3.4.2 Boundary Conditions

Boundary conditions have to be defined piecewise for d3f as well as for r3t. Pieces of the boundary can be boundary lines and boundary areas of singular hydrogeological units or even parts of it like intervals. Boundary conditions must be defined for each segment of the boundary. If they are not explicitly defined, it is assumed that the corresponding segment of the boundary is impermeable for advective flow and for diffusive/dispersive transport.

3.4.2.1 Boundary Conditions for Density-Driven Flow

Boundary conditions have to be given for pressure and salt concentration to solve eqs. (3.1) and (3.2). They can be time independent or transient.

3.4.2.1.1 Pressure Boundary Conditions (d^{3}f)

The following boundary conditions can be defined for **pressure**:

– Dirichlet Boundary Condition

The pressure $p\ \ x,t\ \big|_{x\in\Gamma_i}$ is given at the surface Γ_i of the modelled area.

$$p\ \ \boldsymbol{x},t\ \big|_{\boldsymbol{x}\in\Gamma_i} = f\ \ \boldsymbol{x},t\ \Big|_{\boldsymbol{x}\in\Gamma_i} \quad \text{Ps} \qquad (3.26)$$

where $f\ \ x,t$ is constant or a function of space and/or time.

– Neumann Boundary Condition

The mass flux $\rho\ \ \boldsymbol{x},t\ \ \boldsymbol{n}\cdot\boldsymbol{q}\ \ \boldsymbol{x},t\ \big|_{x\in\Gamma_i}$ is given at the surface Γ_i of the modelled area.

$$\rho\boldsymbol{n}\cdot\boldsymbol{q}\big|_{\boldsymbol{x}\in\Gamma_i} = f\ \ \boldsymbol{x},t\ \Big|_{\boldsymbol{x}\in\Gamma_i} \quad \left[\text{kg m}^{-2}\,\text{s}^{-1}\right] \qquad (3.27)$$

where $f\ \ x,t$ is constant or a function of space and/or time.

– Normal Component of Velocity with Respect to Boundary

The mass-averaged Darcy-velocity $\rho\boldsymbol{n}\cdot\boldsymbol{q}\big|_{\boldsymbol{x}\in\Gamma_i}$ perpendicular to the surface Γ_i of the modelled area is given

$$\rho\boldsymbol{n}\cdot\boldsymbol{q}\big|_{\boldsymbol{x}\in\Gamma_i} = \rho f\ \ \boldsymbol{x},t\ \Big|_{\boldsymbol{x}\in\Gamma_i} \quad \left[\text{kg m}^{-2}\,\text{s}^{-1}\right] \qquad (3.28)$$

where $f\ \ x,t$ again is constant or a function of space and/or time.

– No Volume Flow over Boundary

This boundary condition is useful in modelling salt inflow into a modelled region without volume change. This is primarily important for models whose boundaries are completely impermeable. It is defined as

$$\rho \boldsymbol{n} \cdot \boldsymbol{q}\big|_{\boldsymbol{x}\in\Gamma_i} = -\boldsymbol{n} \cdot \left(\boldsymbol{D}_m + \boldsymbol{D}\right) \nabla\rho \; C \,\big|_{\boldsymbol{x}\in\Gamma_i} = -\rho' \; C \; \boldsymbol{n} \cdot \left(\boldsymbol{D}_m + \boldsymbol{D}\right) \nabla C\big|_{\boldsymbol{x}\in\Gamma_i} \quad (3.29)$$
$$\Leftrightarrow \boldsymbol{n} \cdot \boldsymbol{v}_V\big|_{\boldsymbol{x}\in\Gamma_i} = 0$$

where $\boldsymbol{v}_V := \left(\boldsymbol{q} + \left(\boldsymbol{D} + \boldsymbol{D}_m\right) \frac{\nabla\rho}{\rho}\right)$ is the volume velocity.

3.4.2.1.2 Salt Concentration Boundary Conditions (d³f)

The following boundary conditions may be defined for salt concentration:

– **Dirichlet Boundary Condition**

The concentration $C\left(x,t\right)\big|_{x\in\Gamma_j}$ is given at the surface Γ_j by

$$C_s\left(\boldsymbol{x},t\right)\big|_{\boldsymbol{x}\in\Gamma_i} = f\left(\boldsymbol{x},t\right)\big|_{\boldsymbol{x}\in\Gamma_i} \quad - \quad (3.30)$$

where $f\left(x,t\right)$ is constant or a function of space and/or time.

– **Neumann Boundary Condition**

The mass flux $\rho \boldsymbol{n} \cdot \left(\boldsymbol{q} C_s - \left(\boldsymbol{D}_m + \boldsymbol{D}\right) \nabla C_s\right)\big|_{\boldsymbol{x}\in\Gamma_i}$ is defined as

$$\rho \boldsymbol{n} \cdot \left(\boldsymbol{q} C_s - \left(\boldsymbol{D}_m + \boldsymbol{D}\right) \nabla C_s\right)\big|_{\boldsymbol{x}\in\Gamma_i} = f\left(\boldsymbol{x},t\right)\big|_{\boldsymbol{x}\in\Gamma_i} \quad \left[\mathrm{kg\,m^{-2}\,s^{-1}}\right] \quad (3.31)$$

where $f\left(x,t\right)$ is constant or a function of space and/or time.

– Leaching Boundary Condition

This boundary condition fixes the total flux of salt over the boundary Γ_i to be proportional to the difference of the actual concentration and some reference concentration $C_i^{l,ref}$. This is the common formulation of leaching. Thereby the reference concentration corresponds to the particular solubility limit of pollutant i. The constant α_i^d is the so-called leaching constant. This boundary condition is described by

$$\rho \boldsymbol{n} \cdot \left(\boldsymbol{q} C_s - \left(\boldsymbol{D}_m + \boldsymbol{D} \right) \nabla C_s \right) \Big|_{\boldsymbol{x} \in \Gamma_i} = \alpha \left(\boldsymbol{x}, t \right) \left(C_s - C_s^{ref} \left(\boldsymbol{x}, t \right) \right) \Big|_{\boldsymbol{x} \in \Gamma_i} \qquad (3.32)$$

where $\alpha \left(\boldsymbol{x}, t \right)$ is the leaching constant and $C_s^{ref} \left(\boldsymbol{x}, t \right)$ is the salt concentration at the boundary segment.

– Outflow Boundary Condition (Disappearing of diffusiv/dispersive salt flow)

At an outflow boundary the diffusiv/dispersive flux across the boundary is fixed. The standard outflow boundary condition means that the diffusiv/dispersive flux is set to zero, while the pollutants are leaving the modelled area according to the actual concentration and flow velocity:

$$\begin{aligned} & -\rho \boldsymbol{n} \cdot \left(\boldsymbol{D}_m + \boldsymbol{D} \right) \nabla C_s \big|_{\boldsymbol{x} \in \Gamma_i} = 0 \\ & \Leftrightarrow \\ & \rho \boldsymbol{n} \cdot \left(\boldsymbol{q} C_s - \left(\boldsymbol{D}_m + \boldsymbol{D} \right) \nabla C_s \right) \Big|_{\boldsymbol{x} \in \Gamma_i} = \rho \boldsymbol{n} \cdot \boldsymbol{q} C_s \big|_{\boldsymbol{x} \in \Gamma_i} \end{aligned} \qquad (3.33)$$

– In- and Outflow Boundary Condition

This boundary condition switches between Dirichlet (inflow) and outflow boundary conditions dependent on the direction of velocity.

$$\begin{aligned} & C_s \left(\boldsymbol{x}, t \right) \big|_{\boldsymbol{x} \in \Gamma_i} = f \left(\boldsymbol{x}, t \right) \big|_{\boldsymbol{x} \in \Gamma_i} \\ & \rho \boldsymbol{n} \cdot \left(\boldsymbol{q} C_s - \left(\boldsymbol{D}_m + \boldsymbol{D} \right) \nabla C_s \right) \Big|_{\boldsymbol{x} \in \Gamma_i} = \rho \boldsymbol{n} \cdot \boldsymbol{q} C_s \big|_{\boldsymbol{x} \in \Gamma_i} \end{aligned} \quad \textbf{if} \quad \begin{aligned} & \boldsymbol{n} \cdot \boldsymbol{q} \big|_{\boldsymbol{x} \in \Gamma_i} < 0 \\ & \boldsymbol{n} \cdot \boldsymbol{q} \big|_{\boldsymbol{x} \in \Gamma_i} > 0 \end{aligned} \qquad (3.34)$$

Complete and precise descriptions can be found in /FEI 99/ and /BIR 00/.

3.4.2.1.3 Boundary Conditions for Pollutant Transport (r^3t)

Boundary conditions have to be fixed for N pollutants (nuclides) and, if they are modelled for M agents, too. In the case of kinetically controlled sorption or immobile pore water modelling the boundary conditions are identical to those of dissolved pollutants. One has to keep in mind that at every piece of the boundary the type of boundary conditions has to be equal for every substance. If no boundary conditions are explicitly given it is assumed that the diffusive/dispersive flux vanishes. This is done by flux boundary condition.

– Dirichlet Boundary Condition

The concentration $C_i \;\; x,t \;\big|_{x\in\Gamma_j}$ of pollutant i is given at the surface Γ_j by:

$$C_i^l \;\; x,t \;\big|_{\boldsymbol{x}\in\Gamma_j} = f_i \;\; x,t \;\big|_{\boldsymbol{x}\in\Gamma_j} \quad \left[\mathrm{mol\,m^{-3}}\right] \qquad (3.35)$$

where $f_i \;\; x,t$ is constant or a function of space and/or time for pollutant i.

– Flux Boundary Condition

The total flux of pollutant i over the boundary Γ_j is fixed by:

$$\boldsymbol{n}\rho_f \cdot \left[\boldsymbol{q}\frac{1}{\rho_f}C_i^l - \boldsymbol{D}\frac{1}{\rho_f}\nabla C_i^l\right]\Bigg|_{\boldsymbol{x}\in\Gamma_j} = f_i \;\; x,t \;\big|_{\boldsymbol{x}\in\Gamma_j} \quad \left[\mathrm{mol\,m^{-2}\,s^{-1}}\right] \qquad (3.36)$$

where $f_i \;\; x,t$ is constant or a function of space and/or time for pollutant i.

– Leaching Boundary Condition

This boundary condition fixes the total flux of pollutant i over the boundary Γ_j to be proportional to the difference of the actual concentration and some reference concentration $C_i^{l,ref}$. This is the common formulation of leaching. Here the reference concentration corresponds to the particular solubility limit of pollutant i. The constant α_i^d is the so-called leaching constant.

$$\boldsymbol{n}\rho_f \cdot \left[\boldsymbol{q} \frac{1}{\rho_f} C_i^l - \boldsymbol{D} \frac{1}{\rho_f} \nabla C_i^l \right]_{x \in \Gamma_j} \quad \left[\text{mol m}^{-2} \text{ s}^{-1} \right] \qquad (3.37)$$
$$= \alpha_i^d \left(C_i^l \left(x, t \right) - C_i^{l,ref} \right)$$

– Outflow Boundary Condition

For an outflow boundary the diffusiv/dispersive flux across a boundary is fixed. In this case various alternatives exist:

- Standard Outflow Boundary Condition

A standard outflow boundary condition means the diffusiv/dispersive flux is set to zero, while the salt is leaving the modelled area according to the actual concentration and flow velocity:

$$\boldsymbol{n}\rho_f \cdot \boldsymbol{D} \nabla \frac{1}{\rho_f} C_i^l \Big|_{x \in \Gamma_j} = 0 \quad \left[\text{mol m}^{-2} \text{ s}^{-1} \right] \qquad (3.38)$$

This is the usual outflow boundary condition. As long as no other boundary condition is given this standard outflow condition is valid.

– In- and Outflow Boundary Condition

$$\begin{aligned} & C_i^{in}\left(x, t \right) \Big|_{x \in \Gamma_j} && \boldsymbol{n} \cdot \boldsymbol{q} < 0 \\ & \qquad \text{if} \\ & \boldsymbol{n}\rho_f \cdot \boldsymbol{D} \nabla \frac{1}{\rho_f} C_i^l \Big|_{x \in \Gamma_j} = 0 && \boldsymbol{n} \cdot \boldsymbol{q} > 0 \end{aligned} \qquad (3.39)$$

For this boundary condition the flow simulation itself fixes the domains where different flow situations are valid. At the inflow domain $\boldsymbol{n} \cdot \boldsymbol{q} < 0$ one assumes that the inflowing fluid carries the concentration C_i^{in} while at the outflow domain $\boldsymbol{n} \cdot \boldsymbol{q} > 0$ the concentration gradient normal to the boundary is set to zero. The various fluxes are known but not the exact locations of turning points.

– Transmission Boundary Condition

The transmission boundary condition requires the total flux across the boundary to be constant /HÄF 92/.

$$\nabla \cdot \boldsymbol{D}\rho_f \nabla \frac{1}{\rho_f} C_i^l \quad x,t \Big|_{x \in \Gamma_j} = 0 \qquad (3.40)$$

Physically this boundary condition means that the internal advection-diffusion/dispersion flux continues across the boundary. The flux boundary condition (3.36) stipulates that the diffusive/dispersive flux vanishes across the boundary. Hence it is a special case of equation (3.40).

– Sources and Sinks

Since water inflow and outflow normally can be neglected sources and sinks are only defined for pollutants. If these neglects are improper one has also to take into consideration appropriate sources and/or sinks for water. This amount of water will modify the flow field.

Sources and sinks can have various geometrical shapes. They can be:

– points,
– lines,
  - parallel to axes,
  - arbitrarily orientated,
– quadrilateral surfaces (one axis $\perp$ to area),
– parallelepipeds (axes $\perp$ to lateral surface) or
– pieces of boundary (lines and surfaces, respectively).

The temporal characteristics are given by a rectangular distribution (cf. Fig. 3.1) or by the explicit declaration of the mass in- or outflow at a source or a sink at discrete times. Depending on the modelled time T_{Mod} and the inflow time T either δ-shaped or constant sources can be modelled.

$T_{Mod} >> T$ δ-shaped
$T_{Mod} = T$ constant

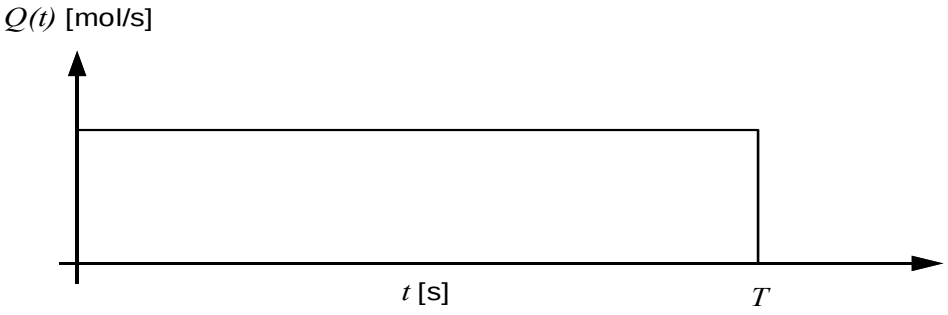

$$Q(t) = \begin{cases} \frac{Q_s}{T} & t \le T \\ 0 & t > T \end{cases} \quad \text{with} \quad \int Q(t)\,dt = Q_s$$

Fig. 3.1 Possible temporal distribution of pollutant inflow

For sources the pollutant rate $Q\ t$ [mol s^{-1}] is always given as

$$Q\ t = \int_{F\ \Gamma} \left(\boldsymbol{n}\rho_f \cdot \left[\boldsymbol{q}\frac{1}{\rho_f} C_i^l - \boldsymbol{D}\nabla \frac{1}{\rho_f} C_i^l \right] \right) df \quad \left[\text{mol}\,\text{s}^{-1}\right] \qquad (3.41)$$
$$= \int_{F\ \Gamma} h_i^{flux}\ x,t\ df$$

Here F is the surface which is attached to the boundary condition.

If the source is located at the boundary it can be modelled as a boundary condition. In that case the flux is given by

$$h_i^{flux}\ x,t \approx \frac{Q\ t}{F} \quad \left[\text{mol}\,\text{m}^{-2}\,\text{s}^{-1}\right] \qquad (3.42)$$

Equation (3.42) is exact only for a homogeneous flow field.

For every geometrical shape of sources and sinks first of all the patches are discriminated which overlap with the sources and sinks. According to the overlaps which are expressed as percentage the pollutants are distributed to the concerned patches. It is obvious that the initial grid has to consider the locations of sources and sinks. Otherwise the dilution of the pollutants will be overestimated. Complete and precise descriptions can be found in /FEI 04/

4 Modelling Freshwater Lenses at the Langeoog Island

Langeoog is one of the East Frisian Islands, located in the North Sea in the north-west of Germany. 1000 years ago all East Friesian islands were part of one large Island named Bant. They got their actual shapes only some 100 years ago.

Fig. 4.1: The Langeoog Island, geographical situation, see /SEL 02/

Langeoog extends over a length of 11 km and has an average width of about 2 km. In a depth up to 70 m tertiary melt water sands exist, covering the Lauenburg Clay. The island is characterised by a large glacial channel with Holocene watt and channel sediments with a thickness up to about 25 to 30 m. In the western and eastern part, the sands are superposed by watt sands with silty stratifications, overlaid by watt and dune sands up to the surface /NAU 05/.

According to geoelectrical data, the freshwater lens of Langeoog partially achieves a depth up to 30 meters and is divided into 3 parts. This fact is caused by numerous storm tides in the past. Today graded dune areas are found in some parts of the island like the Grosse and Kleine Schlopp. Due to the frequent storm tides in these lowlands the development of a freshwater lens was not possible. The Schlopp Lake within the Grosse Schlopp, a lake consisting of brackish water, has its origin not in storm tides but in sand mining.

Hydrogeological data, such as the amount of precipitation, groundwater levels, recharge, pumping rates and specific electric conductivity was taken from /NAU 05/ and /SEL 02/.

The modelled area includes the Pirola Valley in the central part of Langeoog (see Fig. 4.2). This valley is an important area for drinking water supply: 13 wells of the local waterworks are located in this plane, which is protected from the North Sea by a belt of dunes and dikes. During the last years, these dunes often have been damaged by storm tides.

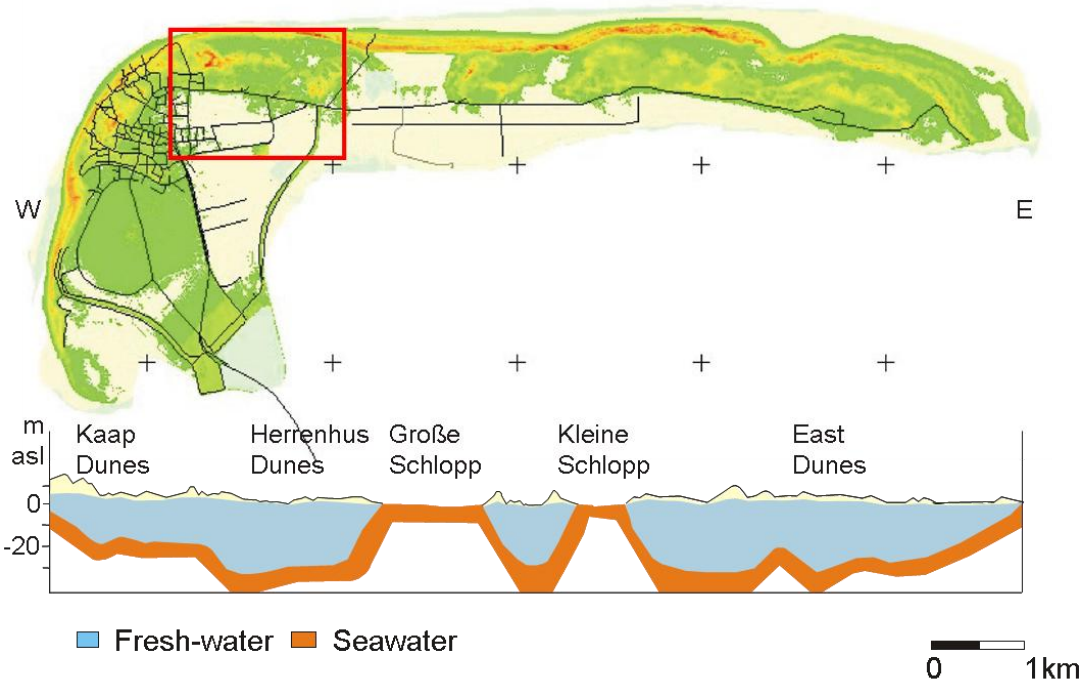

Fig. 4.2: The Langeoog island, model area (red), freshwater lens (/NAU 05/)

4.1 Hydrogeological model

The three-dimensional hydrogeological model was created using the software SURFER. It has an extension of 2 km x 1.4 km x 70 m (see Fig. 4.3). In a depth of 70 m the Lauenburg Clay is covered by melt water sands, overlaid by watt and dune sands with interbeddings of watt silt. At the top the model is limited by the groundwater level that varies from 1.20 m (sea-level) up to 2.04 m absolute altitude.

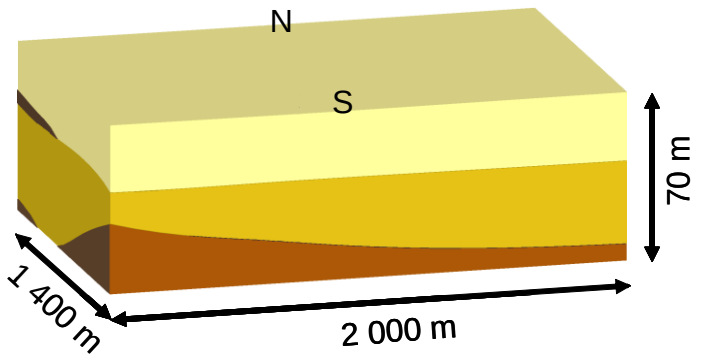

Fig. 4.3: Langeoog: three-dimensional model and its extensions

The Lauenburg clay is the lowest layer of the model. The permeabilities of watt and dune sands and silt were identified by grain-size analysis /NAU 05/. Different permeability and porosity values for the other layers were taken from literature /HÖL 05/. Dispersion coefficients are set to 10 m and 1 m, respectively, the diffusion constant is assumed to be 10^{-9} m² s^{-1}. Permeabilities and porosities used in the model are listed in Fig. 4.4.

Northwards the model is bounded by the North Sea, southwards by watt areas. The freshwater lens crops out towards the eastern boundary. The western boundary crosses the freshwater lens at a depth up to about 25 m.

watt and dune sands	k = $2.8 \cdot 10^{-11}$ m² Φ = 0.14
watt silt	k = $4.8 \cdot 10^{-13}$ m² Φ = 0.08
watt sand	k = $4.0 \cdot 10^{-11}$ m² Φ = 0.14
watt silt	k = $4.8 \cdot 10^{-13}$ m² Φ = 0.08
melt-water sands	k = $1.0 \cdot 10^{-10}$ m² Φ = 0.20
Lauenburger Clay	k = $1.0 \cdot 10^{-16}$ m² Φ = 0.250

Fig. 4.4: Langeoog model: hydrogeological units and parameters

The salt concentration in the North Sea is assumed to be 0.035 kg kg^{-1}, meaning at a temperature of 10 °C the seawater has a density of 1027 kg m^{-3} and a viscosity of $1.4 \cdot 10^{-3}$ kg m^{-1} s^{-1}.

The annual precipitation measured at the Langeoog weather station varies within 13 years (1989-2001) from 657 to 981 mm y^{-1}, the corrected precipitation from 880 to 1315 mm y^{-1}. The average is 724 mm y^{-1}, the average of the corrected values 970 mm y^{-1} /SEL 02/. For the neighbour island Norderney in /NAU 05/ it is given from 422 to 951 mm y^{-1} for 1991 to 2001 and additionally corrected values, varying from 481 to 1095 mm y^{-1}. The average is specified with 730 or 829 mm y^{-1}, respectively. Following /WOL 98/, on Norderney, the 30-year mean precipitation from 1966 to 1996 was 764 millimetres per year.

Groundwater recharge is known as a parameter that can be quantified with an accuracy of only about 30 % - based on the precipitation data. For Langeoog island recharge was calculated by /SEL 02/ according to different methods, such as Renger & Wessolek, Wendling and Grossmann. The average recharge is specified from 300 to 563 mm y^{-1}, the minimum value for the driest year with 235, the maximum for the year with the highest precipitations with 935 mm y^{-1}.

Because of the large interval of data assigned to this essential input parameter several computations were performed based on different average groundwater recharge rates.

4.2 Numerical Modelling – d³f simulations

At first the creation of the freshwater lens is modelled. As an initial condition the model domain is assumed to be completely filled with seawater. d³f works with relative concentrations, that means that a seawater salt concentration c_{abs} = 0.035 kg kg^{-1} is represented by the relative concentration c = c_{rel} = 1.

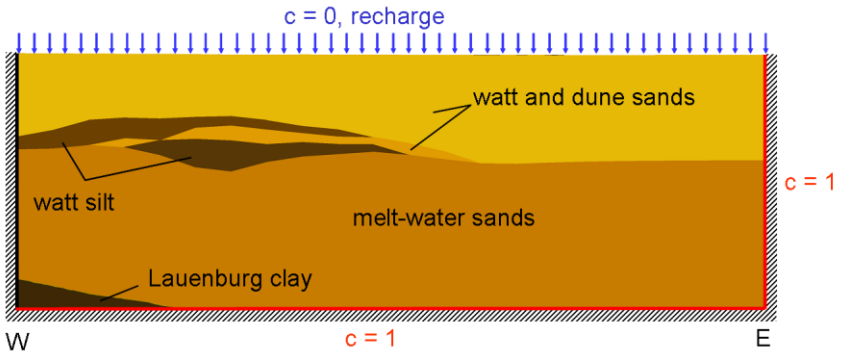

Fig. 4.5: Langeoog model: vertical cross section with boundary conditions

Density and viscosity are linear functions of the concentration, so the density varies from 1000 kg m^{-3} for c = 0 to 1027 kg m^{-3} for c = 1, the viscosity from $1.0 \cdot 10^{-3}$ to $1.25 \cdot 10^{-3}$ kg m^{-1} s^{-1}, analogously.

The bottom and the eastern and western boundary of the model are assumed to be impermeable (see Fig. 4.5). Hydrostatic pressure conditions are defined for the southern and northern boundary below sea level. At the island's surface, the boundary condition for the pressure is defined in form of an inflow velocity which corresponds to the groundwater recharge rates, and the concentration is assumed to be c = 0. A Neumann condition for the concentration is assigned to the western boundary, meaning there is no salt mass transport across this boundary. For all other vertical boundaries below sea level the concentration is set to c = 1, above sea level c = 0.

For the results shown here, the recharge rate was set to 700 mm y^{-1}. The simulations are performed on a hexahedron coarse grid with 1,364 nodes. It was created by D. Feuchter of the University of Heidelberg. To compute the creation of the freshwater lens, the grid is uniformly refined to 65,000 and 500,000 nodes, respectively. The calculations are performed sequentially on PCs. After a model time of about 50 years a velocity field and a concentration distribution are obtained which are quasi steady-state. Concentration and velocity fields on a vertical cross section are shown in Fig. 4.6.

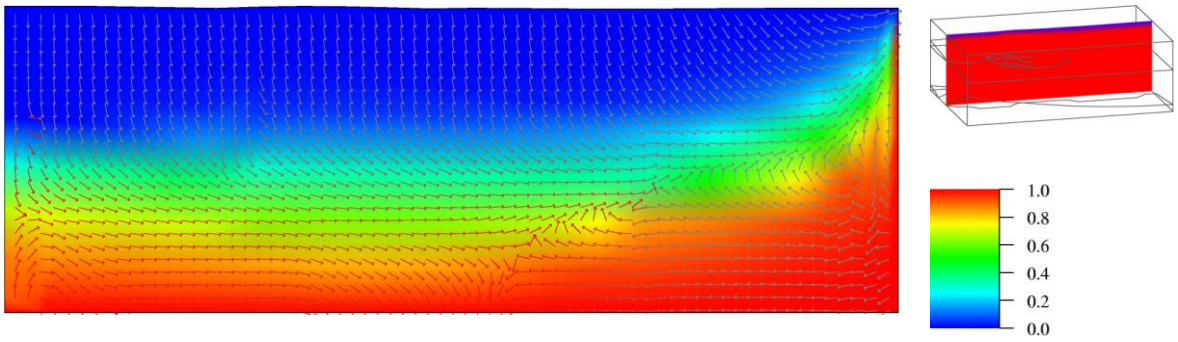

Fig. 4.6: Vertical cross section (E-W): steady state concentration and velocity

In Germany, the limiting value for salt concentration in potable water is 1 g dm^{-3} /GRU 00/, which corresponds to a relative concentration of 0.028. Accordingly a freshwater lens with a depth up to 25 m was computed. The shape of the calculated freshwater lens corresponds to the measurements. In the eastern part the lens forms a transition zone of brackish water (see Fig. 4.7). However, the lens does not reach the

measured depths of 30 m below sea level, but it reaches the surfaces of the watt silt layers as described in /NAU 05/.

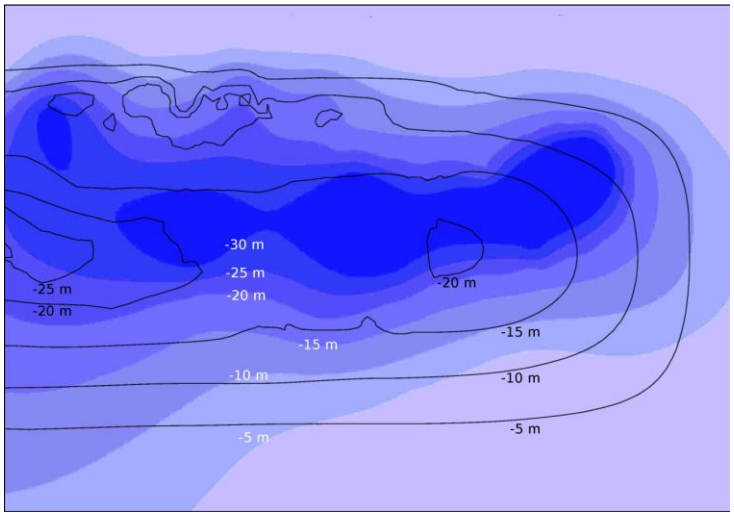

Fig. 4.7: Contour lines of the fresh-water/seawater interface
shaded blue: measured depth of the fresh-water lens
black lines: depth calculated by d^3f

To point out the reasons for the differences, several variations of parameters and boundary conditions have been performed. Modifications of permeabilities, porosities, density, boundary conditions at the vertical boundaries have almost no effects, while varying the groundwater recharge rates has a direct, noticeable impact on the depth of the freshwater lens. To reach a depth of 30 m, one has to suppose recharge rates of more than 1000 mm y^{-1}. Using rates of 300 mm y^{-1}, as suggested by /WOL 04/, the simulated lens has only a depth of about 10 to 15 m.

It cannot be excluded that one reason for the differences is the unavailability of tools to model free water tables in d^3f. On the other hand, the hydrogeological situation is known only from 26 boreholes. And finally it is not impossible that the precision of geoelectrical measurements is not sufficient – in addition to the fact that the measurements were performed in 1995, during a period of extremely high precipitation rates. Taking into account these uncertainties and the bandwith of possible recharge rates, the calculations with a recharge rate of 700 mm y^{-1} are taken as a basis for the further investigations within this chapter. One has to keep in mind that this value is relatively high. Regarding all the uncertainties, one can resume that the coincidence of the measured and the simulated seawater/freshwater interface is satisfactory.

4.3 Modelling Chloride and Potassium Transport with r³t

With the objective of verifying the plausibility of r³t-results compared with d³f, in a second step the transport of Cl^- and K^+ Ions is simulated using r³t, based on the d³f velocity-field. The chloride concentration in the North Sea water is 557 mol m^{-3}. As an initial condition the model domain is completely filled with seawater. Seawater concentration is assigned to the bottom and all vertical boundaries except of the western one (see Fig. 4.8). It is supposed that the steady-state result for chloride transport corresponds to the concentration field computed by d³f. The right part of Fig. 4.8 shows a comparison of both results with a very good correspondence of the seawater/freshwater interface.

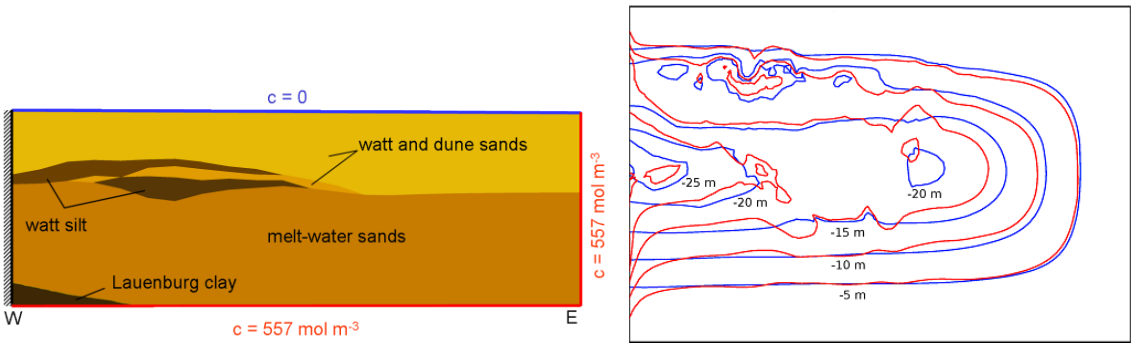

Fig. 4.8: Chloride transport
left: boundary conditions
right: contour lines of fresh /seawater interface blue: d3f, red: r3t

The potassium transport is simulated analogically to the chloride transport. The initial potassium concentration is 9.63 mol m^{-3}. While chloride is not retarded, a weak equilibrium sorption is assumed for the potassium. Therefore the Henry isotherm with $c^{ad} = K_d \cdot c^l$ is used, where c^{ad} is the adsorbed concentration and c^l the concentration in solution. The boundary conditions and K_d-values are shown in Fig. 4.9. Comparing the steady-state results for the interface in Fig. 4.9 (right picture) the contour lines show an almost complete consistence.

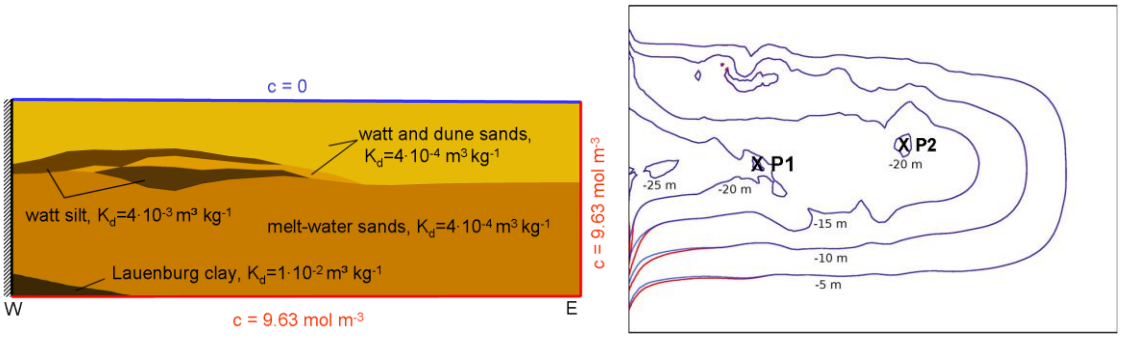

Fig. 4.9: Potassium transport
Left: boundary conditions and Kd-values
Right: contour lines of fresh-water/seawater interface; red: Cl^-, blue: K^+

A comparison of the time-dependent concentrations of Cl^- and K^+ at the two points P1 (depth: 25 m) and P2 (depth: 20 m) given in Fig. 4.9 is depicted in Fig. 4.10. In watt and dune sands the retardation factor of potassium should have a value of about 6. Obviously, in our simulations the potassium transport in both points is retarded by a factor of the same order of magnitude.

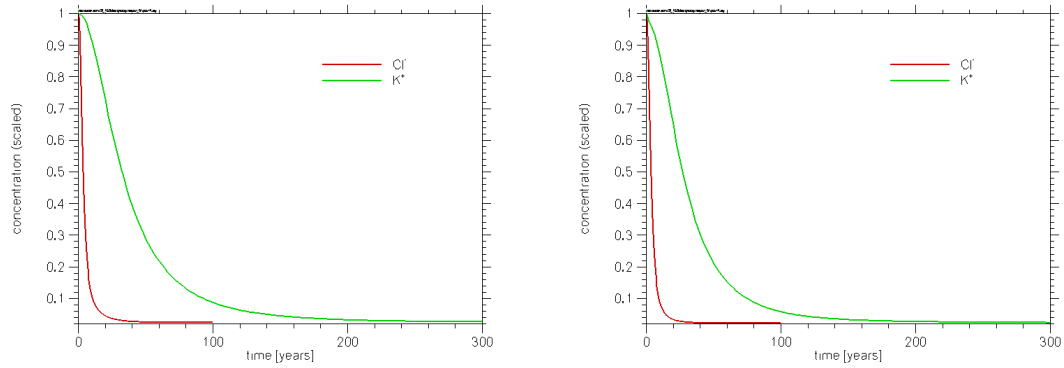

Fig. 4.10: Time-dependent concentrations of Cl^- and K^+ at P1 (left) and P2 (right)

4.4 Flood Scenario

The last step is the simulation of a seawater break through scenario created by the OOWV (Oldenburg-East-Friesian Water Association), see /WOL 04/. In this scenario the groundwater catchment area of the eastern waterworks is flooded. The valleys denoted with A 101 and A 102 in Fig. 4.11 have different properties: Area 101, the central Pirola Valley, is a region protected by large dunes and dikes, with the adverse effect, that these dikes hinder a fast seawater run-off after a storm tide. Area 102, the southern valley, is not bordered by dikes, and the seawater can easily run off. A connection between the two areas is given by a small valley, which could easily be truncated by a dike.

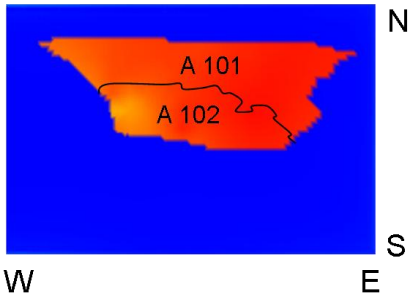

Fig. 4.11: Location of the flooded areas

The scenario is based on the following assumptions: The area 101 is flooded up to a height of 4.50 m. Forced by pumping using the existing wells, the water table decreases to 3 m within 6 days. For a period of 48 hours the situation remains unchanged. 80 days after the flood event the surface will be free of seawater. The area 102 is flooded to 3.20 m, but only while the water table of A 101 is higher than 3.50 m. In the following the seawater is completely disappeared after 48 hours.

In the saturated zone, seepage velocities of $2.0 \cdot 10^{-8}$ to $5.5 \cdot 10^{-8}$ m s^{-1} are suggested /WOL 04/. These velocities and seawater concentration are used as boundary conditions within the areas A 101 and A 102 – decreasing corresponding to the water table.

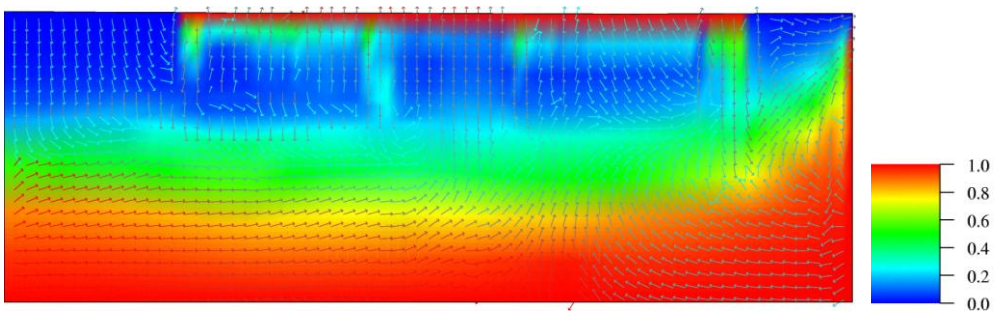

Fig. 4.12: Saltwater intrusion at the end of the flooding period

Fig. 4.12 shows the concentration in a vertical cross section 80 days after the flood event. In evidence a strong fingering and the existence of convection cells are noticeable, and the brackish water zone is remarkably enlarged. In Fig. 4.13 the seawater/fresh-water interface is shown. Obviously, the freshwater lens is damaged by the seawater break through until a depth of about 20 m. As can be seen in the vertical cross section, it takes more than 10 years until the freshwater lens is completely restored.

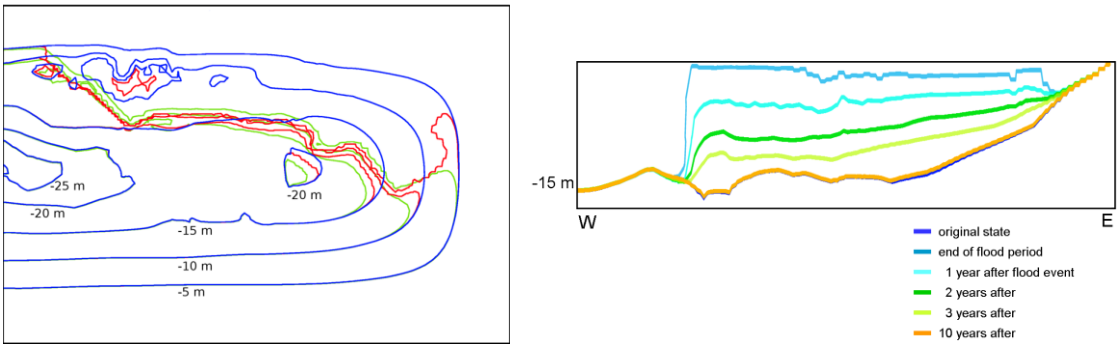

Fig. 4.13: Seawater/freshwater interface, contour lines
left: blue = original; red = end of flooding period; green = one year later
right: vertical cross section (see legend)

4.5 Modelling of Pumping

Initially it was planned to include the pumping wells of the Pirola Valley into the model. Although a previous attempt of modelling wells using d^3f /FEI 99/ was successful, in this case the small depth of the modelled system shows the limitation in modelling wells without the possibility of modelling free water tables. In the actual case, after start of pumping, the upconing was much too strong. Tests with reduced pumping rates provided no satisfying results, too. Possibly wells can only be modelled by the actual d^3f-code, if the aquifer thickness and the depth of the freshwater lens, respectively, are sufficiently large.

Hence we did not succeed in these modelling efforts and have to advert to forthcoming projects. We will repeat these simulations and use it as a test case, when d^3f will be enhanced and enabled to perform free surface modelling.

4.6 Conclusions

The simulations show that modelling of seawater intrusion and pollutant transport in three-dimensional heterogeneous porous media is possible with d^3f and r^3t. The freshwater lens simulations and the saltwater intrusion scenario performed using d^3f gave satisfactory, plausible results. The results of transport modelling with the help of r^3t agree with the salt transport computed with d^3f. The retardation of potassium transport works as expected. That means that at least d^3f- and r^3t-modelling are consistent.

5 The Krauthausen Test Site

5.1 Introduction

The Krauthausen test site is located in North Rhine-Westphalia, Germany, approximately 7 km southeast from the Jülich Research Centre and is a part of the Jülicher Zwischenscholle area, cf. Fig. 5.1. The site was established in 1993 within the framework of the EU project "Critical parameters governing the mobility and fate of pesticides in soil/aquifer systems: An experimental and modelling study based on coherent interpretation of transport parameters and physicochemical characteristics measured at multiple scales" /DÖR 97/.

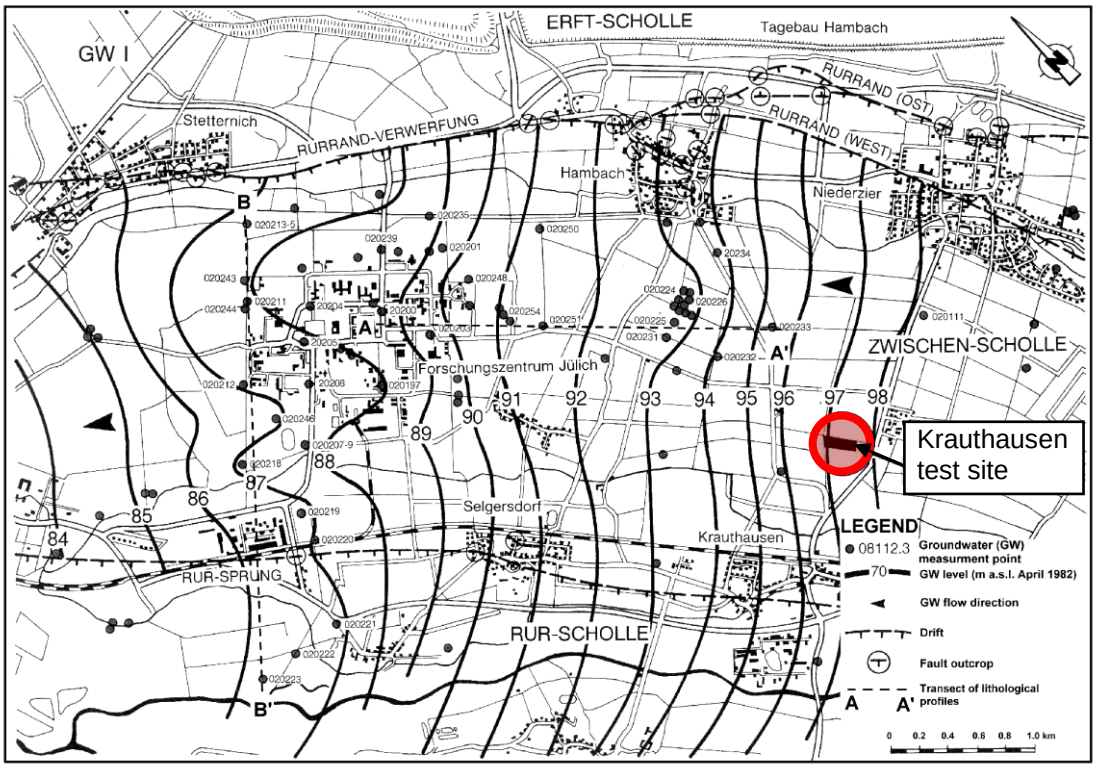

Fig. 5.1: Hydrogeological map of the Jülich area /CIO 01/
The Krauthausen test site is marked in red.

Since that time experiments were conducted to examine groundwater flow and solute transport. The Krauthausen test site covers an area of 200 m × 70 m. A geological profile was generated on the basis of the findings of four drillings which were sunk to a depth of 15 m to 20 m, cf. /VER 00/. The local basis of the uppermost highest aquifer is located at a depth of 9 m to 10 m and consists of clay with a thickness some decime-

tres. This aquifer is limited by flood plain deposits at the top and, as aforementioned, a clay layer at the bottom, cf. Fig. 5.2.

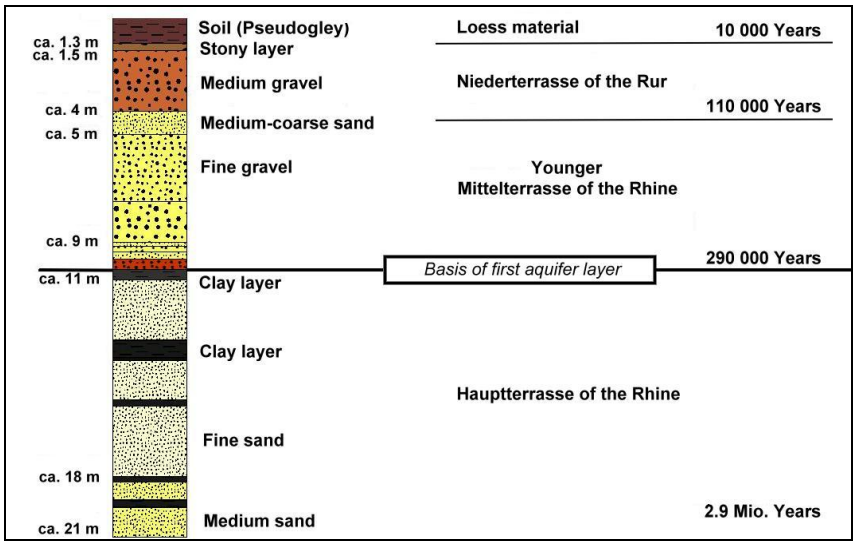

Fig. 5.2: Generalised stratigraphy for the Krauthausen test site /CIO 01/

The first aquifer consists of three different layers /DÖR 97/: the upper layer **U**, the middle layer **M**, and the lower layer **L.** The thicknesses of these layers amount to 3 m, 2 m, and 5 m, respectively. The entire aquifer consists mainly of gravelly and sandy sediments. The groundwater table at the Krauthausen test site varies between 1 m and 3 m below surface. At high groundwater tables (< 1.5 m) the aquifer is semiconfined and at lower groundwater tables the aquifer is semi-unconfined /CIO 01/. The regional groundwater flow is directed towards the northwest with an averaged hydraulic gradient of 0.2 %. The average mean precipitation in the area is 690 mm per year.

To examine the impact of aquifer heterogeneity on solute transport, 74 wells with different measuring equipment were installed at the site, c.f. Fig. 5.3 and **Fig.** 5.4. Among them are 52 wells for the examination of the spatial and temporal concentration distribution during the tracer experiments, 11 wells for the determination of groundwater tables, 28 measuring points for flow meter experiments, 10 infiltration wells, and 1 discharging well to conduct pump tests.

Fig. 5.3: The Krauthausen test site with monitoring wells /KEM 05/

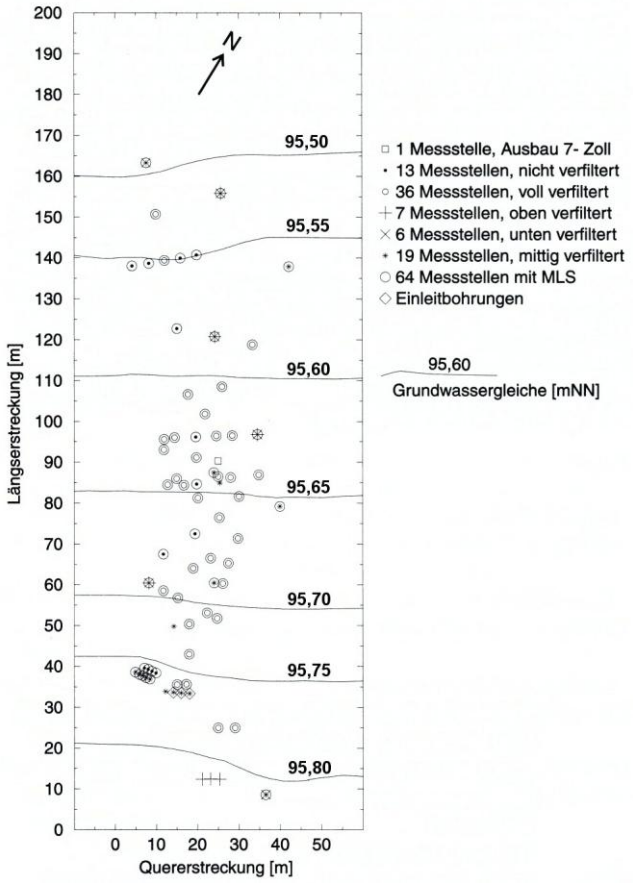

Fig. 5.4: Krauthausen site: groundwater contours and wells /ENG 00/

5.2 Groundwater Flow Field

From May to August 2001 measurements of groundwater flow velocity were performed using flow velocimeters /ENG 03/. During the field campaign groundwater velocity measurements were taken at 361 positions in 21 wells. The measured groundwater velocities were analysed by means of variogram techniques. The experimental variogram was fitted to an exponential model. In a geostatistical estimation of the hydraulic conductivity its spatial heterogeneity is described by the mean, the variance and the correlation lengths. /ENG 03/.

5.2.1 Two-Dimensional Flow Modelling

The rectangular two-dimensional model has a width of 45 m (x-direction) and a length of 150 m (y direction). The means of the permeabilities given in several publications are varying from $3.8 \cdot 10^{-10}$ m² to $7.05 \cdot 10^{-11}$ m²: The averaged Darcy velocity given in /ENG 03/ is 0.33 m d^{-1} = $3.8 \cdot 10^{-6}$ m s^{-1}. The field velocity suggested by bromide transport measurement data /ENG 00/ is decreasing within 110 d to approximately 0.5 m d^{-1} = $5.7 \cdot 10^{-6}$ m s^{-1}, that means a Darcy velocity of $1.5 \cdot 10^{-6}$ m s^{-1}. This can be explained by spatial variability and time dependence of the water table. For the reference case the smallest value was chosen. In a second case a larger value of $1.15 \cdot 10^{-10}$ m^2 is used while all other flow parameters remained unchanged. In Tab. 5.1 the flow parameters are compiled.

Tab. 5.1: Parameters for two-dimensional flow modelling

	reference case	enhanced permeability
permeability mean [m^2]	$7.05 \cdot 10^{-11}$	$1.15 \cdot 10^{-10}$
variance [m^4]	$1.81 \cdot 10^{-20}$	
correlation length [m]	3.43 3.43	
porosity [-]	0.26	
diffusion coefficient [m^2 s^{-1}]	$1.0 \cdot 10^{-9}$	
dispersion length [m] longitudinal transverse	0.75 0.075	

The simulations were performed using Dirichlet boundary conditions for pressure (hydraulic head) which were given in /ENG03/ and are depicted in **Fig.** 5.4. These pressure values gave an average hydraulic gradient of about 0.2 %. In each case the computations were performed on a rectangle grid with about 200 000 nodes.

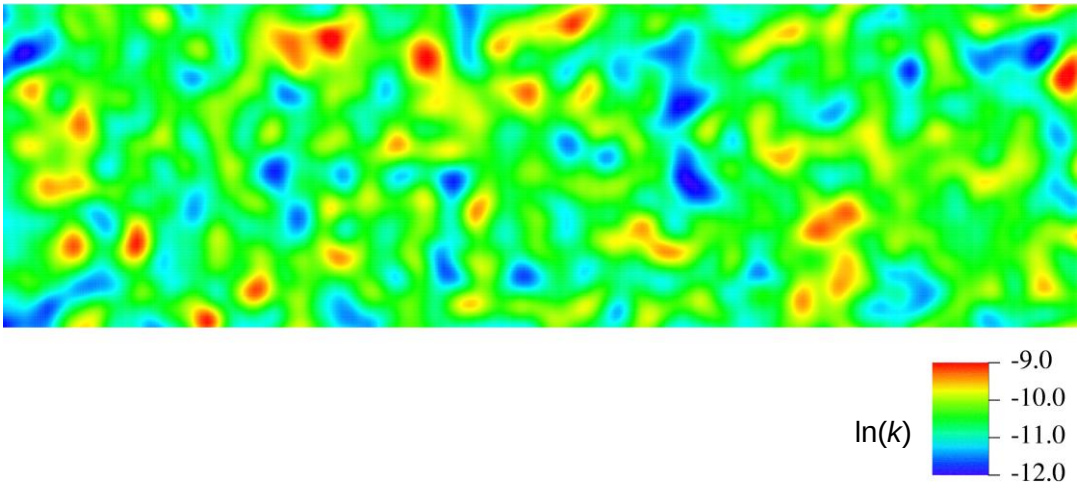

Fig. 5.5: Distribution of the logarithmic permeability (reference case)

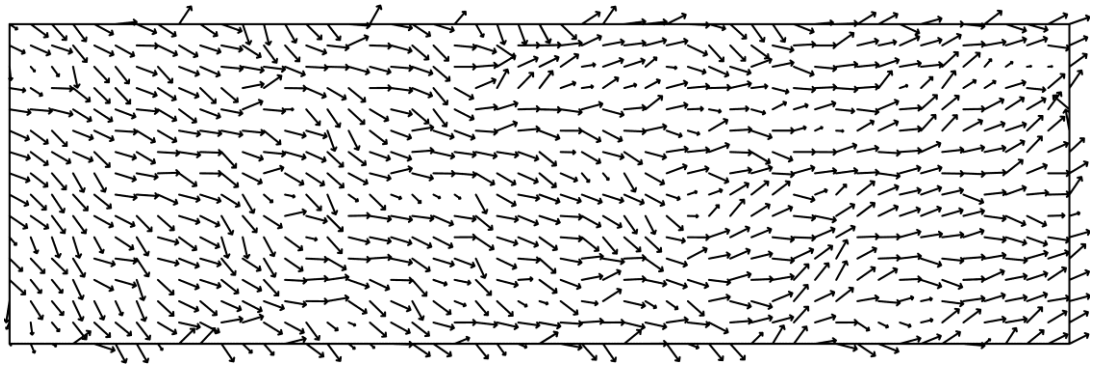

Fig. 5.6: Appropriate Darcy velocity field (reference case)

The permeability distributions were realised by means of the intrinsic random number generator of d^{3}f. In Fig. 5.5 and Fig. 5.7 the permeability fields of reference and enhanced case are shown in logarithmic scale, respectively. One easily can recognise that the mean permeability is higher in the second case. Additionally the appropriate Darcy velocity fields are displayed in Fig. 5.6 and Fig. 5.8.

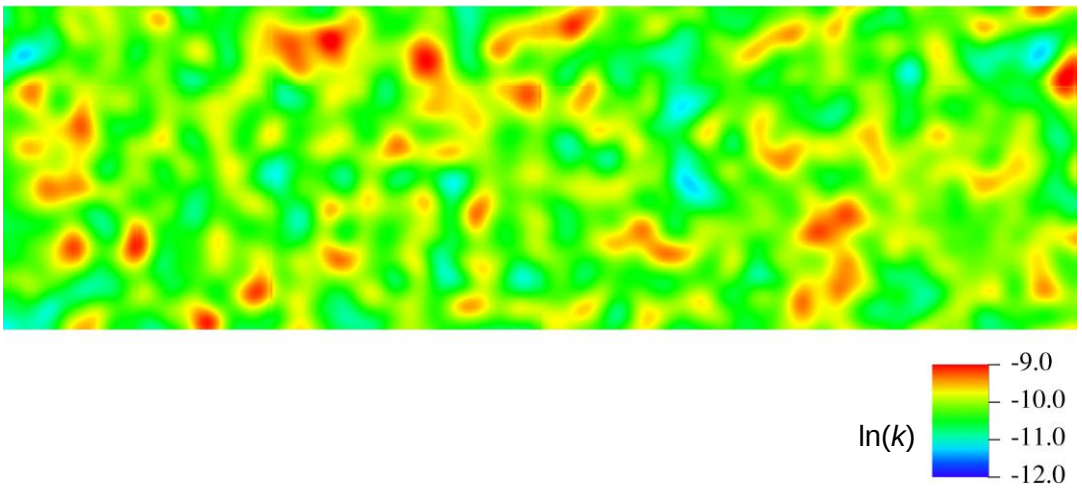

Fig. 5.7: Distribution of the logarithmic permeability (enhanced case)

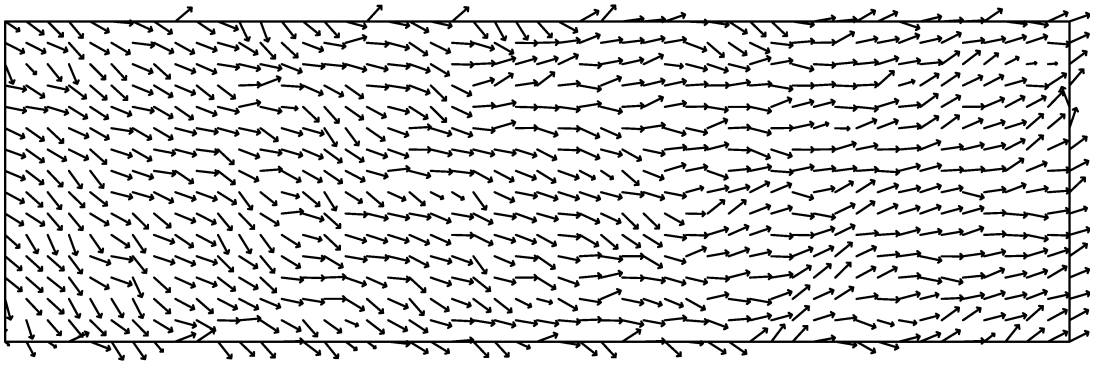

Fig. 5.8: Appropriate Darcy velocity field (enhanced case)

In the reference case the d³f-simulations gave a mean Darcy velocity of $9.2 \cdot 10^{-7}$ m s^{-1} and a theoretical field velocity of $3.54 \cdot 10^{-6}$ m s^{-1}. This does not correspond to the value of field velocity of the bromide centre. Hence a lot of simulations were performed with different permeability values. But beside the reference case only the case with the mean value of $1.15 \cdot 10^{-10}$ m² is presented here. For that case the calculated mean Darcy velocity is $1.91 \cdot 10^{-6}$ m s^{-1}, which roughly corresponds to the velocity of the bromide centre.

5.2.2 Three-Dimensional Flow Modelling

The three-dimensional model has the extensions of 150 m × 45 m × 10 m in length, width, and depth. It consists of three horizontal layers which have (from top to bottom) a thickness of 3 m, 2 m, and 5 m. Due to heterogeneity of the site permeabilities are again modelled stochastically. In all simulations the values of flow parameters of the three layers are the same, except for mean values of permeabilities. Furthermore, the permeabilities are anisotropic. For each of the three layers the correlation lengths in x- and y-direction are 3.43 m, whereas that for z-direction amounts to 0.75 m. In the data for the three-dimensional modelling are compiled. At the lateral borders of the model the boundary conditions for pressure are defined as Dirichlet conditions. The data are given in /ENG 03/. Top and bottom boundary conditions are given as Neumann condition, which means that they are impermeable.

Tab. 5.2: Parameters for three-dimensional flow modelling

layer thickness	upper layer (**U**) 3 m	middle layer (**M**) 2 m	lower layer (**L**) 5 m
permeability mean [m²]	$1.0845 \cdot 10^{-10}$	$2.5463 \cdot 10^{-11}$	$9.4329 \cdot 10^{-11}$
variance [m^4]	$1.565 \cdot 10^{-20}$	$1.263 \cdot 10^{-21}$	$1.025 \cdot 10^{-19}$
correlation length [m]	3.43 3.43 0.75		
porosity [-]	0.26		
diffusion coefficient [$m^2\ s^{-1}$]	$1.0 \cdot 10^{-9}$		
dispersion length [m] longitudinal transverse	0.75 0.075		

In Fig. 5.9 to Fig. 5.12 various drawings of one realisation of the permeability are shown. To give a notion of the three-dimensionality in Fig. 5.9 and Fig. 5.10 a fence- and a block-diagram of the permeability are given in logarithmic scale. On closer inspection one can recognise the three layers. A transversal cross section of the permeability at the centre of the model is shown in Fig. 5.11. Here the borderlines of the various layers are depicted for clearness.

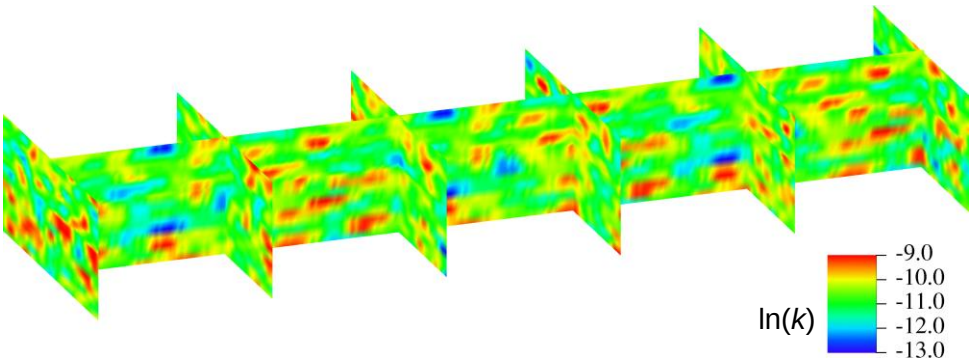

Fig. 5.9: Fence diagram of the permeability distribution in logarithmic scale

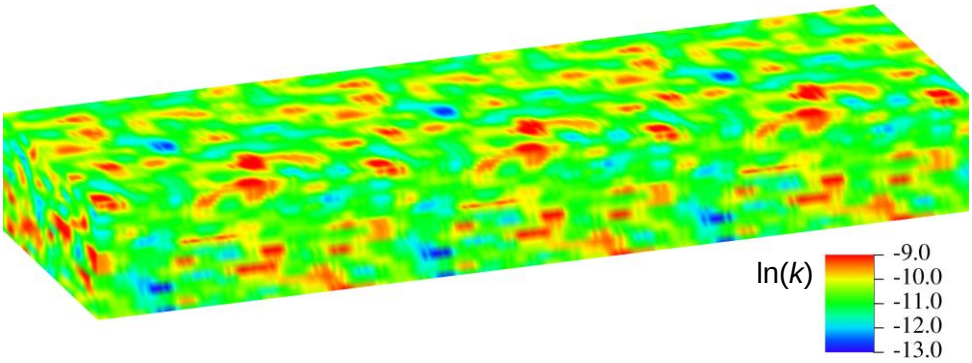

Fig. 5.10: Block diagram of the permeability distribution in logarithmic scale

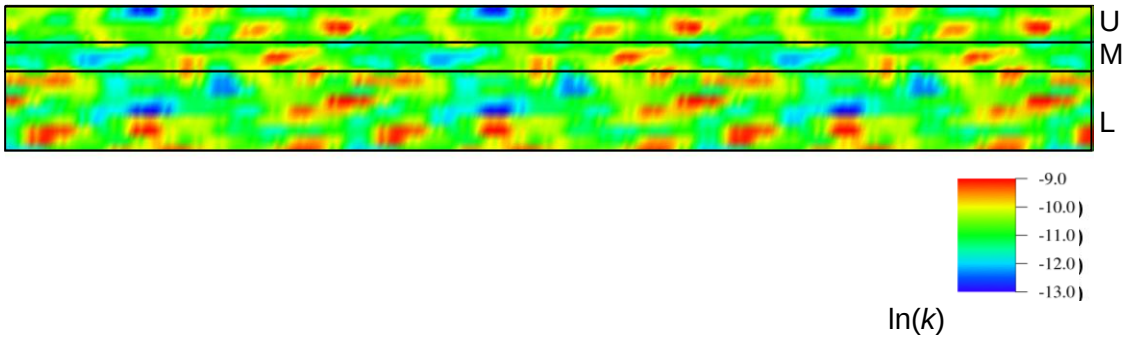

Fig. 5.11: Cross section (centre of model) of permeability in logar

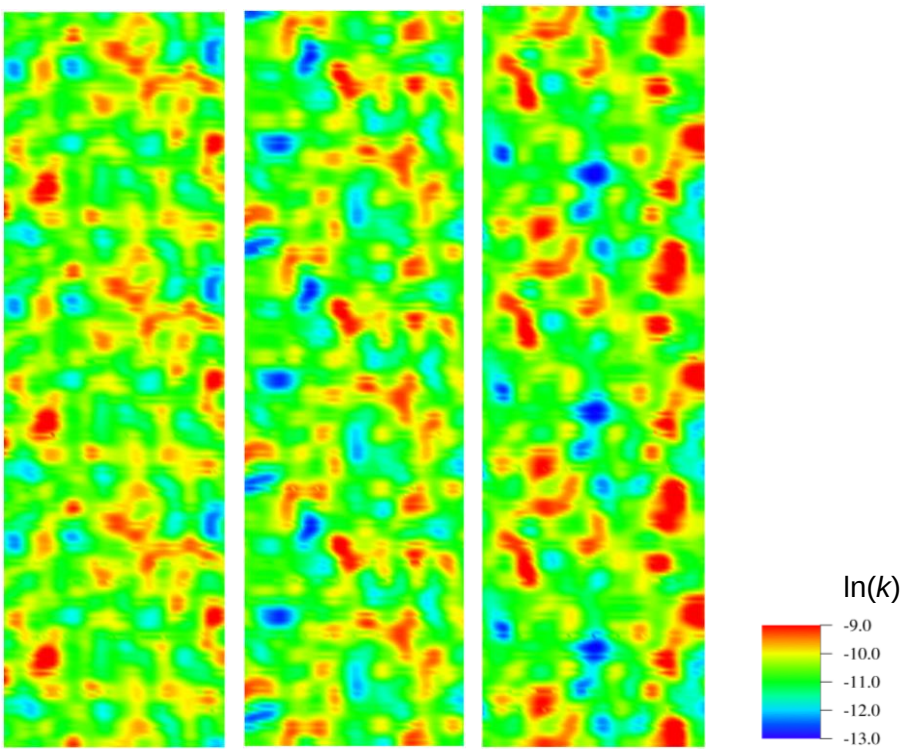

Fig. 5.12: Permeabilities in horizontal planes for U-, M-, and L-layer (logarithmic)

In Fig. 5.12 permeabilities in horizontal planes of the three layers were shown in logarithmic scales. Clearly it can be realised that the permeability in the different layers have different expectation values.

Flow calculations as well as transport calculations were performed on a hexahedron grid with about 440 000 nodes. In Fig. 5.13 and Fig. 5.14 Darcy velocities are plotted in arbitrary but consistent units. In the first plot the velocities in the middle planes of the different layers are given, whereas in the latter the Darcy velocity distribution is shown for a vertical cross section in the middle of the model exaggerated by a factor of 5. In both figures velocity vectors are directed towards (blue) and outwards (red) the drawing plane. The simulated average velocity amounts to $1.7 \cdot 10^{-6}$ m s^{-1}, hence the field velocity is $7.5 \cdot 10^{-6}$ m s^{-1}.

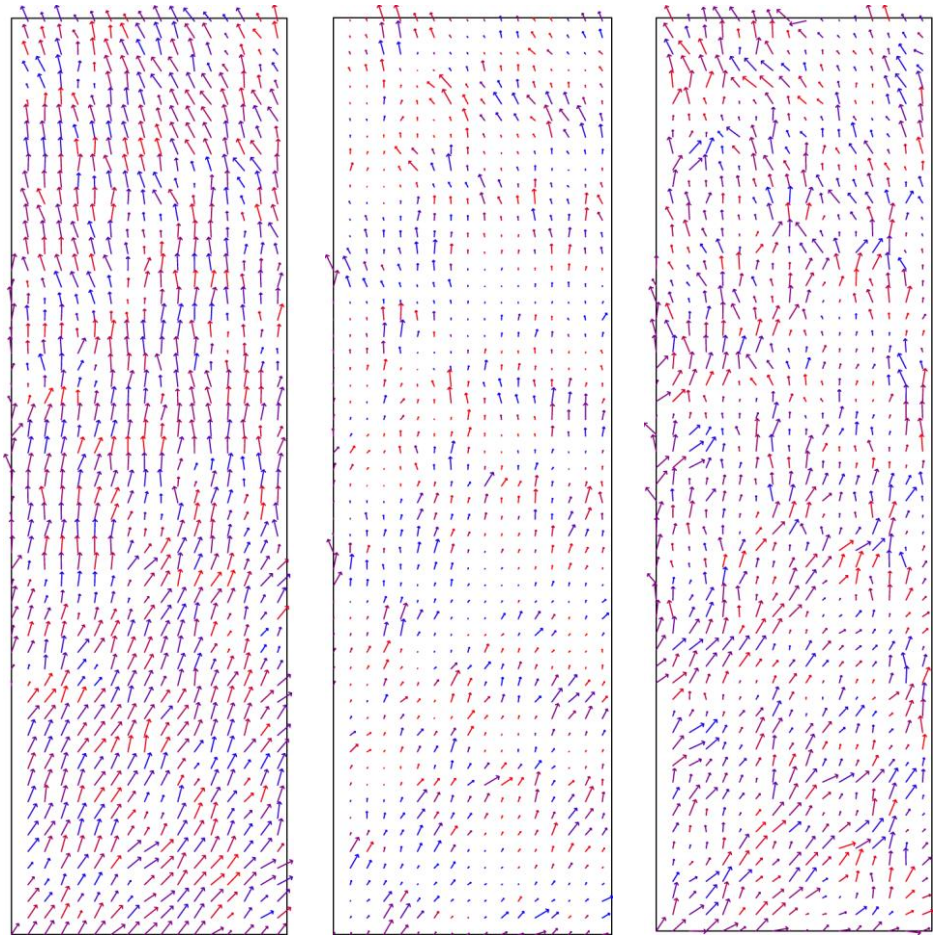

Fig. 5.13: Velocity fields in the middle plane of the three layers U, M, and L
Velocities are directed towards (blue) and outwards (red) the plane

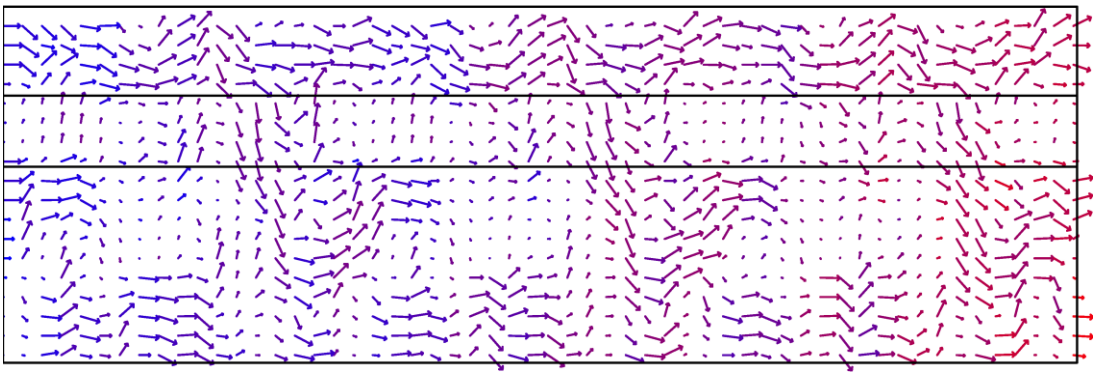

Fig. 5.14: Velocity distribution in a central perpendicular plane
Velocities are directed towards (blue) and outwards (red) the plane;
vertically exaggerated by a factor of 5

5.3 Transport of Uranine, Lithium, and Bromide

In the last years, extensive research concerning the transport of uranine, LiCl, and NaBr was conducted at the test site and documented in the literature /ENG 00/, /DÖR 97/, /DÖR 99/, /NEU 96/, /VER 99/, /VER 00/. On the 30th of August 1994 the sorbing tracers uranine ($C_{20}H_{20}Na_2O_5$) and lithium (LiCl) were injected through three injection wells with depths from 6 to 7 m below surface /DÖR 97/, /ENG 00/. In total 2.67 mol of uranine and 2 659,5 mol of LiCl were dissolved and injected over a period of 5 hours. Using the same injection wells at the same depth on the 3rd of April 1996 a quantity of 1 321.5 mol of the conservative tracer NaBr was injected. In Tab. 5.3 the injection data are compiled.

Tab. 5.3: Locations of sources and tracer masses

source	location			uranine mass [mol] time [s]	lithium mass [mol] time [s]	bromide mass [mol] time [s]
	x [m]	y [m]	z [m] (3D only)			
1	14.09	33.68	6 - 7	0.89 18 000	886.5 18 000	440.5 38 880
2	16.0	33.51	6 - 7	0.89 18 000	886.5 18 000	440.5 38 880
3	18.01	33.34	6 - 7	0.89 18 000	886.5 18 000	440.5 38 880

The tracer plumes were observed for at least 449 days at the numerous measuring points installed in various depths in the test site. The recovery of tracers averaged out at about 50 % or even less. Experimenters guessed that the tracers partially disappear through the thin clay layer which is modelled as impermeable boundary at the bottom, cf. Fig. 5.2.

5.3.1 Two-Dimensional Transport Modelling

The retention of the two sorbing tracers uranine and lithium is modelled using a Freundlich isotherm, cf. (3.16), while bromide is not retarded. The sorption parameters for two-dimensional modelling are assembled in Tab. 5.4. All other parameters needed are already given in Tab. 5.1.

Tab. 5.4: Sorption parameters for two-dimensional transport modelling

	tracer	isotherm	a [m^3 kg^{-1}]	p [-]
sorption	uranine	Freundlich	$4.77 \cdot 10^{-5}$	0.81
	lithium	Freundlich	$1.02 \cdot 10^{-4}$	0.61
	bromide	Henry	0.0	1.0
	rock density [kg m^{-3}]		2600	

In the case of two-dimensional transport the front face was modelled using a Dirichlet inflow boundary condition, while at the opposite side Dirichlet outflow boundary „out“, was considered. The other boundaries were modelled as impermeable with Neumann conditions.

The coordination system used by the experimenters is defined by the medium injection well as the origin of the coordinates. Hence our coordinates run from -16 m to 29 in x-direction, and from -33.51 m to 116.49 m in y-direction. Note that in the cases of measurements that the experimental results plotted here give only the vertically averaged concentrations.

In Fig. 5.15 to Fig. 5.17 the simulated concentration plumes of uranine, lithium, and bromide after 85 d, 154 d, 365 d, and 449 d are pictured for the reference case. It can be recognised that the tracers first move to the right and later to the left hand side of the modelled area. One can clearly see that uranine underwent the strongest retardation contrary to bromide which was not adsorbed and spread over the longest distance. This behaviour is in agreement with the measurements. One should keep in mind that the tracers have different concentration scales.

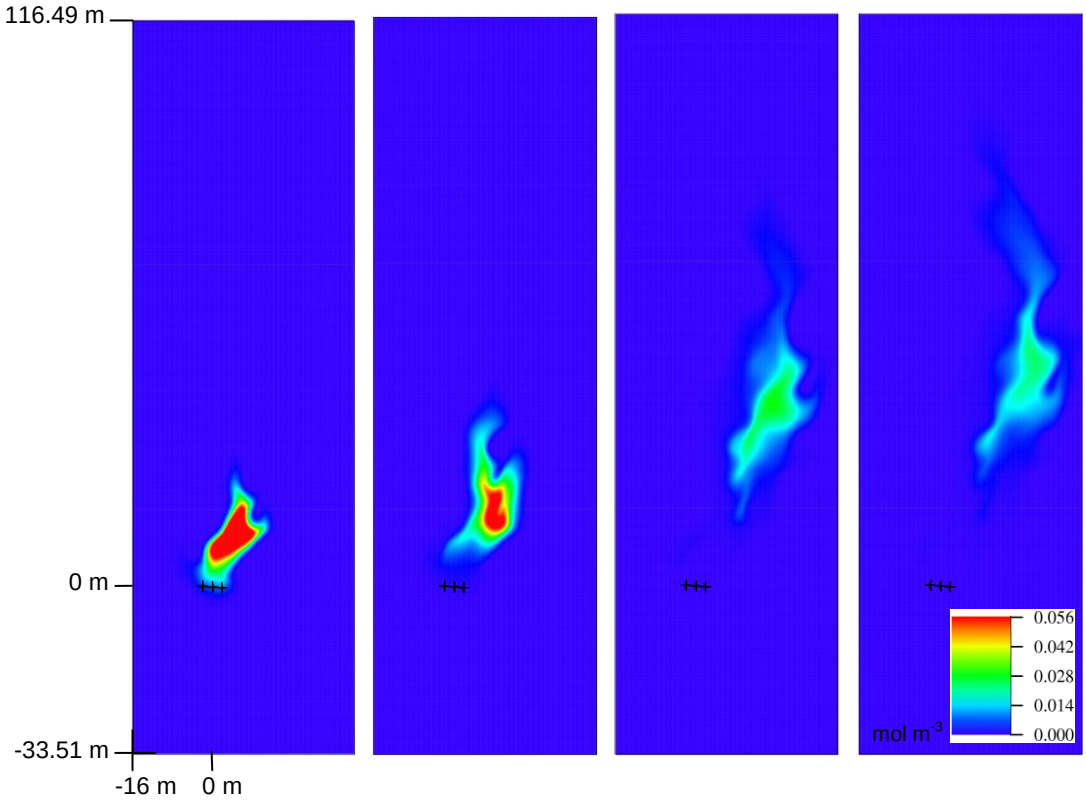

Fig. 5.15: Uranine plume after 85 d, 154 d, 365 d, and 449 d (ref. case)

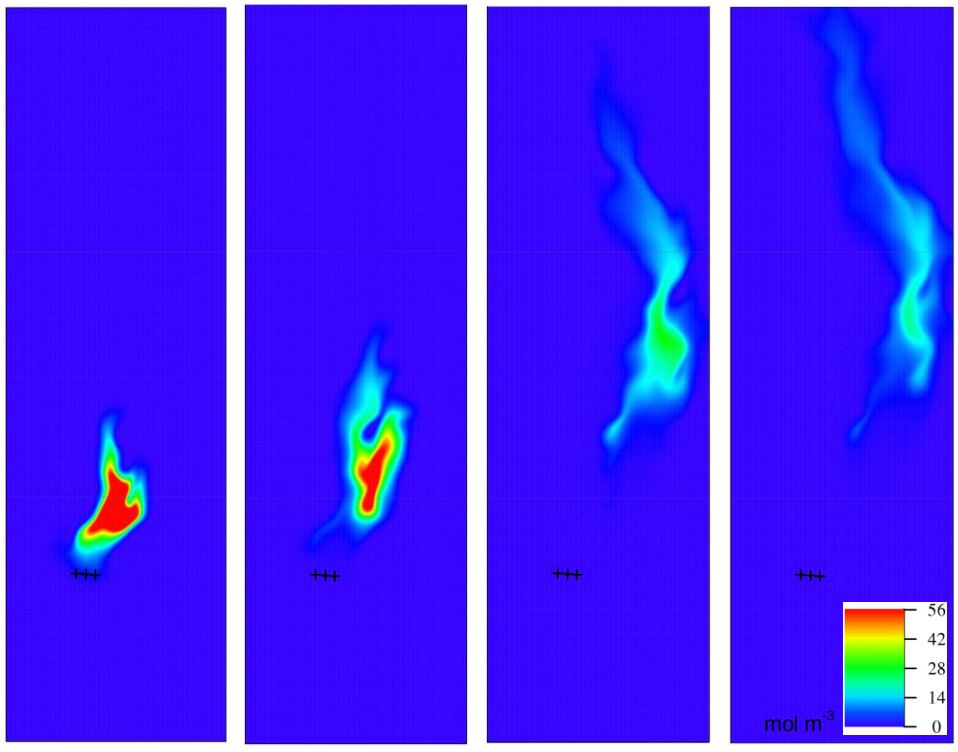

Fig. 5.16: Lithium plume after 85 d, 154 d, 365 d, and 449 d (ref. case)

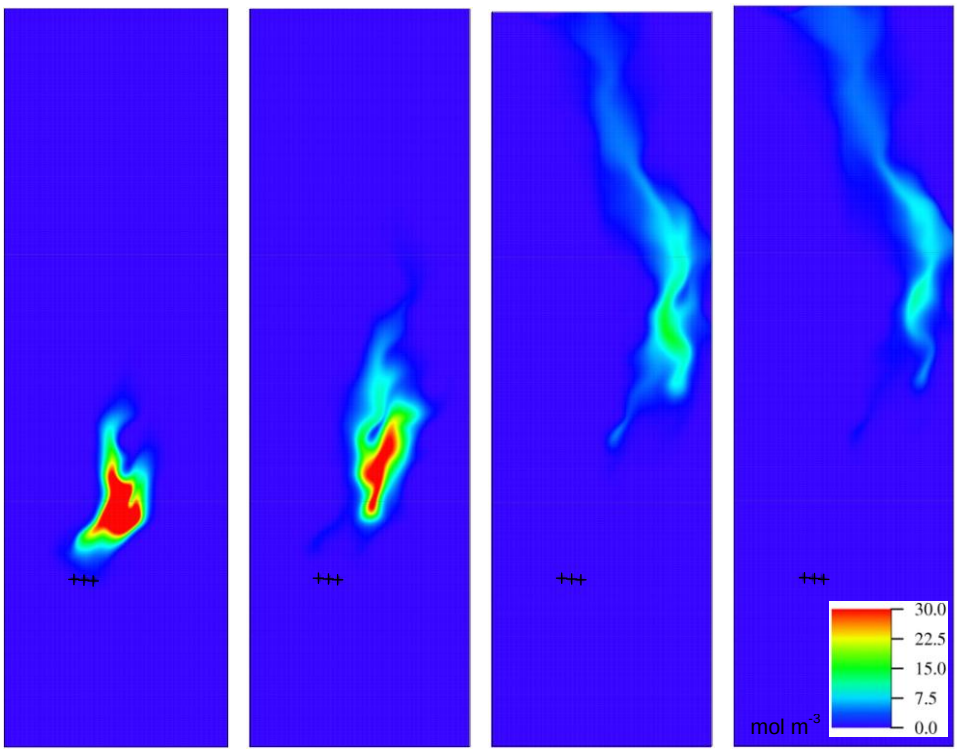

Fig. 5.17: Bromide plume after 85 d, 154 d, 365 d, and 449 d (ref. case)

In Fig. 5.18 to Fig. 5.20 the simulated concentration plumes of uranine, lithium, and bromide after 85 d, 154 d, 365 d, and 449 d are pictured for the case with enhanced permeability. Here the movement of the tracer plumes to the right firstly and then the migration to the left is more pronounced than in the reference case. Again the uranine undergoes the strongest retardation, while the bromide is not adsorbed and covers the longest distance. One should keep in mind that the tracers have different concentration scales and the scales change within the figures.

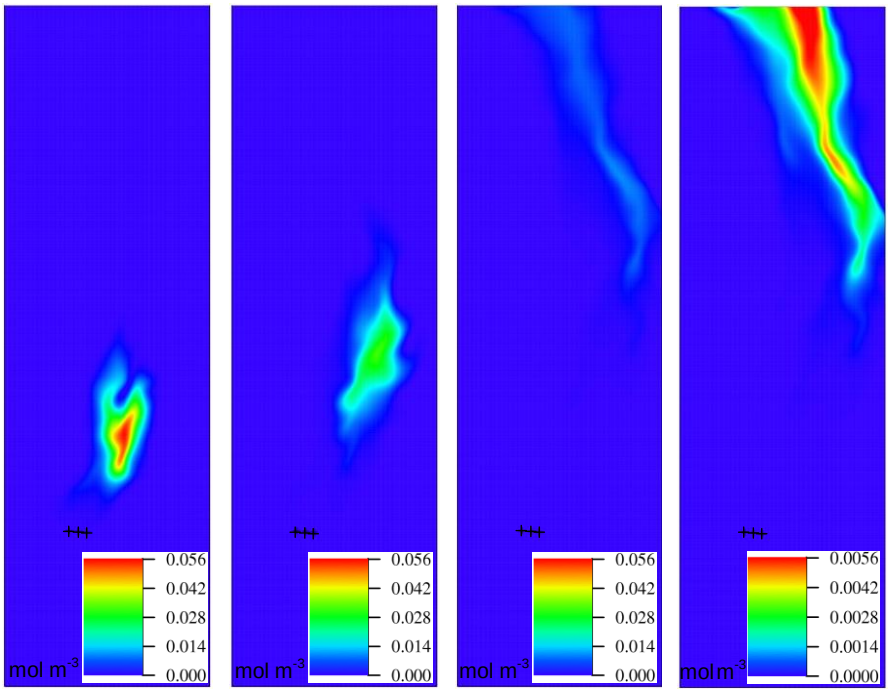

Fig. 5.18: Uranine plume after 85 d, 154 d, 365 d, and 449 d (enhanced perm.)

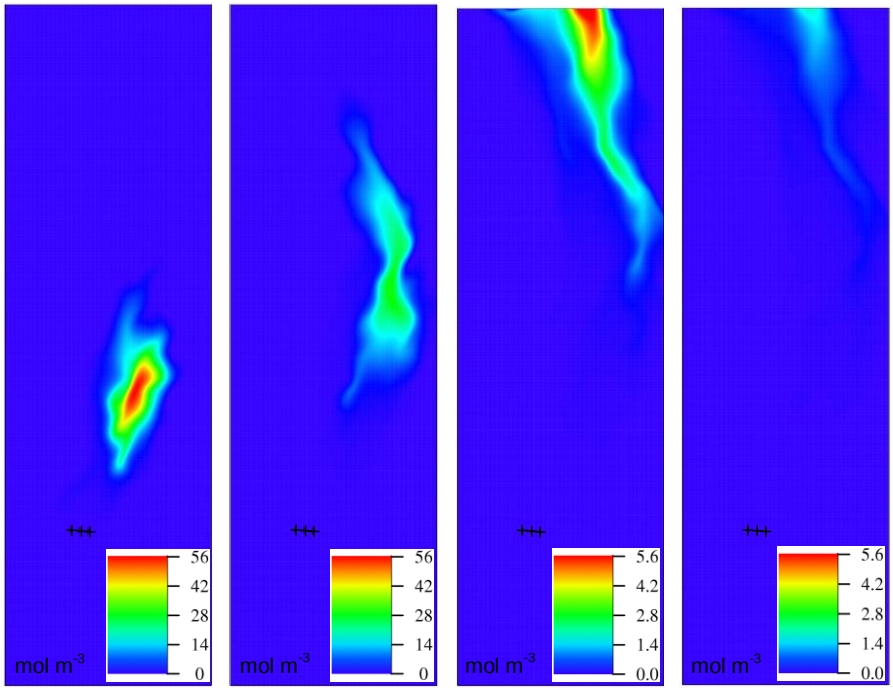

Fig. 5.19: Lithium plume after 85 d, 154 d, 365 d, and 449 d (enhanced perm.)

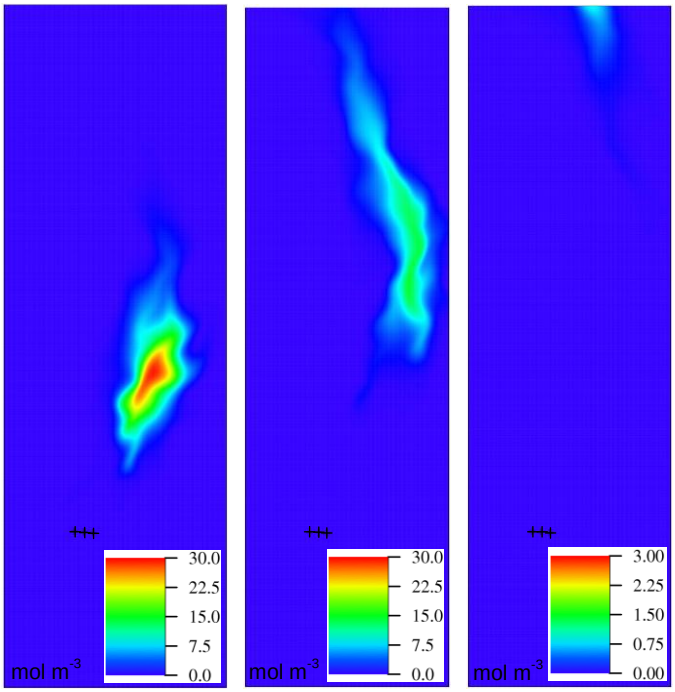

Fig. 5.20: Bromide plume after 85 d, 154 d, and 365 d (enhanced perm.)

In Fig. 5.21 the simulated concentration distribution of uranine, lithium, and bromide after 85 d for the enhanced permeability case is depicted. Fig. 5.22 shows the data for the three tracers measured at the same time. These figures give vertically averaged concentrations. In both figures the concentrations are normalised to the highest vertically averaged concentration. That means the outer lines in both figures are defined by the 5%-lines.

Comparing simulated and measured concentrations show that the calculations with d^3f and r^3t deliver feasible results. Uranine undergoes the strongest retardation whereas lithium and bromide are almost equally retarded.

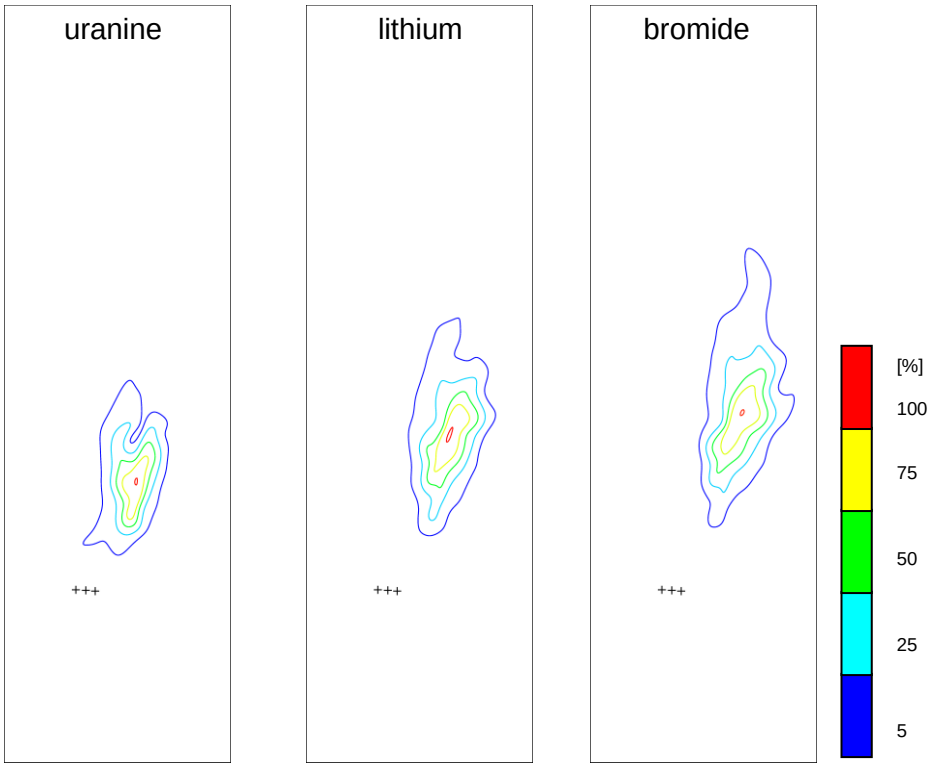

Fig. 5.21: Higher permeability: uranine, lithium, bromide plumes after 85 d scaled to maximum values of concentration

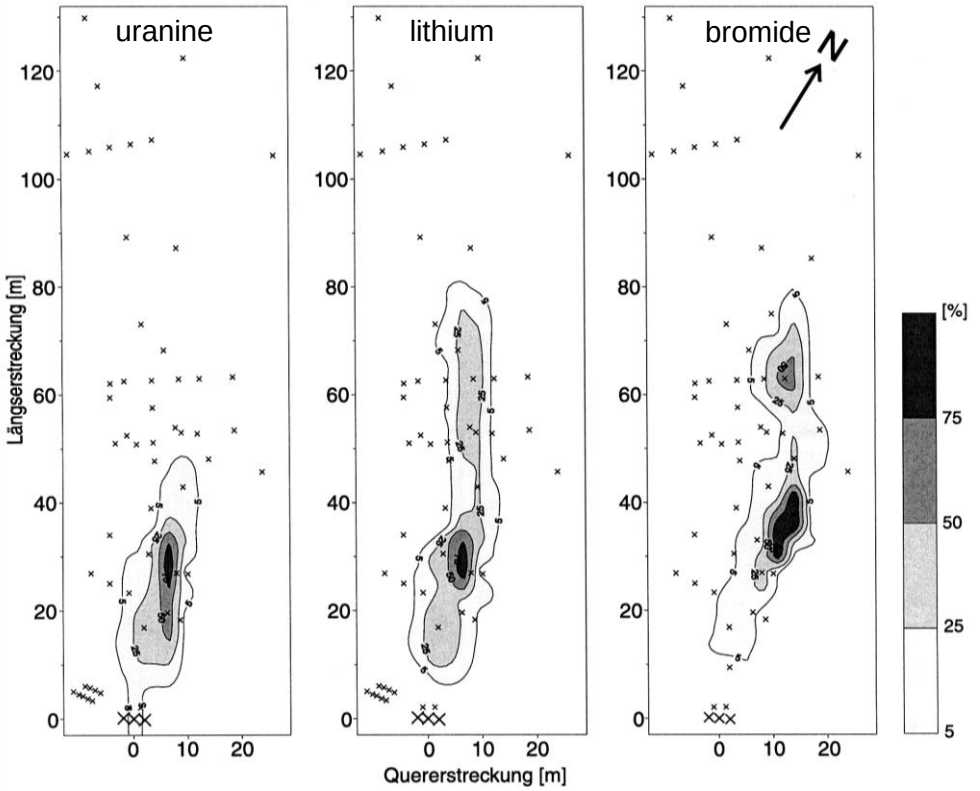

Fig. 5.22: Uranine, lithium, and bromide plumes after 85 days /ENG 00/ scaled to maximum of vertically averaged concentration

5.3.2 Three-Dimensional Transport Modelling

The three-dimensional transport modellings were performed with the identical tracer injection (cf. Tab. 5.3) as in the two-dimensional case, except that the inflow takes place at a depth of 6 – 7 m. Tab. 5.5 shows the sorption parameters for the three layers. For uranine and lithium Freundlich isotherms are assumed whereas bromide is not adsorbed. The data are taken from /DÖR 97/.

Tab. 5.5: Sorption parameters for three-dimensional transport modelling

	layer	tracer	isotherm	a [m^3 kg^{-1}]	p [-]
sorption	U	uranine	Freundlich	$3.93 \cdot 10^{-5}$	0.83
		lithium	Freundlich	$1.05 \cdot 10^{-4}$	0.53
		bromide	Henry	0.0	--
	M	uranine	Freundlich	$3.63 \cdot 10^{-5}$	0.85
		lithium	Freundlich	$9.23 \cdot 10^{-5}$	0.49
		bromide	Henry	0.0	--
	L	uranine	Freundlich	$4.77 \cdot 10^{-5}$	0.81
		lithium	Freundlich	$1.02 \cdot 10^{-4}$	0.61
		bromide	Henry	0.0	--
	rock density [kg m^{-3}]		2600		

The boundary conditions for the three-dimensional case are exactly the same as for two-dimensional case. The front face was modelled using a Dirichlet inflow boundary condition, while at the opposite side the standard outflow boundary condition was used. The other boundaries were modelled as impermeable with Neumann conditions.

Again the coordinate system used by the experimenters is defined by the medium injection well as the origin of the coordinates. Hence the coordinates run from -16 m to 29 in x-direction, and from -33.51 m to 116.49 m in y-direction. Note that in the cases of measurements the experimental results plotted here give only the vertically averaged concentrations.

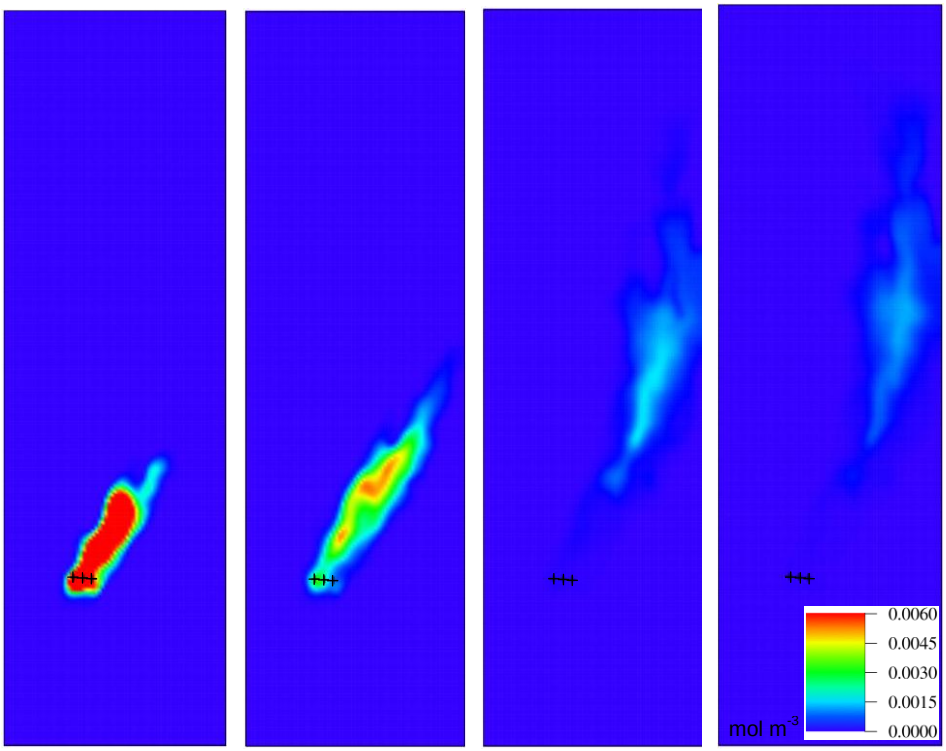

Fig. 5.23: Horizontal uranine plume after 85 d, 165 d, 365 d, and 449 d

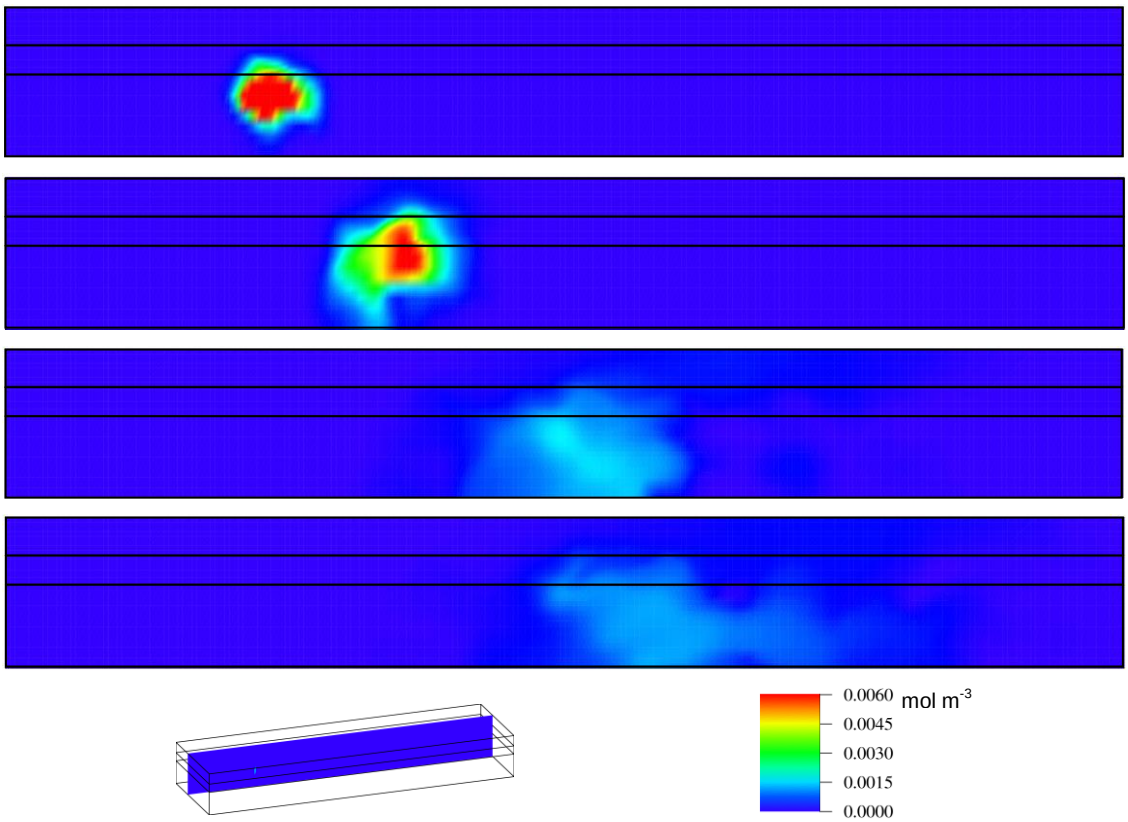

Fig. 5.24: Vertical uranine plume after 85 d, 165 d, 365 d, and 449 d

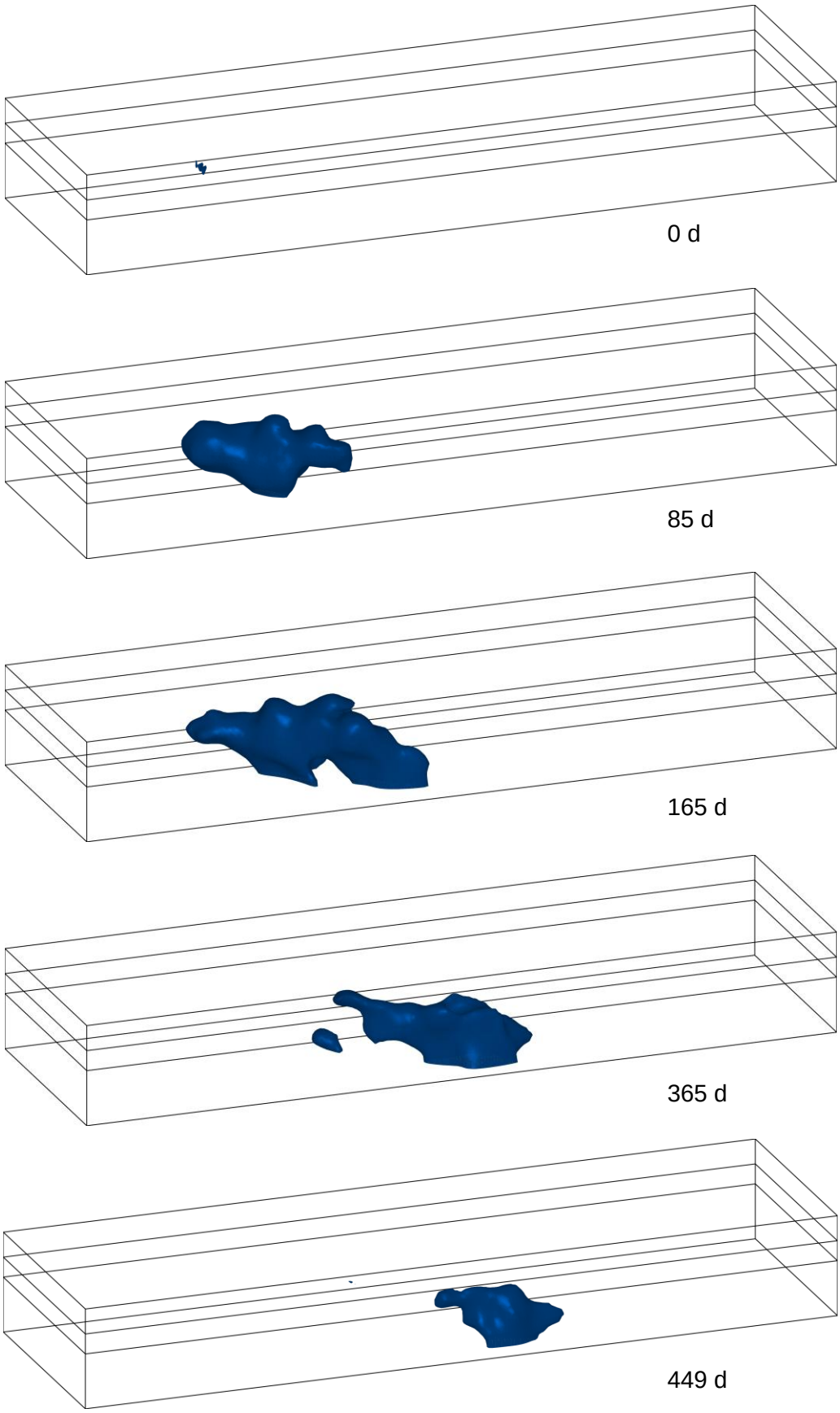

Fig. 5.25: Uranine 1‰-plume after 0 d, 85 d, 165 d, 365 d, and 449 d

In Fig. 5.23 the concentration distribution of uranine in a horizontal plane at a depth of 6.5 m after 85 d, 165 d, 365 d, and 449 d is depicted. Fig. 5.24 pictures the uranine plume in a vertical plane for the same time points. The position of this vertical plane is shown in Fig. 5.24, too. Finally, in Fig. 5.25 the 1‰-isosurface of uranine at the same times is shown. This plot clearly identifies the three-dimensionality of the model. The plot for the injection start at about 0 d is included to show the locations of the injection wells. In Fig. 5.26 - Fig. 5.28 the results of the simulations for lithium and in Fig. 5.29 - Fig. 5.31 the results for bromide are shown. In these cases the 50%-isosurfaces are represented. Each tracer is displayed by colour-bars with the same scales.

In the three-dimensional cases it is even clearer to recognise that the migration of the tracers in the horizontal plane proceeds first to the right boundary and afterwards to the left. This is a consequence of the flow field. In Fig. 5.13 the directions of the velocity in layer **L**, which comprises the horizontal plane at a depth of 6.5 m, shows an identical pattern. At the vertical planes one can see the immediate diving down of the tracers towards the bottom of the model. This vertical movement is described in /DÖR 97/, too. The experimental recovery of the tracers is rather low, it is about 50% or even less. The diving down which is observed in reality and in our calculations can be an indication of the disappearance of tracer mass through the bottom of the examined test field. The bottom is made up of a thin clay layer with a thickness of some decimetres and it cannot be excluded that it contains hydraulic windows. It may be worthwhile to investigate the density influence on the migration of the tracers.

In Fig. 5.32 the simulated concentration of uranine, lithium, and bromide in the horizontal plane at a depth of 6.5 m 85 d after the injection is shown. Fig. 5.33 depicts the experimental findings about the uranine, lithium, and bromide plumes after 85 d. The latter figure gives vertically averaged concentrations. In both figures the concentrations are normalised to the highest concentration. Again the simulations show feasible results.

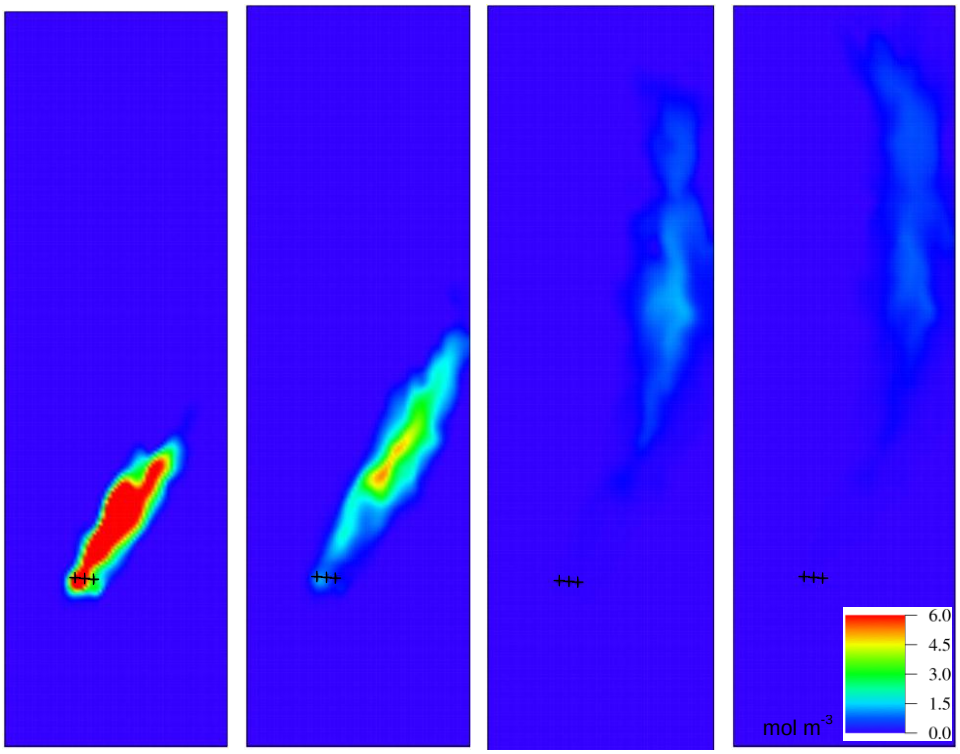

Fig. 5.26: Horizontal lithium plume after 85 d, 165 d, 365 d, and 449 d

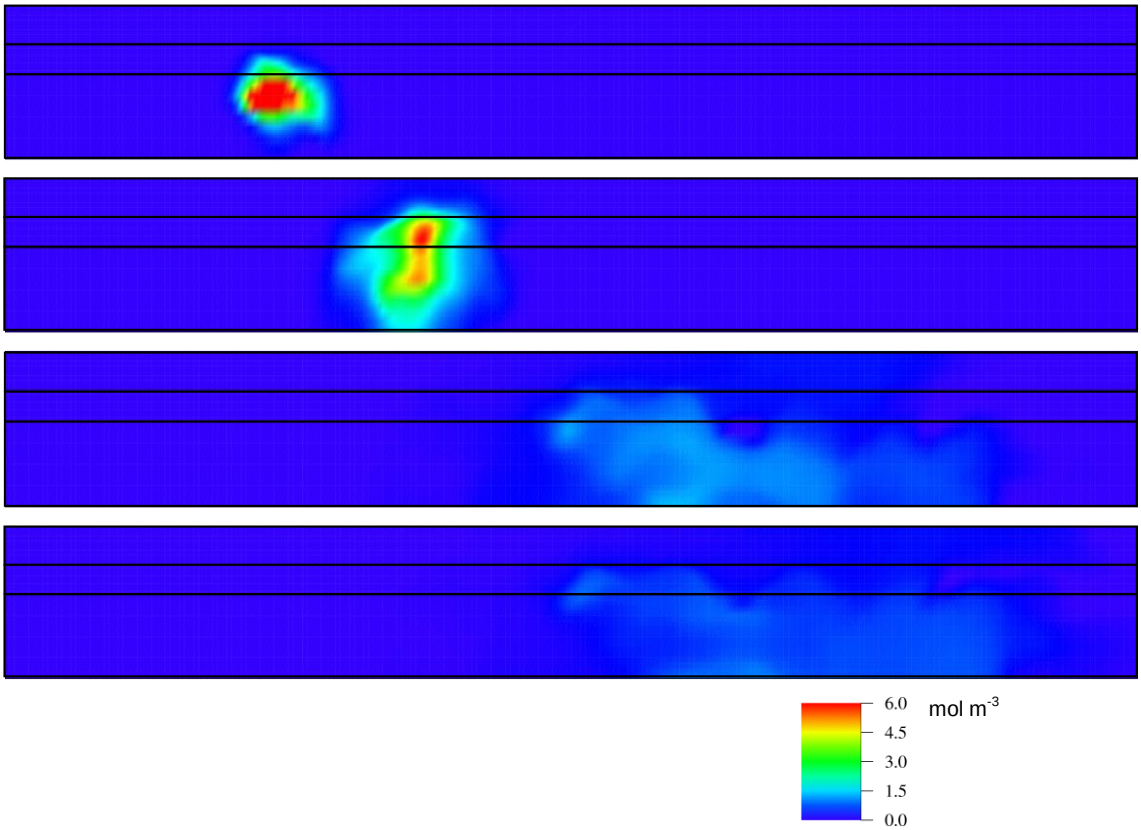

Fig. 5.27: Vertical lithium plume after 85 d, 165 d, 365 d, and 449 d

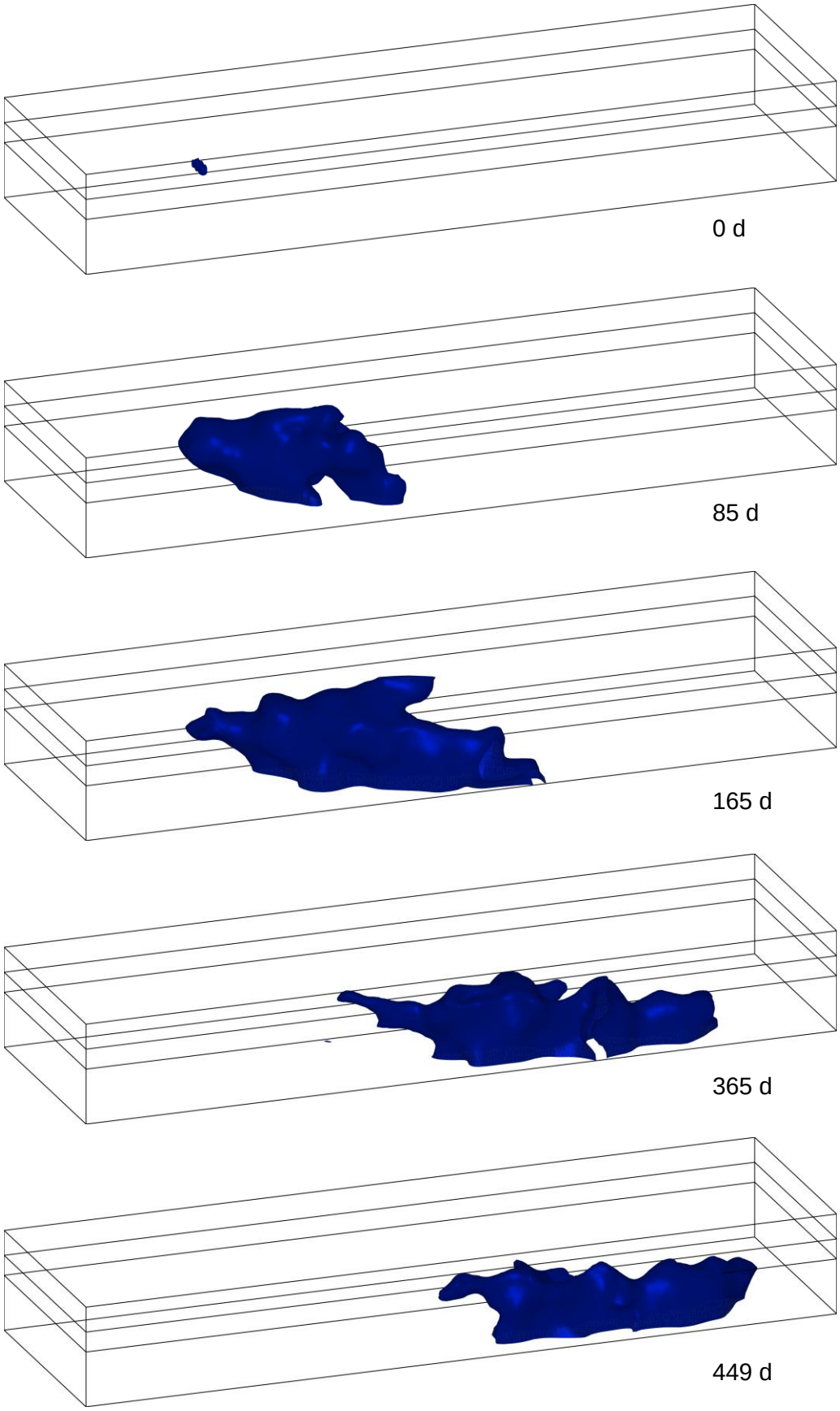

Fig. 5.28: Lithium 50%-plume after 0 d, 85 d, 165 d, 365 d, and 449 d

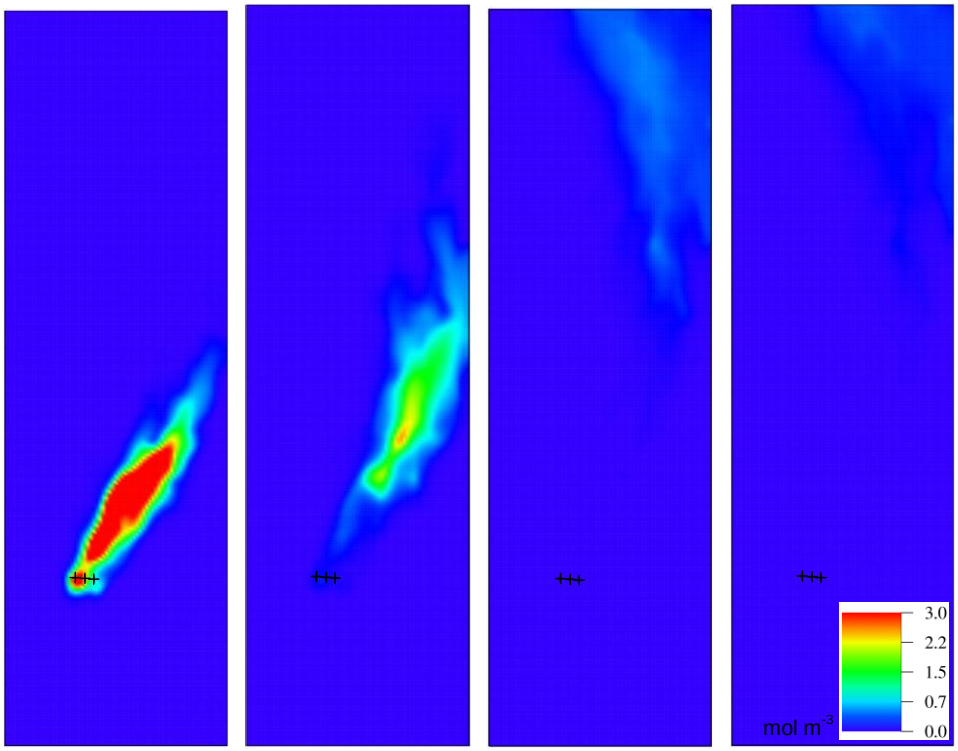

Fig. 5.29: Horizontal bromide plume after 85 d, 165 d, 365 d, and 449 d

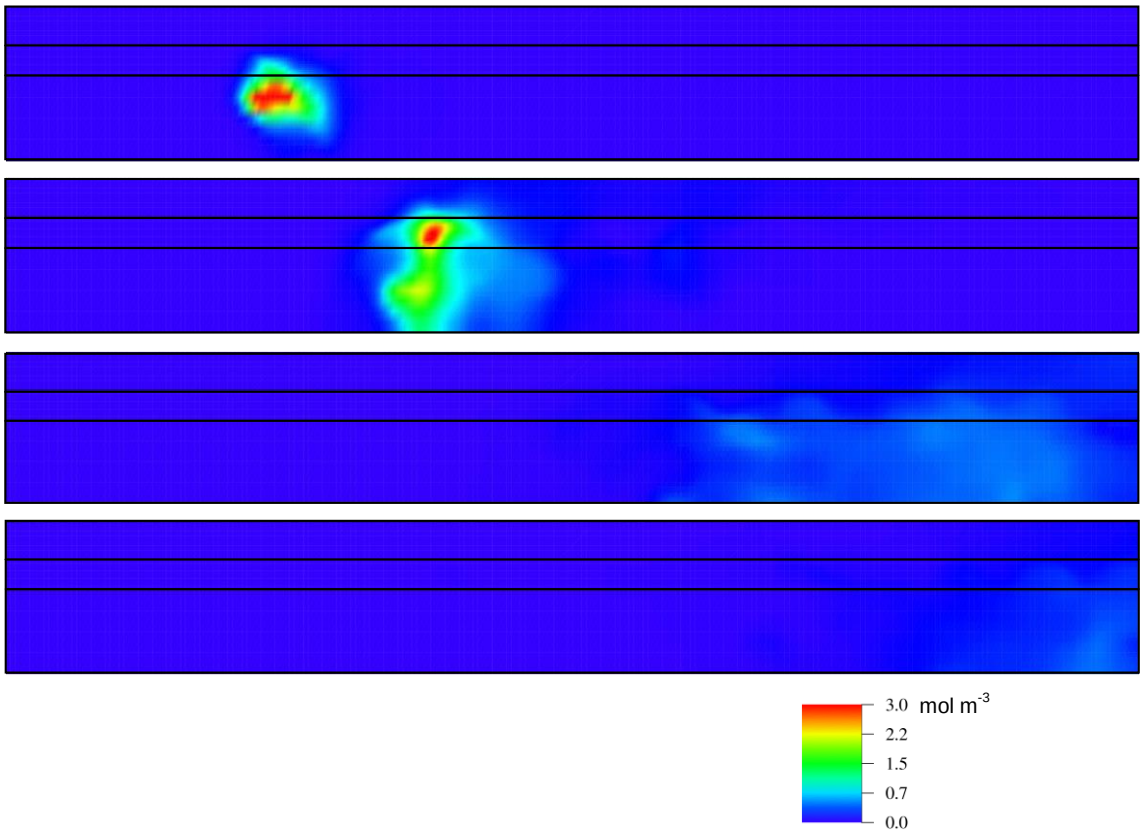

Fig. 5.30: Vertical bromide plume after 85 d, 165 d, 365 d, and 449 d

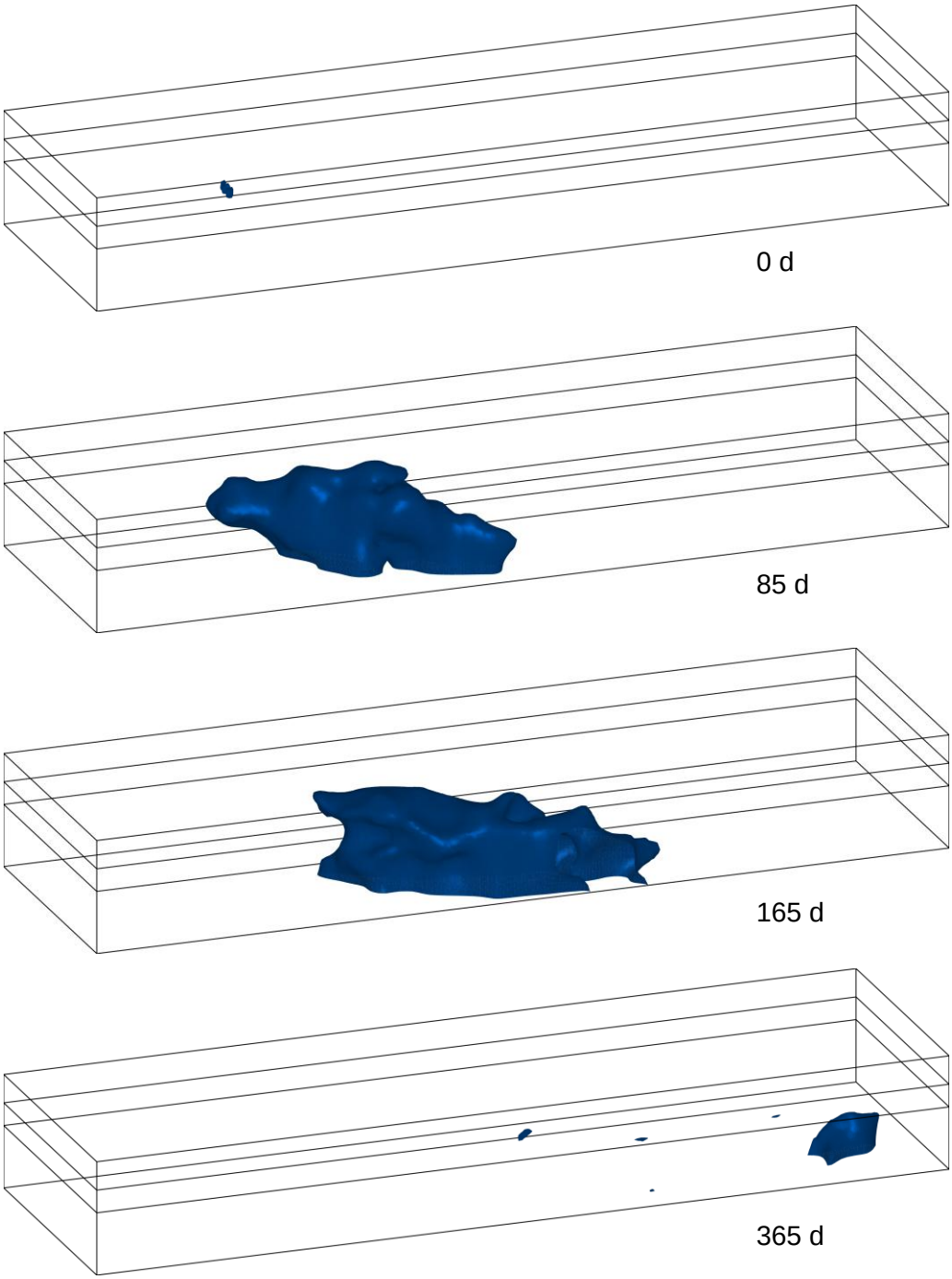

Fig. 5.31: Bromide 50%-plume after 0 d, 85 d, 165 d, 365 d, and 449 d

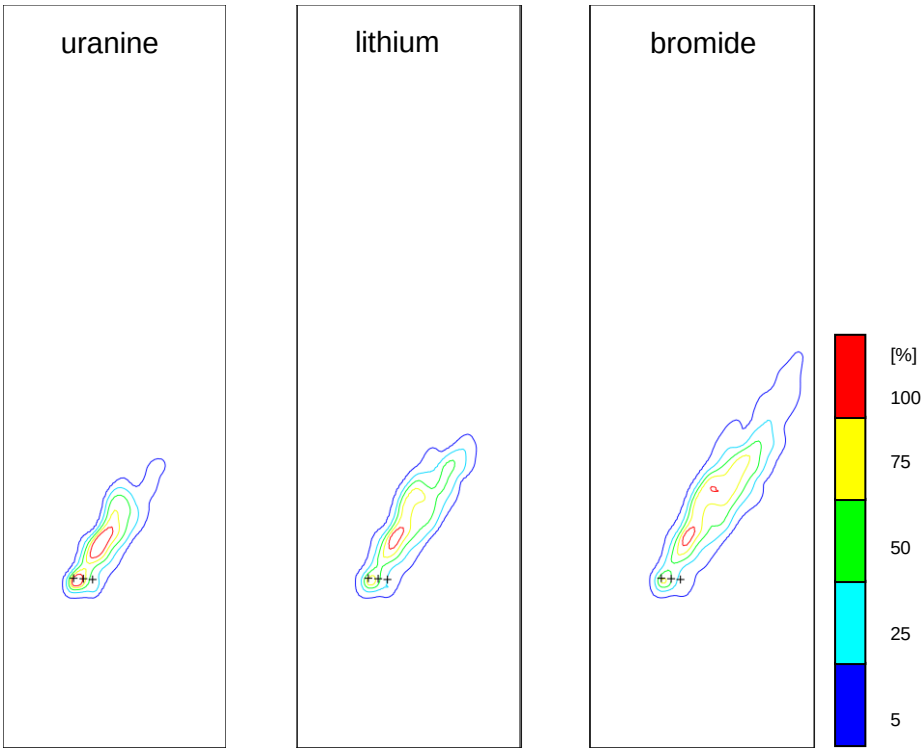

Fig. 5.32: Uranine, lithium, and bromide plumes after 85 days

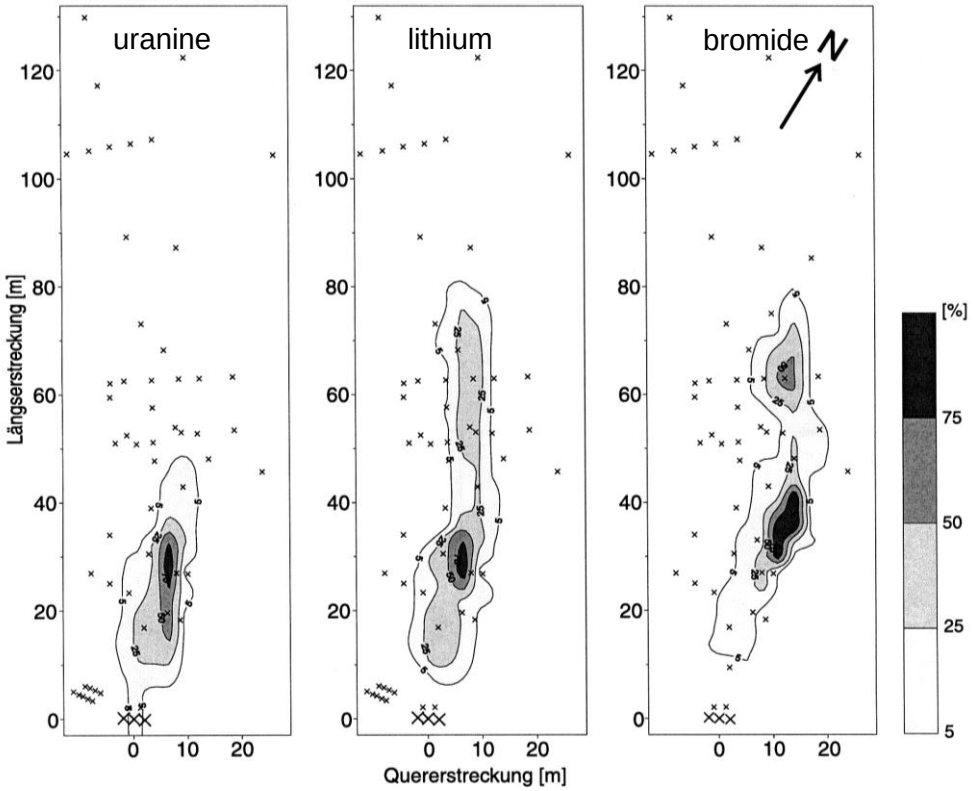

Fig. 5.33: Uranine, lithium, and bromide plumes after 85 days /ENG 00/

5.4 Conclusions

In this test case stochastic flow modelling and subsequent transport modelling using non-linear adsorption isotherms were performed. Both flow and transport calculations were carried out two- and three-dimensionally. In both cases the results are consistent in comparison with measurements. Principally stochastic modellings have to be repeated sufficiently often with different realisations of the permeability fields. Then reliable results are given in appropriate averages of the various findings. Due to the requirements in CPU-time only a single realisation of the permeability fields was examined.

6 Zinc Transport at the Cape Cod Site, Massachusetts, USA

At the Cape Cod site some pollutants were found even at a distance of 5 500 m to the source and in a depth of about 30 m. In contrast to that zinc has migrated less than 100 m. This limited propagation is caused by pH-dependent sorption processes. Hence the simultaneous transport of zinc and protons was modelled whereas the proton concentration affected the adsorption of zinc.

6.1 Site Description

The field site considered here is located in the West of Cape Cod, Massachusetts. About 59 years of land disposal of sewage effluent resulted in contamination of the aquifer amongst others with zinc (Zn). The sewage plant was opened in 1936 and shut down in 1995. Extensive measurement campaigns and field-tests were undertaken during the last years of operation and for the first years after closure.

6.2 Groundwater Flow

The aquifer consists of medium to coarse sands and gravels with a median grain size of ~ 0.5 mm. It contains less than one percent silt and clay /KEN 00/. The water table is located 4 m to 7 m below land surface and slopes to the south at ~ 1.6 m per 1000 m. Groundwater flow direction is thus generally from north to south but locally it is from the sewage treatment facility towards the Ashumet Pond (cf. Fig. 6.1). The flow is nearly horizontal except for the recharge that results in a vertical flow component close to the water table. The water table altitude fluctuates about 0.80 m and the flow direction varies about 16° (c.f. Fig. 6.2) /KEN 00/.

6.3 Zinc Contamination

The distribution of dissolved zinc along a longitudinal cross section as of 1997 is shown in Fig. 6.3. Dots indicate the locations of sampling points. Distance downstream refers to the centre of the southernmost set of four disposal beds as indicated in Fig. 6.2. The zinc contamination at the southern corner of this set - about 62 m downstream, marked as point S469 in Fig. 6.2 - extended 13 to 15 m deep into the aquifer (see Fig. 6.3). Zinc concentrations observed throughout the vertical profile were in the range between

0.4 – 1.5 µM (µmol/l) while measurements of the sewage effluent and the groundwater under the disposal beds showed a range from 0.4 to 2 µM.

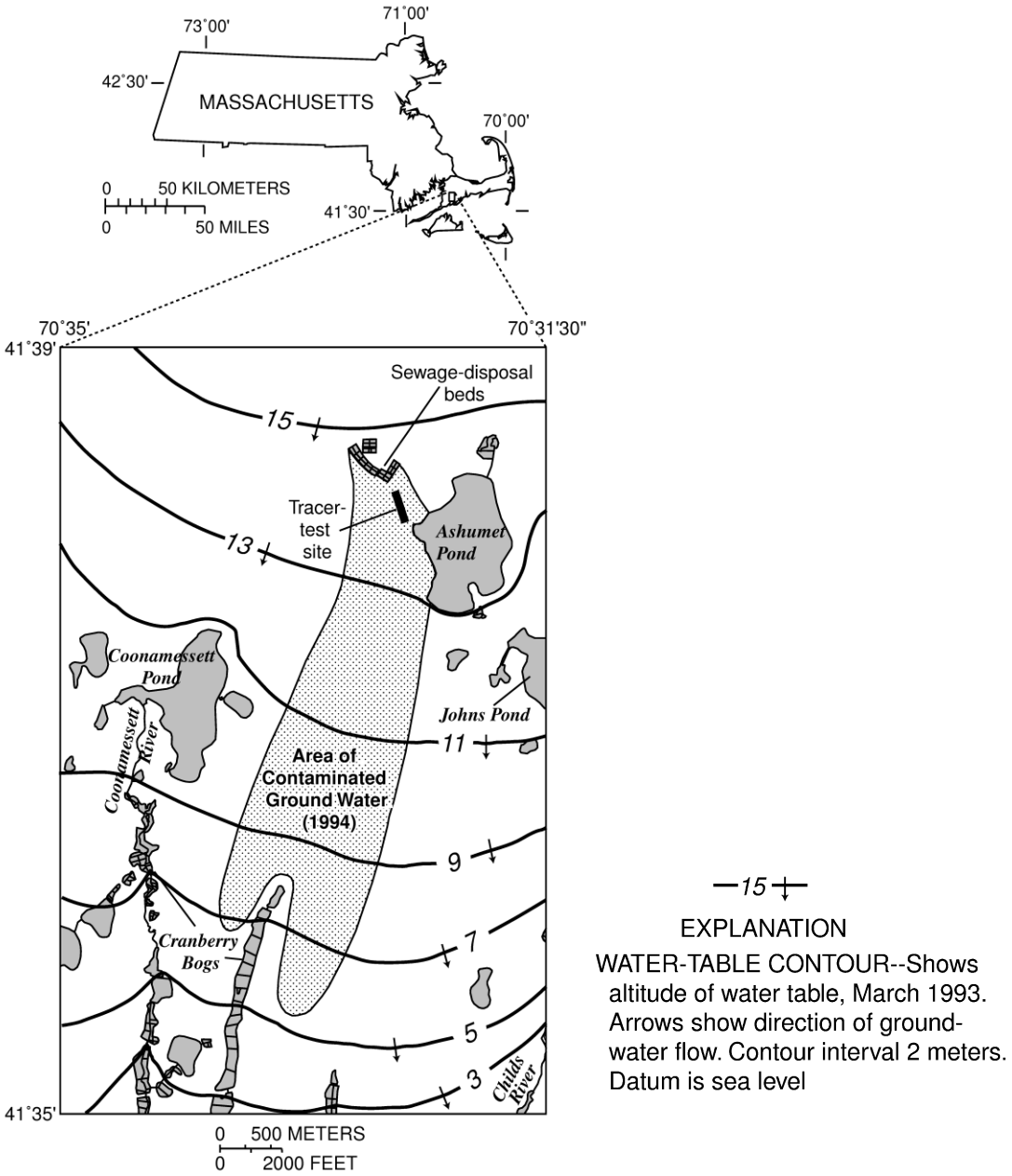

Fig. 6.1: Location of the area of sewage-contaminated groundwater water table contours and area of contamination; from /HES 99/

At 90 m downstream a sharp transition in the thickness of the zinc plume was observed. Further downstream the plume covered only the topmost 2-4 m of the contaminated region. The leading edge of the Zn-plume was sharp and was located approximately 400 m downstream. In contrast, conservative, non-reactive constituents of the sewage plume formed a diffuse leading edge greater than 5500 m downstream of the source.

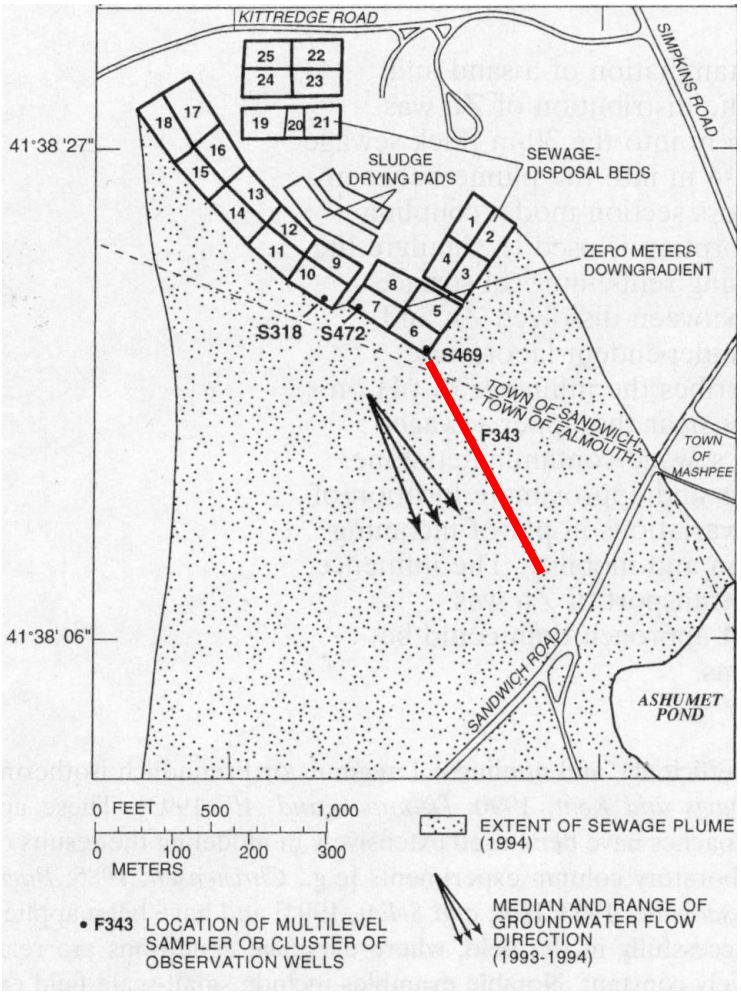

Fig. 6.2: Location of the area of sewage-contaminated groundwater facility layout and hydraulic gradient direction; from /KEN 00/ The modelled region (two-dimensional) is marked in red.

Anomalously high concentrations of dissolved Zn were found about 280 m down-stream. As shown in Fig. 6.3, they amounted to values of more than 8 µM. The reason for this concentration anomaly is not quite clear since there are no records about the operation history of the sewage facility. A possible explanation involving a short-term decrease of the pH-value is presented in /KEN 00/. The referring mechanism will be explained in more detail in chapter 6.6.2.

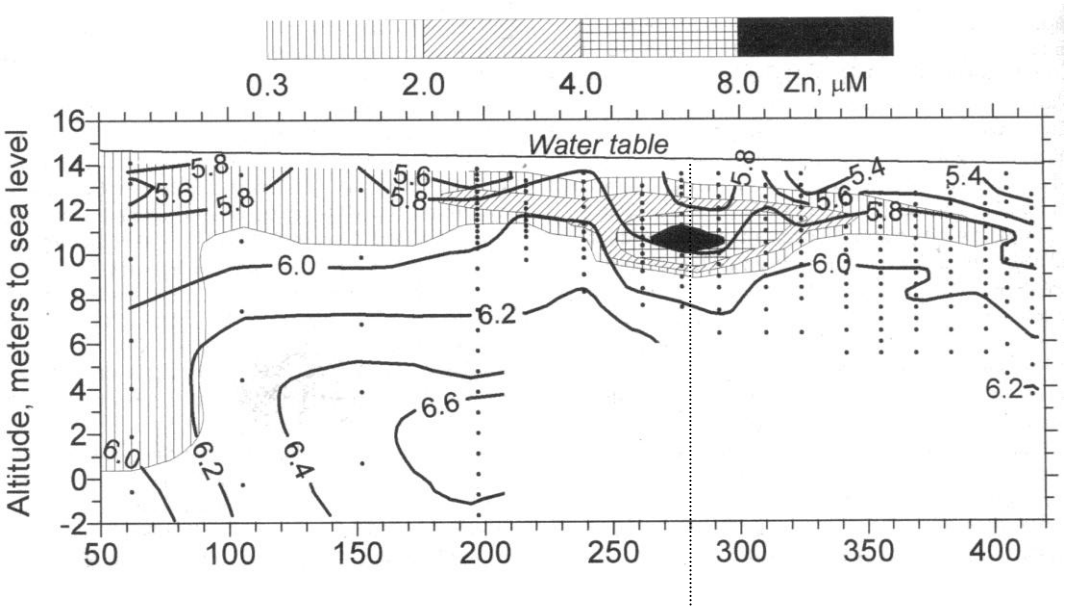

Fig. 6.3: Profile of dissolved Zn concentrations and pH contours from 1997 (see Fig. 6.2 for line of section beginning at S469). From /KEN 00/

6.4 Distribution of pH-Value

Contour lines in Fig. 6.3 show the distribution of pH-values in the Zn-contaminated region. While recharge of uncontaminated water resulted in a pH-value of about 5.6 the contamination raised the pH-value above 6.6. Spreading of the zinc with the groundwater flow was apparently correlated with a regime of ph-values less than 6. The Zn- and pH-profiles of some test wells downstream - shown in Fig. 6.4 - confirm this correlation.

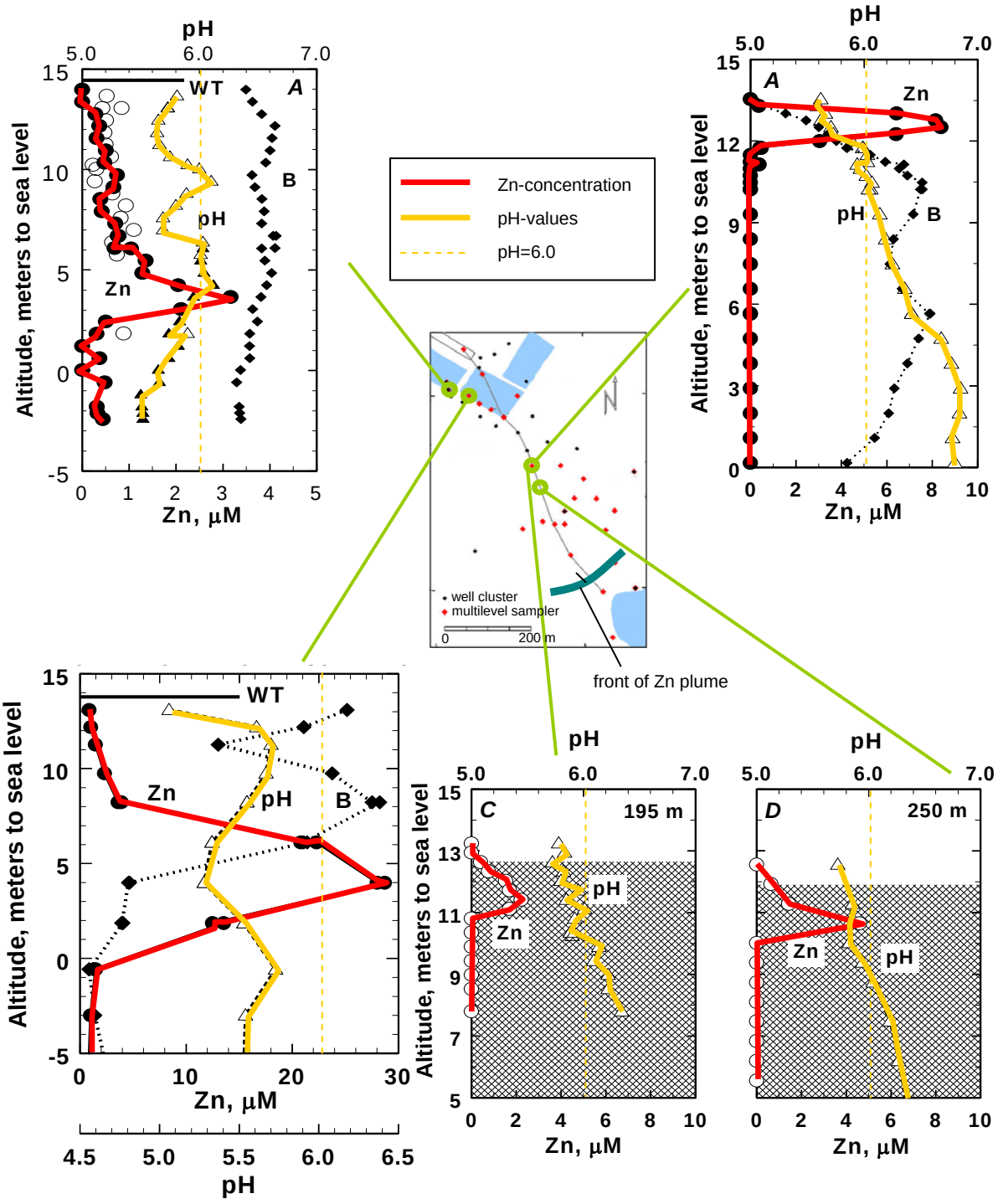

Fig. 6.1: Location of test wells and measured Zn- and pH-profiles modified from /KEN 00/

6.5 Numerical Modelling

6.5.1 Two-dimensional Groundwater Flow

Seasonal variations in the water table and the flow direction are small enough to allow an approximation of the true flow conditions as a steady-state flow. Thus, only the permeability and the boundary conditions are required to describe the flow field.

The horizontal dispersion appears to be sufficiently small (c.f. chapter 6.5.2) to reduce the spatial domain to a two-dimensional vertical cross-section without loosing too much accuracy. The top boundary is supposed to be identical with the water table. Water from precipitation enters the aquifer here. The bottom boundary is assumed to be a no-flow boundary. From the left hand side the contaminated water enters the domain horizontally thus assuming that the effluent from the disposal beds is outside the domain already completely mixed with the pristine groundwater. At the right side boundary the water leaves the domain.

Different authors have adopted this model but used slightly differing input data. The data used in the literature as well as the data used for the present model are compiled in Tab. 6.1 and partially visualised in Fig. 6.5. The resulting flow field is shown in Fig. 6.6.

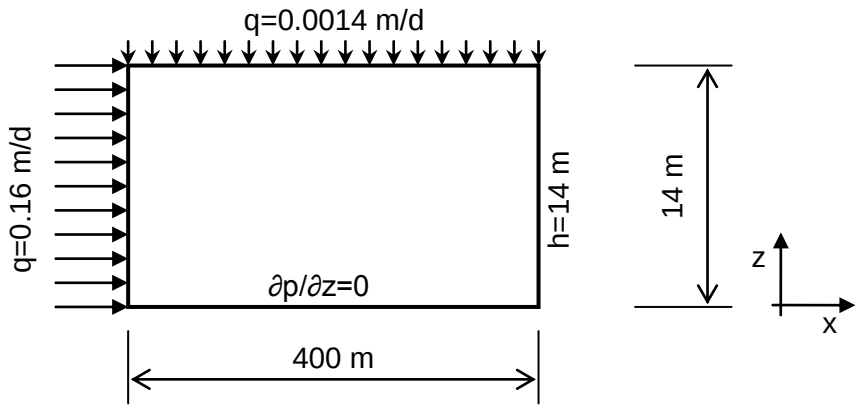

Fig. 6.5: Conceptual flow model

Tab. 6.1: Data for the flow model

quantity	value	source	adopted value
horizontal conductivity	110 m/d 95 ± ½ m/d 106.1 m/d 94.5 m/d	/KEN 00/ /DAV 00/ /ZHA 98/ /ZHA 98/	110 m/d
vertical conductivity	31.4 m/d 89 m/d 76.2 m/d	/KEN 00/ /ZHA 98/ /ZHA 98/	50 m/d
porosity	0.39	/DAV 00/ /ZHA 98/	0.39
viscosity	0.001002 Pa s	/ZHA 98/	0.001002 Pa s
density	998.2 kg/m³	/ZHA 98/	998.2 kg/m³
matrix compressibility	10^{-8} m²/N	/ZHA 98/	0
water compressibility	$4.8 \cdot 10^{-10}$ m²/N	/ZHA 98/	0
inflow rate (left side)	$1.85 \cdot 10^{-6}$ m/s $1.81 \cdot 10^{-6}$ m/s	/KEN 00/ /ZHA 98/	$1.85 \cdot 10^{-6}$ m/s
inflow rate (top side)	$1.62 \cdot 10^{-8}$ m/s $2.6 \cdot 10^{-8}$ m/s	/KEN 00/ /ZHA 98/	$2.0 \cdot 10^{-8}$ m/s
lower boundary	no flow	(all sources)	no flow
hydraulic head (right side)	h=14 m	/KEN 00/ /ZHA 98/	hydrostatic

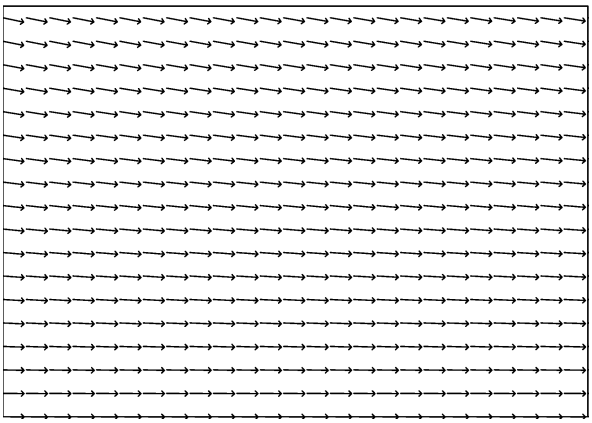

Fig. 6.6: Steady-state flow field

6.5.2 Two-dimensional Zinc Transport

6.5.2.1 Processes

In all modelling efforts zinc has been fed to the modelled domain by using a constant Dirichlet boundary condition at the left hand side boundary. Temporal variations of this value were not considered. In the present model a value of 2 µM is assigned to this boundary for 59 years of model time. Afterwards this value is set to zero assuming instantaneous cessation of contamination.

Spreading of zinc in the modelled domain is controlled by three effects:

- mixing of the contaminated water with the pristine water coming from the surface,
- hydrodynamic dispersion and
- pH-dependent sorption.

Mixing is automatically taken care of by the conservation equations for flow and transport. Hydrodynamic dispersion and pH-dependent sorption are discussed in the following subsections.

6.5.2.2 Hydrodynamic Dispersion

A value for the diffusion coefficient is provided only by /ZHA 98/: $D = 1.48\ 10^{-9}$ m²/s. More data exists on dispersion lengths which are compiled in Tab. 6.2. The transverse dispersion length is rather small in comparison to the longitudinal dispersion length.

This apparently follows from the fact that sharp horizontal Zn concentration gradients were observed transverse to the flow direction /KEN 00/.

Tab. 6.2: Dispersion lengths for the transport model

dispersion lengths	value	source	adopted value
longitudinal	0.96 m 1.1 m 0.67; 0.96 m	/KEN 00/ /HES 99/ /ZHA 98/	1.00 m
transversal (horizontal / vertical)	1.5 mm 1.5 cm / 3.8 mm 1.8 cm / 1.5 mm	/KEN 00/ /HES 99/ /ZHA 98/	0.01 m

6.5.2.3 Dynamic pH-Conditions

Pristine groundwater and water coming from the surface have a pH-value of about 5.6 as shown in Fig. 6.3 and in Fig. 6.4. In the models of /KEN 00/ and /ZHA 98/ a value of 5.65 is used.

The pH-value of the groundwater downstream of the sewage plant is influenced by the effluents and changes with depth. Neither the pH-values nor the equivalent proton activities[1] of the water entering the domain over the left hand side boundary are given explicitly in the literature. The only hints can be found in figures showing the simulated pH-values like in /KEN 99/, see Fig. 6.7.

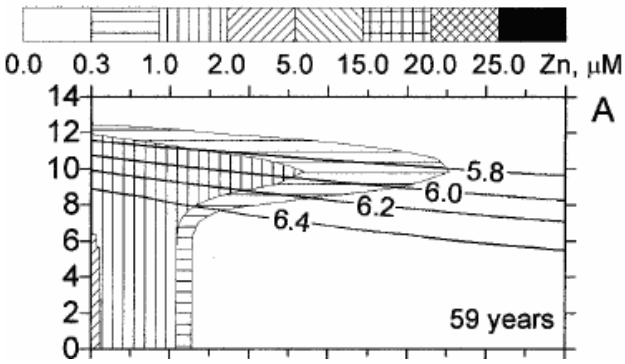

Fig. 6.7: Zinc concentration and pH-values after 59 years /KEN 00/

[1] The pH-value is defined as the negative common logarithm of the proton activity in [M].

In the present model the proton concentration is used as a primary variable for the modelling instead of pH-values because the pH-value is not an extensive quantity. For simplification the proton concentration is chosen. This is possible since it is assumed that the ionic strength in the whole is constant in space and time with I= 0.01 mol l^{-1}. In this case the proton concentration is directly proportional to the proton activity. The proton concentration at the left hand side boundary is assumed to change piecewise linear with depth. The data as taken from Fig. 6.7 and used in the model is summarised in Tab. 6.3. The protons are assumed to be transported like a tracer, being subject to dispersion but not to retardation, i.e. buffering of pH by the sediment is neglected. After a model time of 59 years the equivalent to a pH-value of 5.65 is applied uniformly along the left hand side boundary.

Tab. 6.3: pH-conditions at the left hand side boundary in the model

height [m]	pH-value [-]	proton concentration [M]
0.0	6.5	3.16E-7
9.0	6.5	3.16E-7
12.0	5.8	1.58E-6
14.0	5.65	2.24E-6

6.5.2.4 pH-dependent Sorption

The reason for the retardation of the zinc is sorption on the surface of the sediment. Equilibrium sorption can safely be assumed for the flow conditions at Cape Cod /KEN 99/. In combination with the fact that the amount of zinc adsorbed on the sediments amounts to less than one tenth of the saturation value, the adsorption process appears to be well described with the K_d-concept. The distribution coefficient K_d is defined as 6.1

$$K_d = \frac{c_{ad}}{C_l} \qquad (6.1)$$

K_d - distribution coefficient [m³ kg^{-1}]

c_{ad} - concentration of adsorbed zinc [mol kg^{-1}]

C_l - zinc concentration in the solution [mol m^{-3}][2]

where

$$c_{tot} = c_{ad} + C_l \frac{V}{M} \qquad (6.2)$$

c_{tot} - total zinc concentration [mol kg^{-1}]

M/V - sediment/water ratio [kg$_{matrix}$ m$^{-3}_{water}$]

It can be shown that the sorption of zinc is dependent on the pH-value of the groundwater[3]. In the pH-range considered here, the distribution coefficient increases with increasing pH-value. A correlation between the pH-value and a referring K_d-value can be derived from an adsorption isotherm which relates the concentration of adsorbed zinc to the pH-value.

Sorption experiments with zinc and sediment from Cape Cod were used to develop two non-electrostatic surface complexation models in order to predict this adsorption behaviour on a theoretical basis /DAV 98/. The sediment/water ratios M/V of the test material were chosen to be 400 kg/m³ and 50 kg/m³ corresponding to surface areas of 176 m² l^{-1} and 22 m² l^{-1} /DAV 98/.

The simpler of the chemical models - the “one-site model” - yields a curve independent of the zinc concentration and is less matching the more complex - “two-site model” - that includes such a dependency. The differences are shown in Fig. 6.8. However, the deviation between the two models decreases rapidly with increasing ph-value. For a Zn-concentration of 1 µM the deviation between the two models amounts to less than 50% in the pH-range of interest. This is assumed to be sufficient for a first approximation.

[2] Note, that lower and upper case letters “c” for the concentration refers to different dimensions.

[3] Zinc adsorption on the other hand changes the pH-level only slightly so that the effect of sorption on the pH-value is of secondary importance. It will thus not be considered here.

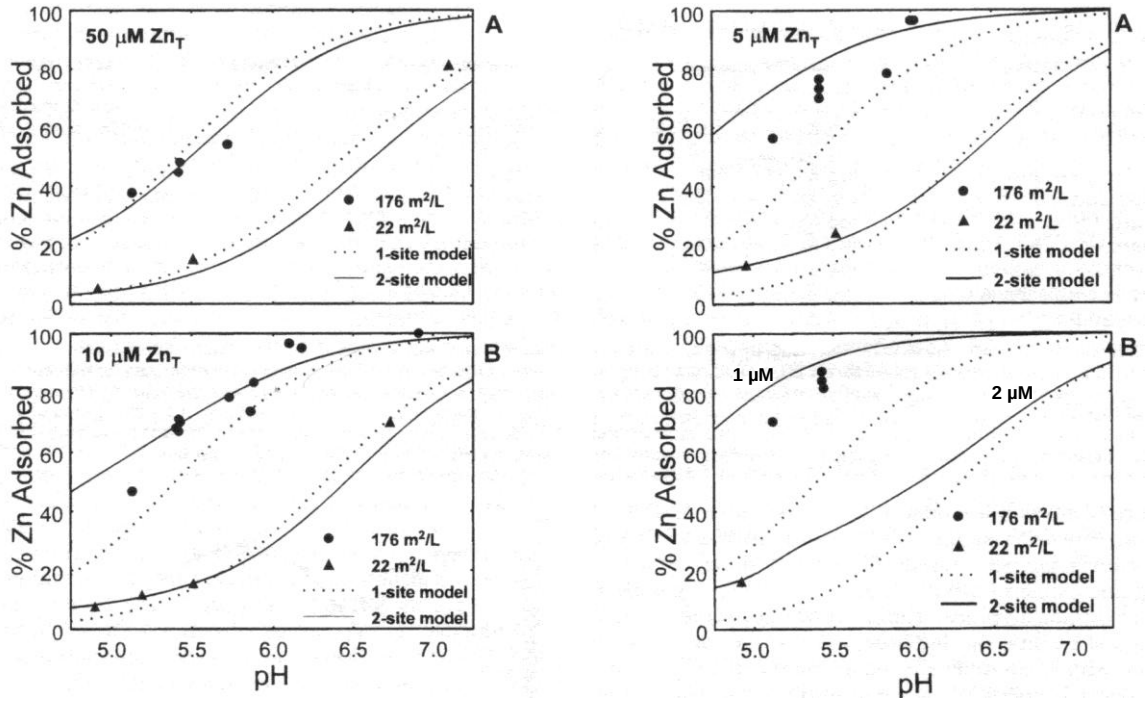

Fig. 6.8: Adsorption isotherms for zinc and Cape Cod sediments
From /DAV 98/

The curves presented in Fig. 6.8 are the result of a surface complexation model not yet implemented in r^{3}t, so an analytical function has to be found yet. For the task at hand it is not necessary to cover the whole adsorption isotherm from the one-site model in Fig. 6.8 but only the range of pH-values between 5.5 and 6.5. A third order polynomial is therefore fitted to this part of the isotherm for M/V = 400 kg m^{-3} (which better represents the field conditions than 50 kg m^{-3}) which reads:

$$x(pH) = \frac{c_{ad}}{c_{tot}} = 0.05682\, pH^3 - 1.25581\, pH^2 + 9.28878\, pH - 22.0 \qquad (6.3)$$

x - mass fraction of adsorbed zinc [-]

The quality of this approximation to the isotherm can be judged from Fig. 6.9. Elimination of the zinc concentration C_l in eq. (6.1) with the help of eq. (6.2) and subsequently the concentration c_{ad} with the help of eq. (6.3) finally yields the formulation (6.4) for the pH-dependent distribution coefficient. The resulting function for the distribution coefficient is given in Fig. 6.9.

$$K_d = \frac{x}{(1-x)} \frac{V}{M} \qquad (6.4)$$

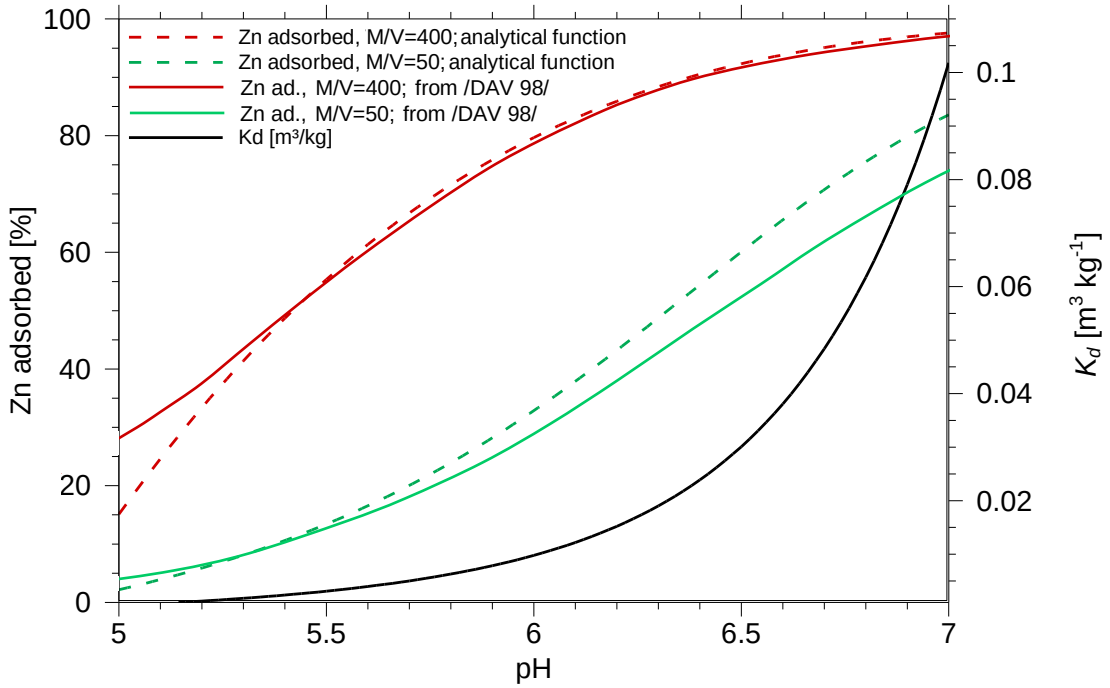

Fig. 6.9: Approximation of the adsorption isotherm

Using the analytically derived K_d-data the consistency of this approach can be checked by back calculating the function $x(pH)$ for the ratio M/V = 50 kg m^{-3}. The resulting curve is shown in Fig. 6.9, too. A comparison with the curve calculated by the chemical model of /DAV 98/ shows a satisfying agreement.

6.5.3 Three-Dimensional Model

Rather little is to be considered if the model geometry is changed from 2-D to 3-D because the vertical cross-section discussed above is only to be extended transversally to the flow direction. The flow field is not changed by this because flow parameters and boundary conditions remain in 3-D the same as in 2-D.

Transport parameters do not change either. Only the conditions at the inflow boundary are a little bit more complicated. In order to encompass the whole contaminant plume in the transverse horizontal direction the model has to be wider than the width of the sewage plant. The inflow boundary conditions of the 2-D model are applied everywhere along the perimeter of the plant. The zinc concentration at the remaining inflow boundary is set to zero.

For symmetry reasons only half of the system needs to be modelled. First test calculations showed, though, that the 3-D effects of transverse dispersion are very localised. A rather narrow cut-out section of the domain suffices to cover the transverse spreading zinc plume completely. Therefore geometry is chosen according to Fig. 6.10.

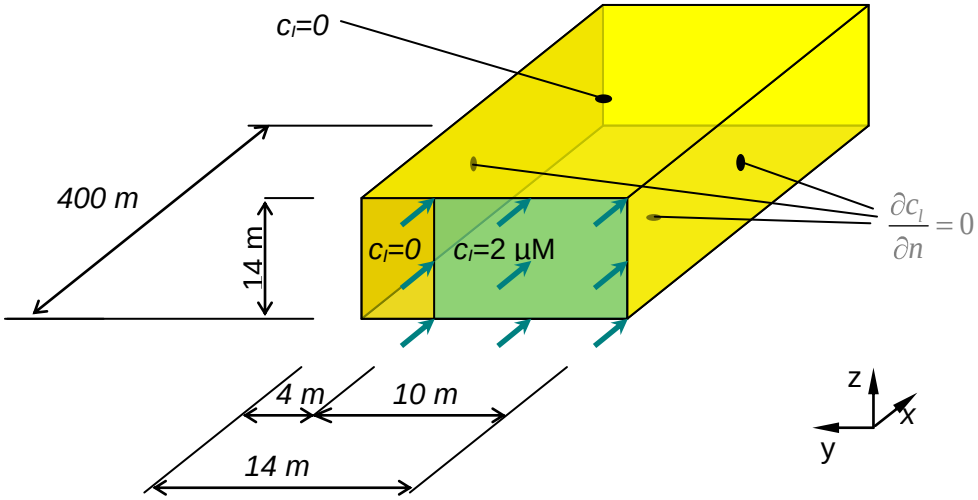

Fig. 6.10: Geometry and boundary conditions for Zn-transport in the 3-D model

6.6 Results

6.6.1 Two-Dimensional Model, Simulation until Plant Shutdown

The development of the zinc plume and the pH-distribution until closure of the sewage plant after 59 years of operation is illustrated in Fig. 6.11 and Fig. 6.12. In contrast to proton transport migration of zinc is impeded by sorption. Steady-state conditions with respect to proton transport are thus reached within little more than 3 years while the zinc plume does not even reach the right hand side of the domain after 59 years. Transport of zinc is much slower than the changes in the pH-values, so that the zinc always travels in a steady-state pH-condition.

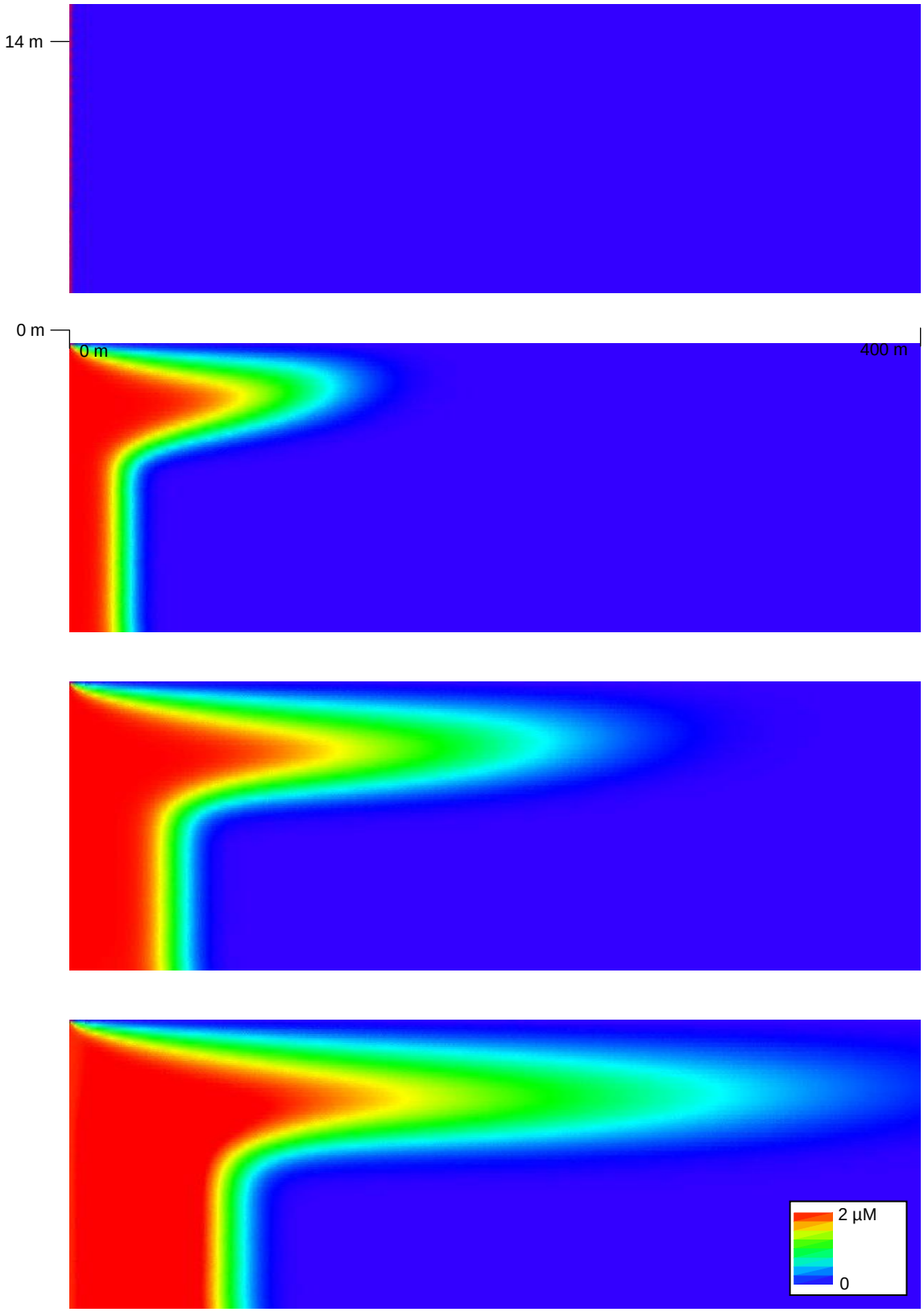

Fig. 6.11: Simulated zinc concentrations after 0, 20, 40 and 59 years

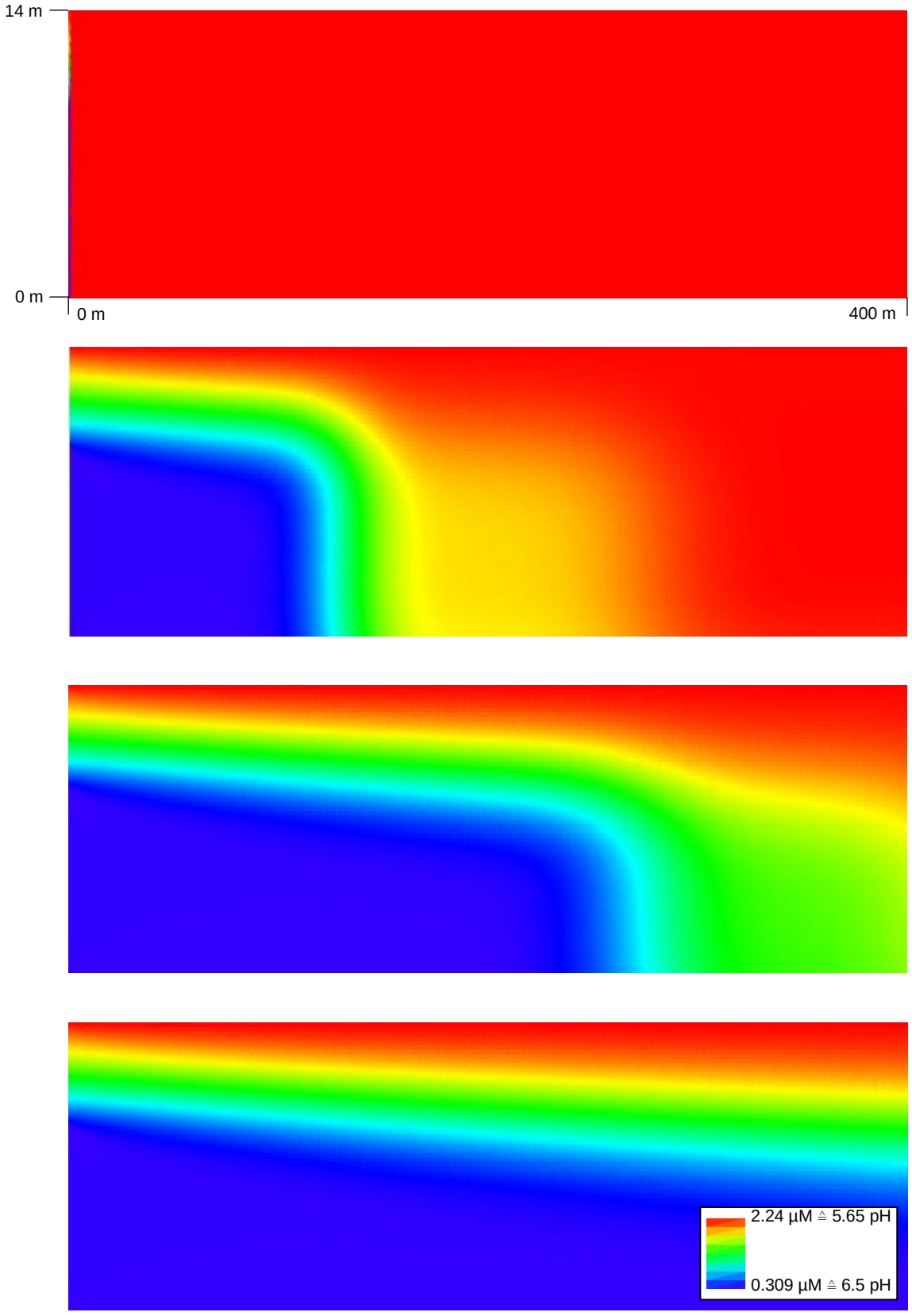

Fig. 6.12: Simulated proton concentrations after 0, 1, 2 and 3.5 years

The two subdomains of different pH-values - and thus of different Zn transport velocities - can clearly be distinguished.

Fig. 6.13 demonstrates the correlation of low pH-values with a high transport velocity and vice versa at 59 years model time. Downwards directed transport due to the recharge is discernable at the top of the model, too.

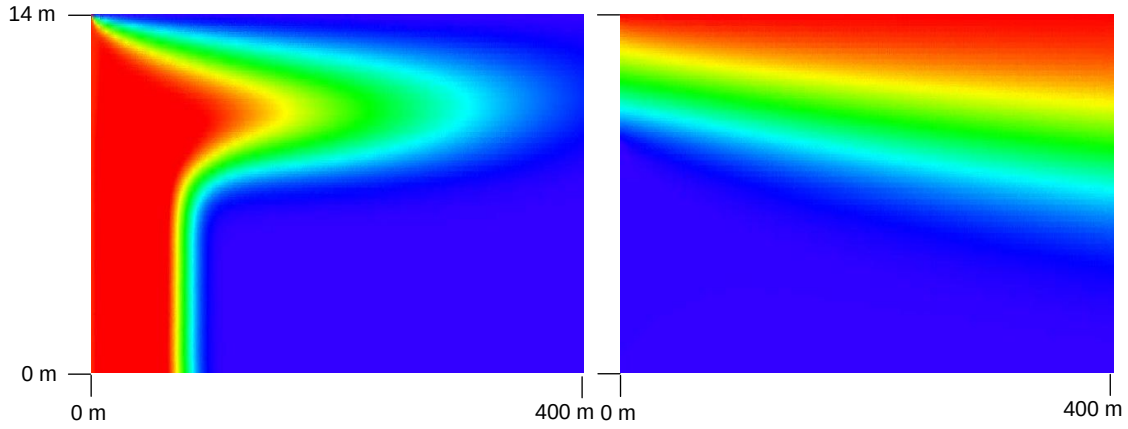

Fig. 6.13: Zinc concentration and pH-values after 59 years

Qualitatively, the model results compare well with the results of /KEN 00/. Fig. 6.14 shows the calculated zinc concentrations after 59 years of contamination. The colours refer to the results of r^3t, isolines represent 0.3 µM and 1.0 µM in the model from /KEN 00/. Both models result in a wedge-shaped plume in the upper half of the model and a more or less uniform vertical concentration profile in the lower half of the model.

The most apparent difference is that zinc moves in the r^3t-model not as fast as in the model from /KEN 00/. This may be attributed to the different degrees of accuracy at which sorption is taken into account in the models. Of course, it has to be shown, too that the assumption of no pH buffering by the sediments is reasonable. However, the effect of the pH-dependent sorption on the zinc transport has been captured.

A minor difference is caused by the upstream boundary condition for zinc which has been applied to whole left hand side boundary in the r^3t-model while in the model from /KEN 00/ the uppermost node were left out.

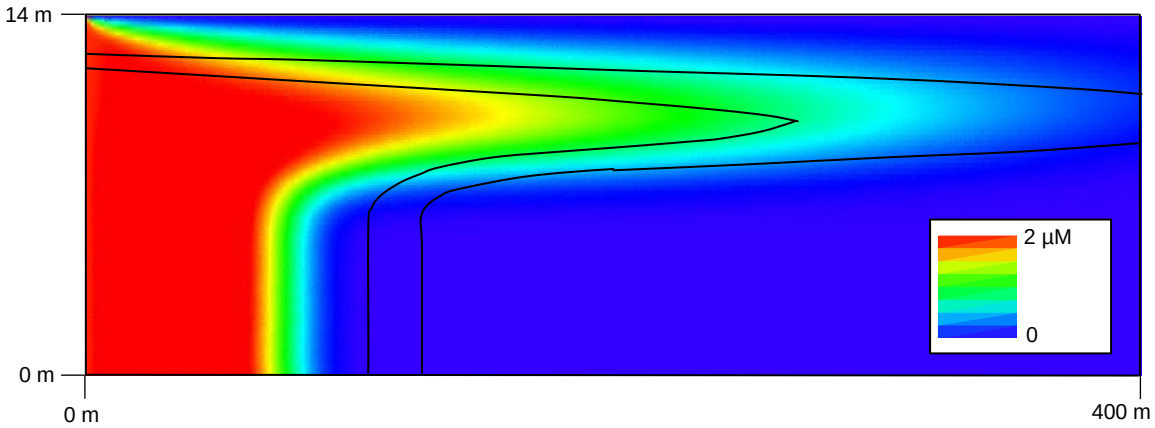

Fig. 6.14: Zinc concentration after 59 years from r^3t and from /KEN 00/
Colours refer to the results of r^3t,
isolines represent 0.3 and 1.0 µM in the model from /KEN 00/

6.6.2 Two-Dimensional Model, Simulation after Plant Shutdown

In the r^3t-model it is assumed that zinc ceases to pollute the groundwater after 59 years of model time. This terminates the zinc plume. At the same time the pH-value switches back to uncontaminated conditions. This affects the zinc plume since the front of decreased pH-values migrates faster through the domain than the zinc plume.

According to eq. (6.4) the distribution coefficient for zinc is directly proportional to the pH-value and is thus lowered at the source after 59 years, too. Zinc adsorbed during the contamination will therefore be partially desorbed when the pH-value drops. This increases the zinc concentration in the solution above the value formerly assigned to the inflow boundary[4]. During the time of pH-front movement along the Zn contaminated area the tail of the plume moves faster than the head due to the reduced retention. After pH decrease in the whole area Zn plume travels with uniform velocity. The mobile Zn concentration is increased far above the value observed before the plant shutdown. Fig. 6.15 illustrates this mechanism. This is the way in which the pH-dependent zinc transport is presently modelled with r^3t. Results are given in Fig. 6.16 and Fig. 6.17. In order to ease readability of the plots the same colour code is used as in the previous figures. Maximum values reach 13.5 µM, though.

[4] A short-term decrease of pH-value during operation is suspected to have caused the anomalously high zinc concentration at 280 m downstream /KEN 00b/.

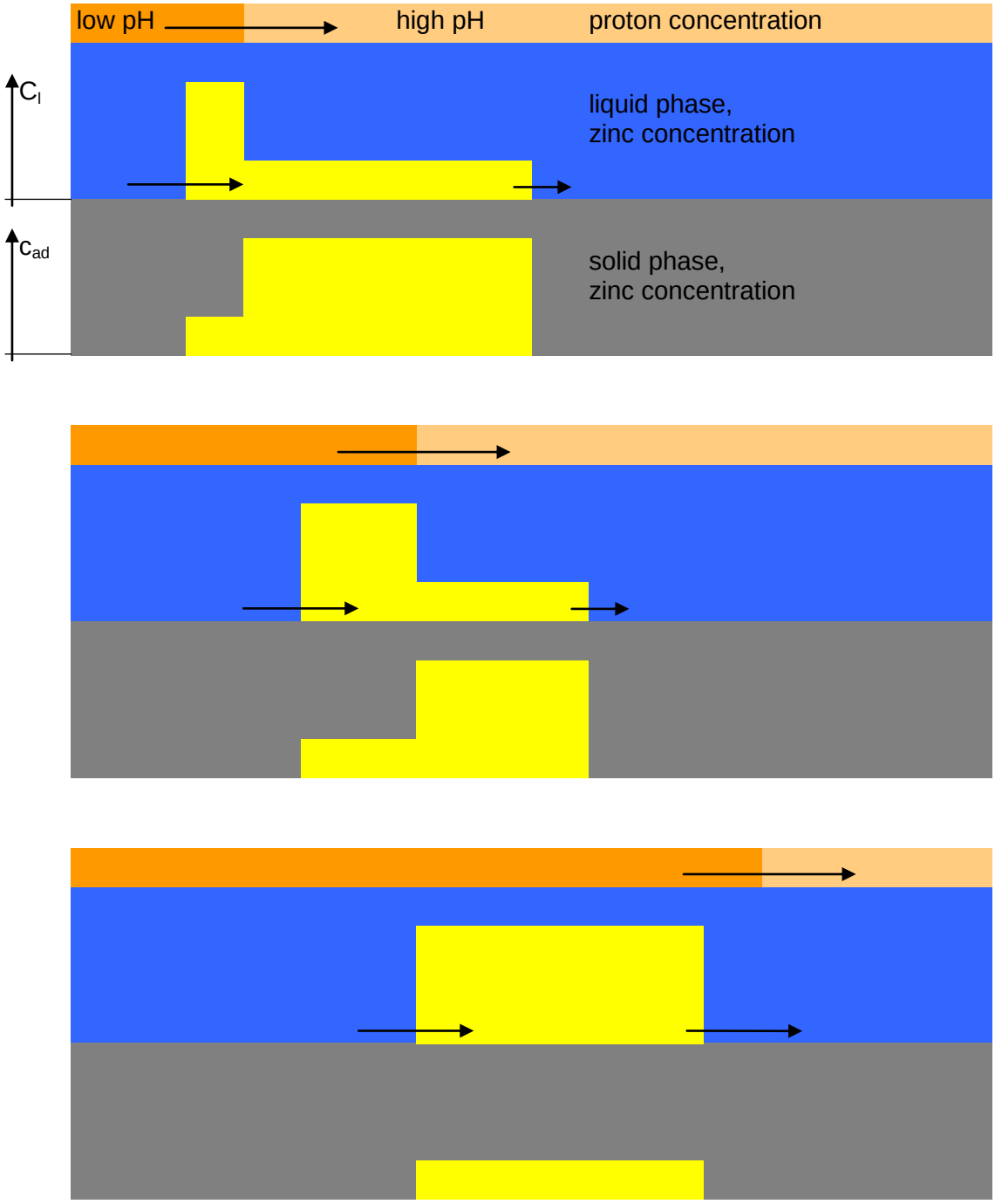

Fig. 6.15: Transport and distribution of Zn between liquid and solid phase during pH front movement through the Zn contaminated area

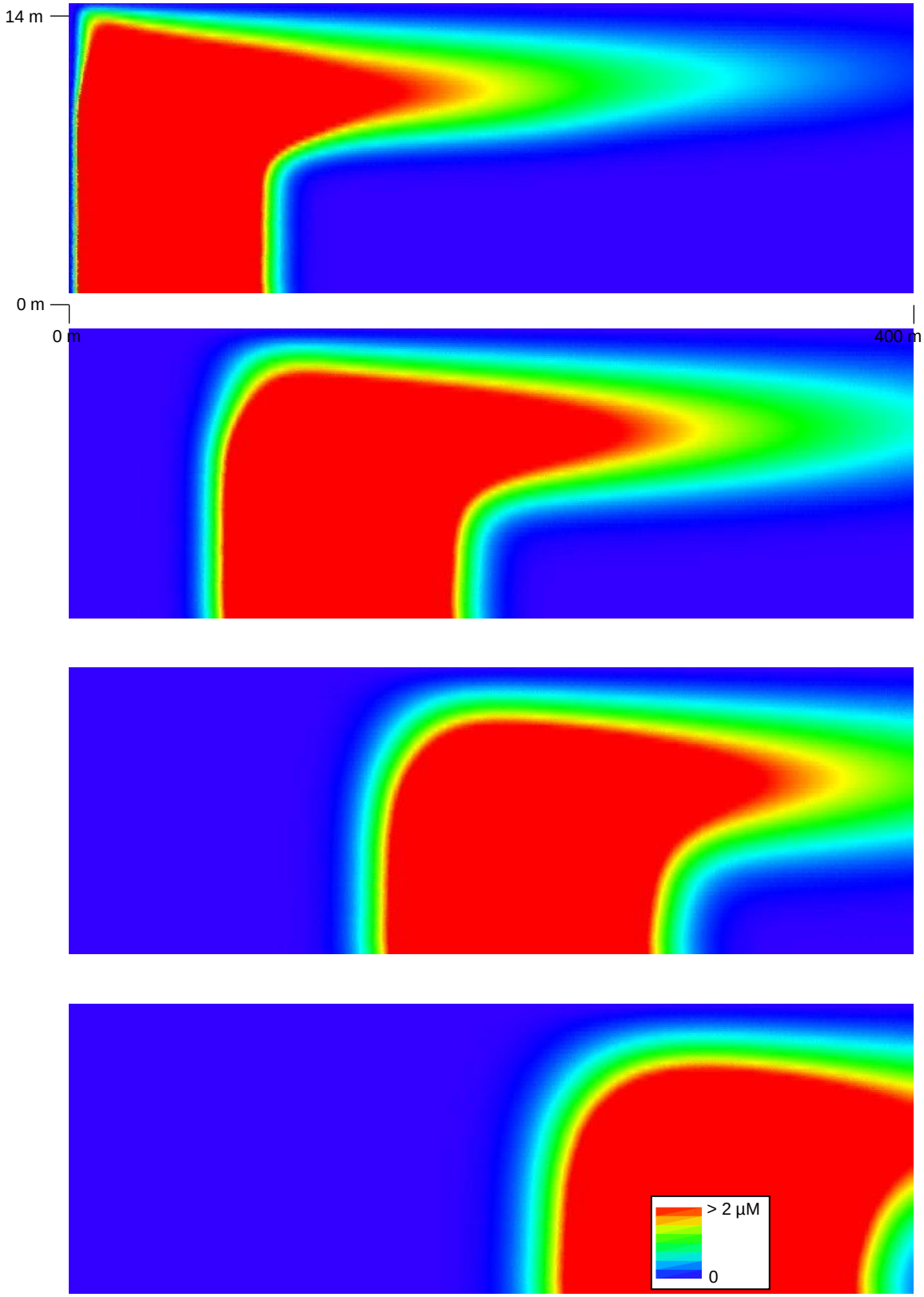

Fig. 6.16: Simulated zinc concentrations after 60, 70, 80 and 90 years

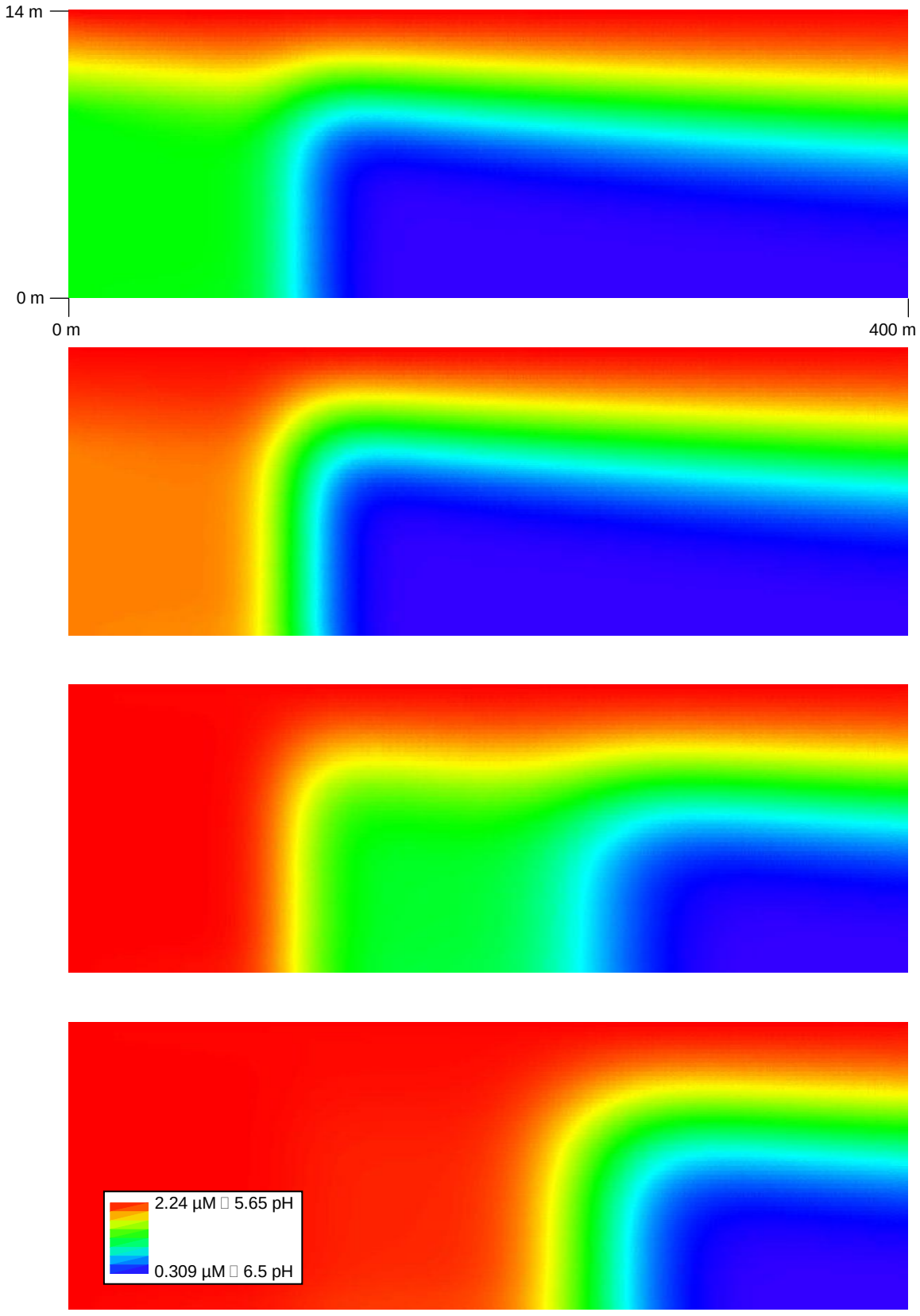

Fig. 6.17: Simulated proton concentrations after 59.3, 59.6, 60.1 and 60.5 years

A comparison of the results with the model results from /KEN 00/ after 75 years model time is given in Fig. 6.18. The zinc plume in the r^3t-model moves still behind the plume

in the model of /KEN 00/ with about the same offset as after 59 years. The maximum concentration is different, too: about 13 µM in the r^3t-model and more than 20 µM in the model of /KEN 00/. However, the form of the zinc plume appears to be very similar in both models.

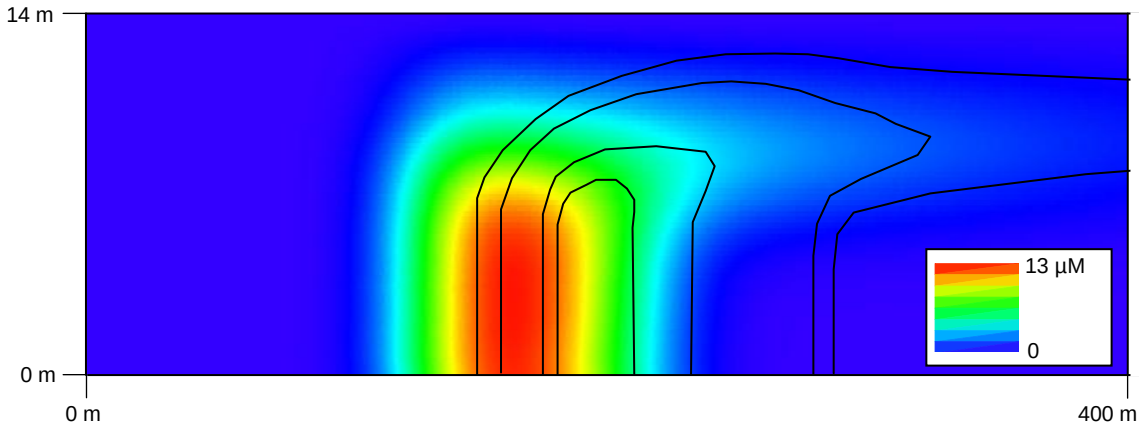

Fig. 6.18: Zinc concentration after 75 years from r^3t and from /KEN 00/
Colours refer to the results of r^3t,
isolines represent 0.3, 2, 15 and 20 µM

Sorption of zinc onto the solid surface is more complicated than presently modelled in r^3t. In the adsorption process a proton is released. Thus, the pH-values are changed by this process, too, with the accompanying changes of the distribution coefficient. Since the whole phenomenon depends strongly on the non-linear relation (6.4) the development of the zinc concentration can hardly be predicted without adequate numerical models.

An indication of these dynamics for the Cape Cod site is given by results of a code coupled with a surface complexation model that takes into account the feedback of desorption on the pH-value. Fig. 6.19 shows the development of the zinc plume as well as the distribution of pH-values after closure of the sewage plant. Apparently, changing of the pH-conditions is impeded by the zinc plume as shown in /KEN 00/. As a result maximum concentration in the plume is reached only after several years (plot C of Fig. 6.19) in contrast to the r^3t results where this maximum concentration is reached within several months of simulation time.

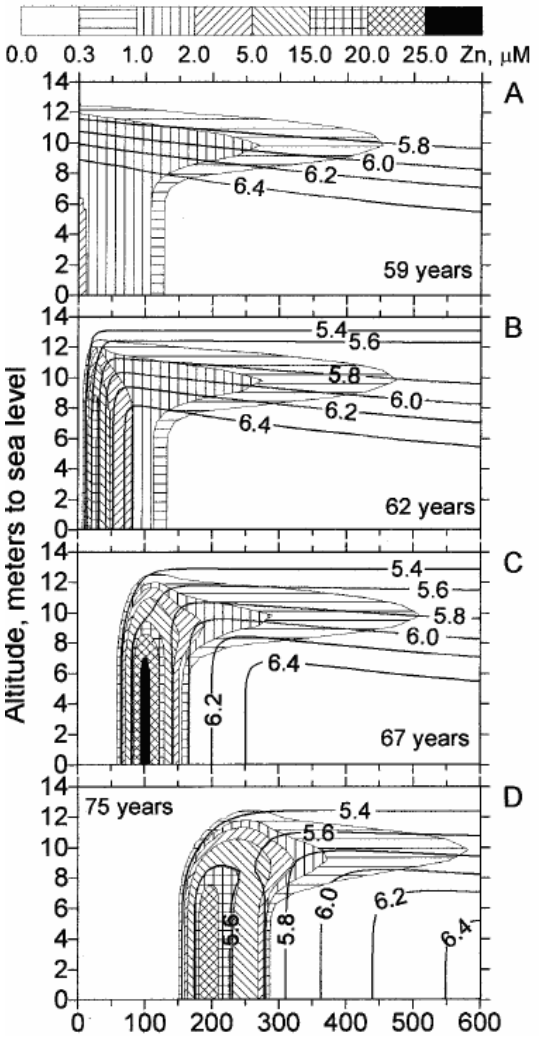

Fig. 6.19: Zinc transport and evolution of groundwater pH after plant closure from /KEN 00/

6.6.3 Comparison of r^3t results with field data

Finally, a comparison between the results of the model and the measurements at the site in 1997 - two years after shutdown of the facility - is given in Fig. 6.20. While the simulated zinc plume shows the same characteristic form as the measured one the agreement is not entirely satisfying:

- the faster moving part at the top of the plume lies too low and is too thick in the model,
- the slower moving part is too fast and
- in reality the increase of zinc concentration due to the changing pH-milieu has not reached as far downstream as 50 m two years after plant shutdown while the model already yields values up to 13.5 µM.

However, the penetration depth of zinc into the domain appears to be in rather good agreement with the measurements.

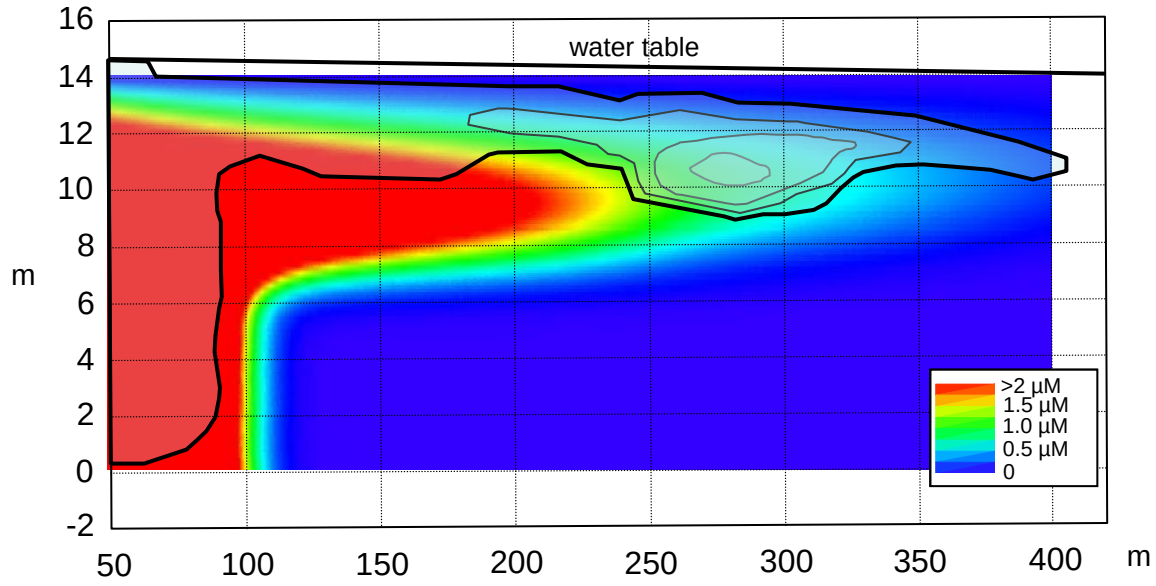

Fig. 6.20: Zinc concentration after 61 years with pristine water conditions measurements from /KEN 00/ (isolines representing 0.3, 2, 4 and 8 µM concentration) and r^3t-model (results in colour)

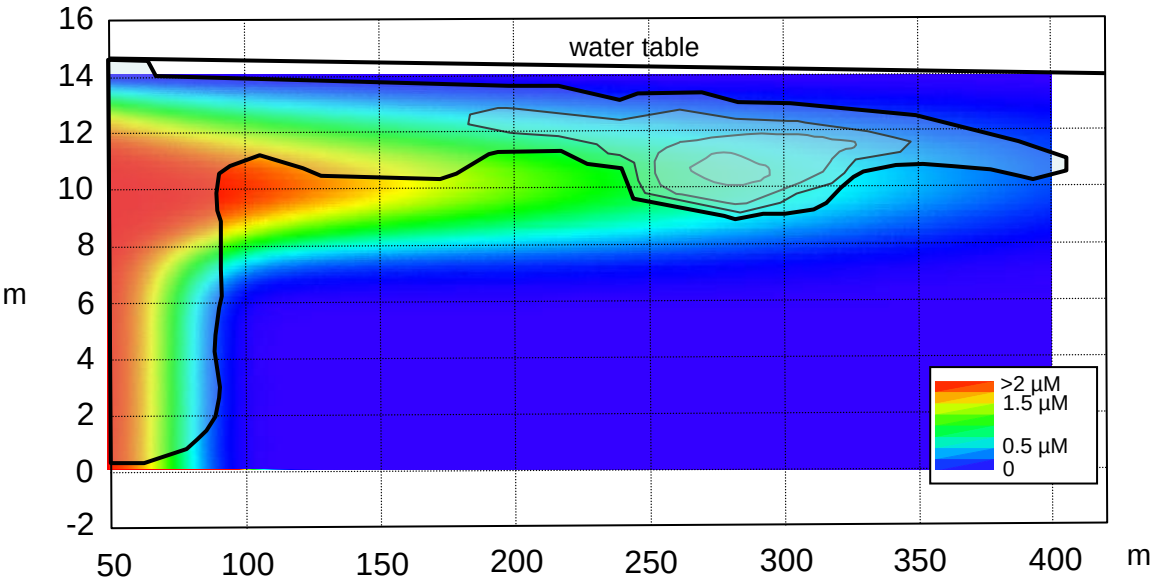

Fig. 6.21: Zinc concentration after 61 years with sustained pollution conditions Measurements from /KEN 00/ (isolines representing 0.3, 2, 4 and 8 µM concentration) and r3t-model (results in colour)

A much better agreement of model and measurement yields a model that simply sustains the polluting conditions of the sewage plant beyond actual operation on account of ongoing contamination from the disposal beds after shutdown of the facility as shown in Fig. 6.21:

- the faster moving part on top of the plume has become narrower,
- the slower moving part fits quite well the measurements and
- the maximum zinc concentration is far better met without change of the pH-condition.

Apparently, either the pH-controlling processes were still active for some time after shutdown of the disposal plant or the changes in the pH-condition due to shutdown did not propagate downstream unretarded or both. It is thus highly probable that it takes several years of low pH-conditions to produce a zinc concentration peak as the one observed at 280 m downstream.

6.6.4 Three-Dimensional Model

Switching over to three-dimensional considerations basically just adds horizontal dispersion to the two-dimensional model. This means that the contaminated water entering the model at 0 m $\leq$ y < 10 m intermixes now laterally with the pristine water entering at 10 m $\leq$ y $\leq$ 14 m, and thus the zinc plume spreads out laterally beyond y = 10 m. In the transition zone between fully contaminated water and pristine water the increase of the pH-values is less pronounced than in the core of the contamination plume. Zinc is therefore much faster transported in this transition zone than in the middle of the plume.

Fig. 6.22 and Fig. 6.23 show the zinc concentration after 59 years model time in vertical and horizontal cross-sections along the flow direction. Apparently, the small transverse dispersion length lets the transition zone expand only over a few metres width within the time period of interest. The rest of the zinc plume shows the same characteristic shape as in the 2-D model.

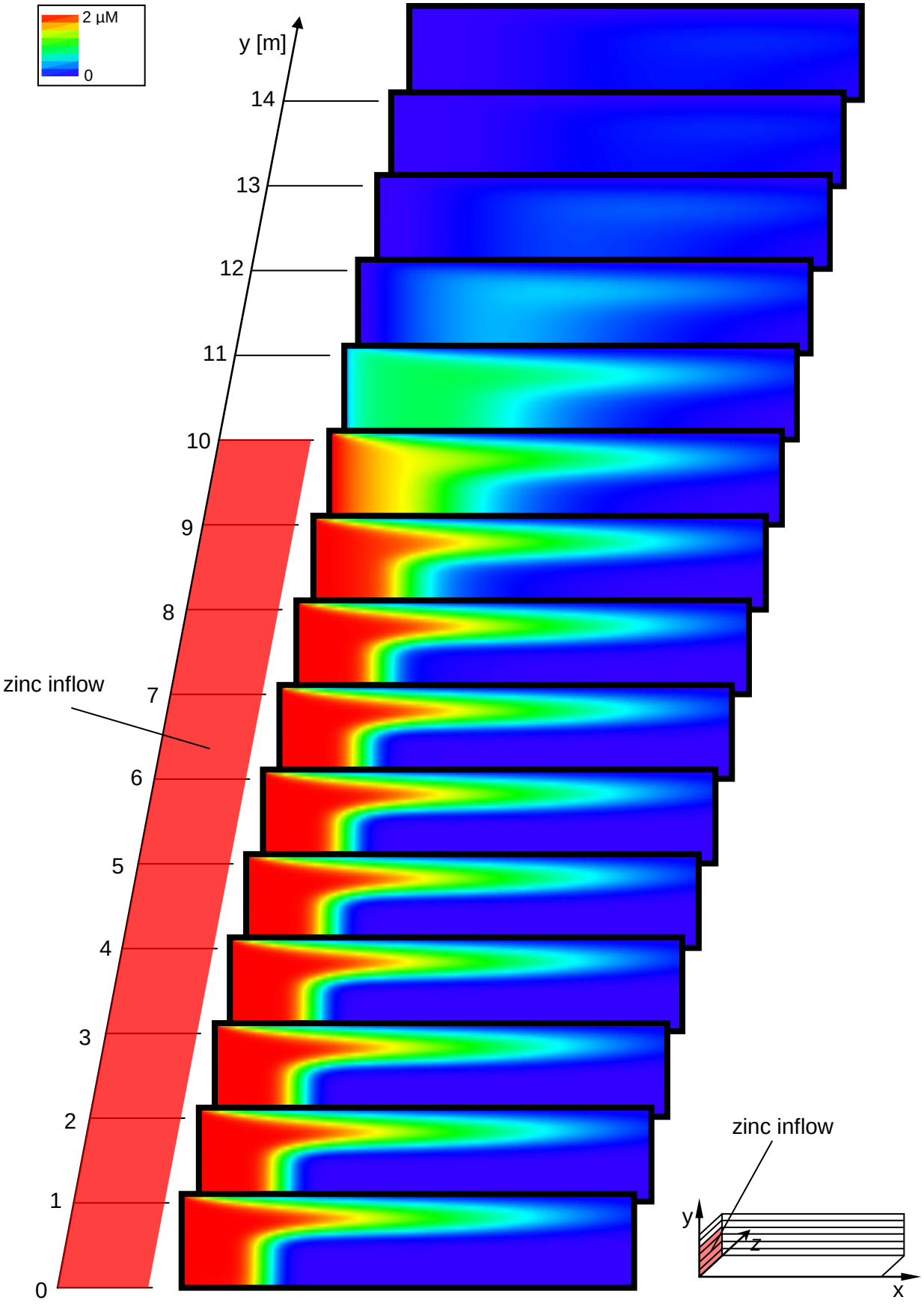

Fig. 6.22: Zinc concentrations at 59 years in vertical cross-sections

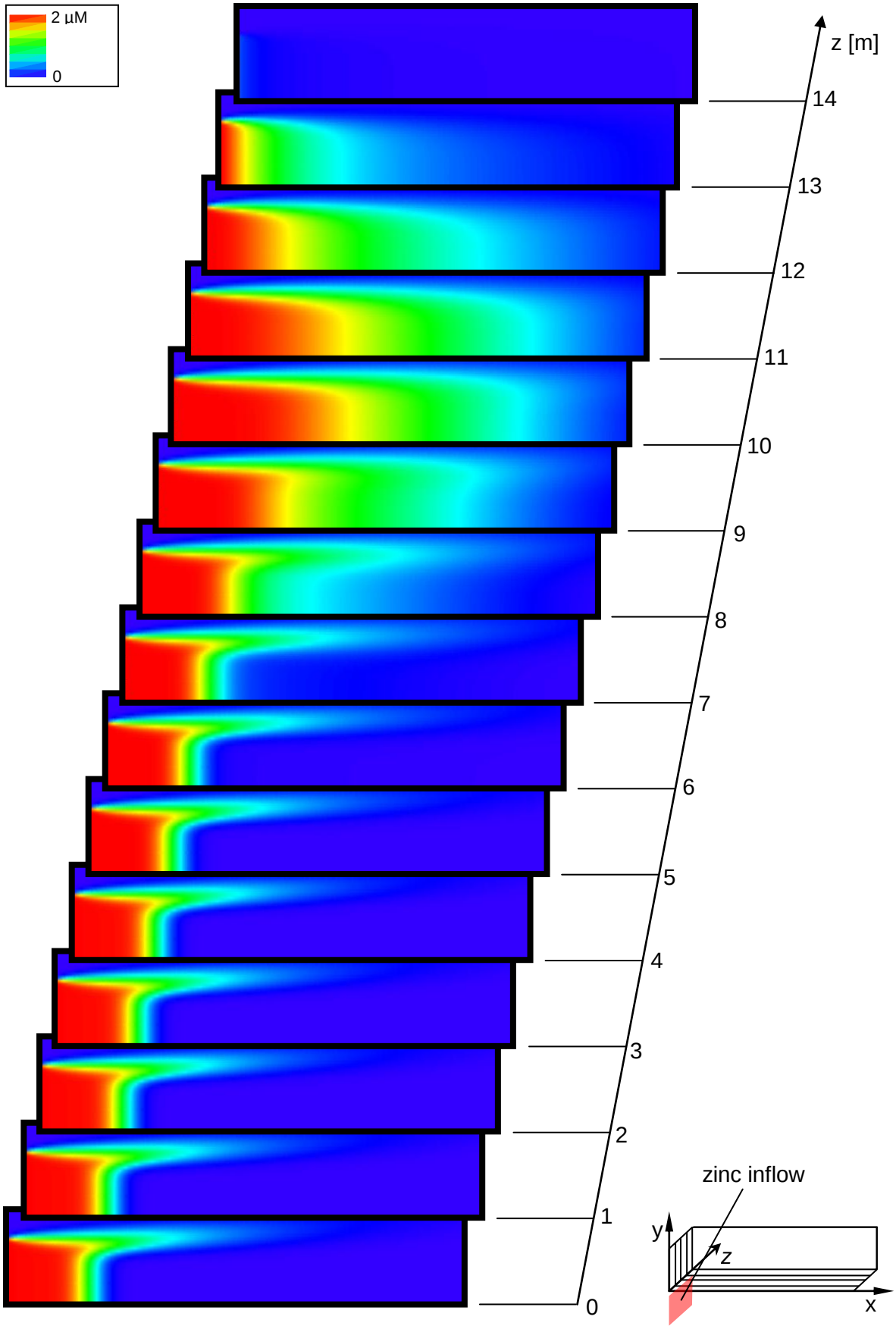

Fig. 6.23: Zinc concentrations at 59 years in horizontal cross-sections

6.7 Conclusions

Modelling zinc transport at Cape Cod appears to be a most challenging task. A key process to explain the characteristic form of the zinc plume is the pH-dependent sorption of zinc. In the past a lot of effort has already gone into the numerical description of this effect and surface complexation models have been developed so far. Nevertheless, no numerical model up to now simulates the zinc transport at Cape Cod satisfyingly well. The results of the r^3t-model can therefore not be expected to reproduce the measurements exactly.

This can be understood in the light of the simple set-up of the r^3t-model and the other models. Possibly critical simplifications for the 2-D model include

- the rectangular model geometry,
- the assumption of a constant effluent rate into the ground,
- the assumption of complete mixing of Zn under the sewage disposal beds,
- the assumption of parallel horizontal flow under the sewage disposal beds,
- isotropy and homogeneity of the flow and transport parameters and
- the assumption that the pH-value changing quantities can be transported with the flow without impact of other reactions, i.e. by zinc adsorption and buffering by the sediment (at least in case of the r3t-model).

Further adjustments of the model could most certainly improve the agreement between measurements and model results. However, the most meaningful check of the r^3t-results with respect to the treatment of sorption is a comparison with results of other models. A qualitative comparison is possible for the 2-D models even if those models incorporate sorption in a different way.

The comparison of the 2-D models clearly shows that the pH-value dependent retardation of zinc is captured in the r^3t-model. This applies for the time during plant operation as well as for the subsequent period. The model simulated even the drastic increase of the zinc concentration after closure of the sewage plant caused by the drop of the pH-value.

Apart from the present work no 3-D simulation has yet been presented in the literature. Modelling results of r^3t in 3-D for the contamination at the sewage plant are indeed basically the same as for the 2-D model. The only exceptions are some very localised effects in the mixing zone of contaminated and pristine water. While the 3-D model has only an arguable value for interpreting the situation at Cape Cod it clearly shows the ability of r^3t to capture the pH-dependent transport behaviour of zinc even in 3-D.

7 Benzene Transport and Biodegradation at the Borden Site

The field research site is located at the Canadian Forces Base (CFB) Borden, approximately 80 km northwest of Toronto, Ontario, Canada. It is an abandoned sand quarry situated about 350 m north of a landfill that operated from 1970 to 1976. The aquifer is comprised of primarily horizontal, discontinuous lenses of medium-grained, fine-grained, and silty fine-grained sand, with silty clay and coarse sand layers also present /TEN 03/, /KIN 99/. These deposits are glacio-lacustrine in origin and grade into silts and clays at a depth of approximately 9 m.

CFB Borden is an extremely well studied site, perhaps it is the best-characterised sand aquifer in the world /MEL 00/. Over the past 25 years numerous experimental studies of subsurface organic contaminant behaviour have been conducted there. Additionally the Borden aquifer structure was determined statistically from detailed measurements of grain size. For these reasons the Borden test side was chosen to serve as an example of a highly permeable aquifer /GLE 99/.

7.1 Background

Methyl tertiary-butyl ether (MTBE) and ethanol were introduced as gasoline additives and are the most frequently used gasoline oxygenates. The original use of MTBE was to replace lead as an octane-enhancing additive, while ethanol was initially added to reduce reliance on oil imports. As of 1998, approximately 30 percent of all gasoline in the United States contained MTBE. This ether oxygenate was present in 80% of oxygenated fuels. Ethanol was used in approximately 15% of the oxygenated fuels.

MTBE is used throughout the year because it reduces gasoline volatility and is consequently useful for reducing the release of hydrocarbons through gasoline volatilization during summer months. Conversely, ethanol is generally used in winter months since it increases the vapour pressure of gasoline thereby increasing gasoline volatility.

Basically the petroleum hydrocarbon is released from oil production sites, and underground storage tanks (USTs). Chemicals of concern at these sites include benzene, toluene, ethyl benzene, xylenes (BTEX), total petroleum hydrocarbons, lead, and MTBE. Of these constituents benzene is known to be carcinogen and the others all pose health risks. Due to the toxic nature of the chemicals released and the fact that

many of these sites are located adjacent to residential properties or drinking water resources, the risk of a potential impact to human health is high. The potential way of human exposure to ethanol as oxygenate includes inhalation and the ingestion of contaminated groundwater.

The risk of exposure to gasoline oxygenates from the ingestion of contaminated groundwater increases with increasing length and size of the oxygenate plume. Additionally, gasoline additives including MTBE that can migrate beyond the benzene, toluene, ethylbenzene, and xylene (BTEX) plume, are more apt to escape detection because monitoring for gasoline oxygenates is less routine than BTEX monitoring. Hence, MTBE represents an increased risk to exposure relative to gasoline oxygenates that do not migrate to this extent.

Sources of subsurface contamination include pipelines, refuelling facilities, surface spills, precipitation, and especially underground storage tanks (USTs).

7.2 Biodegradation in the Presence of Ethanol

Since ethanol is rapidly metabolised, it is unlikely that ethanol will travel a substantial distance once spilled into the subsurface. Hence, ethanol itself likely poses little threat to contaminating drinking water wells. However, the potential of ethanol to decrease the biodegradation of BTEX hydrocarbons either by serving as a preferred substrate, or through the release of acetic acid during ethanol metabolism, merits additional consideration. Thus, some transport modelling was performed to predict the consequences of ethanol on the biodegradation and transport of benzene through aquifers contaminated with ethanol-blended gasoline. Benzene was selected as the model compound because it poses an increased risk due to its relatively high toxicity, resistance to biodegradation, and relatively high water solubility. So benzene is the most hazardous of the BTEX compounds. The modelling places emphasis on the influence that ethanol biodegradation has on the persistence of benzene. It was demonstrated /COR 98/, /HUB 94/ that ethanol is degraded much faster than BTEX when both are present and oxygen is available. The hypothesis is that most of the oxygen will be utilised by ethanol degraders rather than by BTEX degraders, thus slowing the biodegradation of benzene, when ethanol is present in the groundwater. Our model captures this aspect by using a biodegradation rate for benzene that depends on the concentration of ethanol.

7.3 Modelling of the Migration of Ethanol and Benzene

Here the complicated processes of anaerobic biodegradations are modelled in a simplified way using degradation (decay) constants. To include the interaction of benzene with ethanol and acetic acid the degradation rate of benzene was assumed to be dependent on the concentration of ethanol and acetic acid. In this test case we assume that concentrations of ethanol or acetic acid larger than $1 \cdot 10^{-6}$ mol m^{-3} cause the suppression of the biodegradation. In Tab. 7.1 the degradation products and the appropriate degradation and accumulation constants are compiled.

Tab. 7.1 Degradation- and accumulation rates

	degradation rate [s^{-1}]	accumulation rate [s^{-1}]
C_6H_6 ➔ NN benzene	$2{,}3 \cdot 10^{-8}$ if $\begin{cases} C_{CH_3-CH_2OH} \\ \text{or} \quad \leq 10^{-6} \text{ mol m}^{-3} \\ C_{CH_3-COOH} \end{cases}$ 0.0 else	---
CH_3-CH_2OH ➔ CH_3-COOH ethanol	$5.2 \cdot 10^{-6}$ $5.2 \cdot 10^{-7}$ (reduced degradation)	---
CH_3-COOH ➔ NN acetic acid	$1.6 \cdot 10^{-8}$	$5.2 \cdot 10^{-6}$ $5.2 \cdot 10^{-7}$

7.3.1 Flow Model

As already mentioned the Borden test site served as standard for the conducted modelling /GLE 99/. The hydrogeology of the site is relatively simple: it consists of a sandy layer. The two-dimensional model region covers an area of approximately 610 m × 610 m, cf. Fig. 7.1. Constant head boundaries are assigned to the south western corner and the north eastern corner. The head values amount approximately -0.3 m (-1 ft) and -4.0 m (-13 ft). All the rest of the boundaries are assumed impermeable. For the Borden site reliable hydraulic conductivity data are available /MAC 94/. The aquifer has a permeability of $7.06 \cdot 10^{-12}$ m^2 and a porosity of 0.33. This induces an overall gradient

of approximately $4.3 \cdot 10^{-3}$ m m^{-1} directing from southwest to northeast. The flow model data are assembled in Tab. 7.2.

Tab. 7.2: Parameters of flow model

size of model	610 m × 610 m
hydraulic conductivity K permeability k	$7.06 \cdot 10^{-5}$ m s^{-1} $7.06 \cdot 10^{-12}$ m^2
porosity	0.33
hydraulic head SW	-0.3 m
hydraulic head NE	-4.0 m

In Fig. 7.1 the model, the source location, and the boundary conditions are shown. Additionally the dimensioning of the modelled area is given.

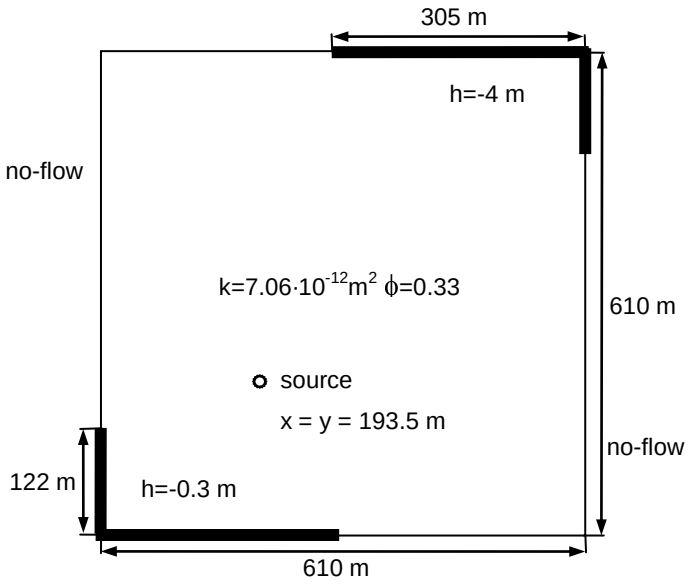

Fig. 7.1: Flow model and parameters

In Fig. 7.2 the calculated head distribution is depicted. In the bottom left and in the upper right corners the constant boundary heads of -0.3 m and -4.0 m can be seen. The contour lines are spaced equally with an increment of about 0.3048 m (1 ft).

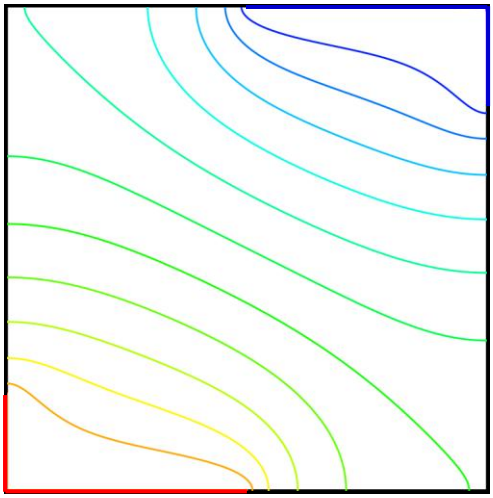

Fig. 7.2: Modelled hydraulic head
-0.3 m (bottom left), -4.0 m (right top), equal spacing (~0.3048 m)

Fig. 7.3 shows the steady state Darcy velocity field. The Darcy velocity in the centre of the modelled area is about $3.4 \cdot 10^{-7}$ m s^{-1} which means a displacement velocity of $1.03 \cdot 10^{-6}$ m s^{-1}.

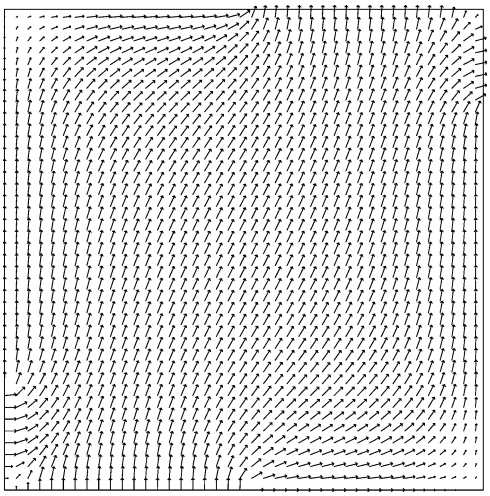

Fig. 7.3: Steady-state velocity field

7.3.2 Transport Model

Since ethanol is a preferred source for the microbial populations it is assumed that no benzene will be degraded where ethanol or acetic acid is available. Four different models were taken into account (cf. Tab. 7.3). The first model concerns the transport of benzene and ethanol without degradation. In this case there is no acetic acid which can be transported, because it is only generated by biodegradation of ethanol. The second comprises the transport of benzene and ethanol with degradation. Hence acetic acid is

transported, too. In this case the interaction of the degradation of benzene with the presence of ethanol or acetic acid is not considered. In contrast the third model includes this interaction. The fourth model is equal to the third, except that a smaller degradation rate of ethanol is considered.

Tab. 7.3: Various models

#	pollutants	details
1	C_6H_6 (benzene) CH_3-CH_2OH (ethanol)	injection without degradation
2	C_6H_6 CH_3-CH_2OH CH_3-COOH (acetic acid)	injection with degradation no interaction
3	C_6H_6 CH_3-CH_2OH CH_3-COOH	injection with degradation with interaction
4	C_6H_6 CH_3-CH_2OH CH_3-COOH	injection with degradation with interaction smaller ethanol degradation rate

The degradation rate of benzene is $2.3 \cdot 10^{-8}$ s^{-1} in places where the concentrations of ethanol or acetic acid are smaller than 10^{-6} mol m^{-3} and 0 s^{-1} elsewhere. The rates of ethanol and acetic acid are $5.2 \cdot 10^{-6}$ s^{-1} and $1.6 \cdot 10^{-8}$ s^{-1}, respectively. In the case of reduced biodegradation of ethanol the rate amounts to $5.2 \cdot 10^{-7}$ s^{-1}. These data are compiled in Tab. 7.1.

The transport data are made available in Tab. 7.4. The diffusion coefficient is selected to be $1.0 \cdot 10^{-9}$ m^2 s^{-1}, whereas the dispersion lengths are 0.1 m and 0.01 m, respectively. Only benzene is sorbed. It is modelled with an Henry isotherm with k_D=0.001 m^3 mol^{-1}. At one location at (193.5 m, 193.5 m) the pollutants are released into the groundwater. Over a period of 20 y 25 kg of benzene and 25 kg of ethanol are permanently discharged annually. That implies that a total of 500 kg each contaminate the groundwater: 6 400 mol of benzene and 10 851 mol of ethanol. Acetic acid is produced only by degradation of ethanol.

Tab. 7.4: Transport parameters

	parameters		
diffusion	$D = 1.0 \cdot 10^{-9}\ m^2\ s^{-1}$		
dispersion	$\alpha_L = 0.1$ m $\alpha_T = 0.01$ m		
C_6H_6	$k_D = 0.001\ m^3\ mol^{-1}$		
CH_3-CH_2OH	k_D=0.0		
CH_3-COOH	k_D=0.0		
source location	x = 193.5 m y = 193.5 m		
C_6H_6 (benzene)	25 kg y^{-1}	500 kg = 6 400 mol	20 y
CH_3-CH_2OH (ethanol)	25 kg y^{-1}	500 kg = 10 851 mol	20 y
CH_3-COOH (acetic acid)	--	--	--

In the following figures the concentration distributions of benzene, ethanol and acetic acid are shown for 10 years and 20 years after release, except Fig. 7.9 where the temporal distribution of the degradation of benzene with and without ethanol influence is plotted. The examination point is situated 25 m downstream from the injection point.

7.3.2.1 Transport without Degradation

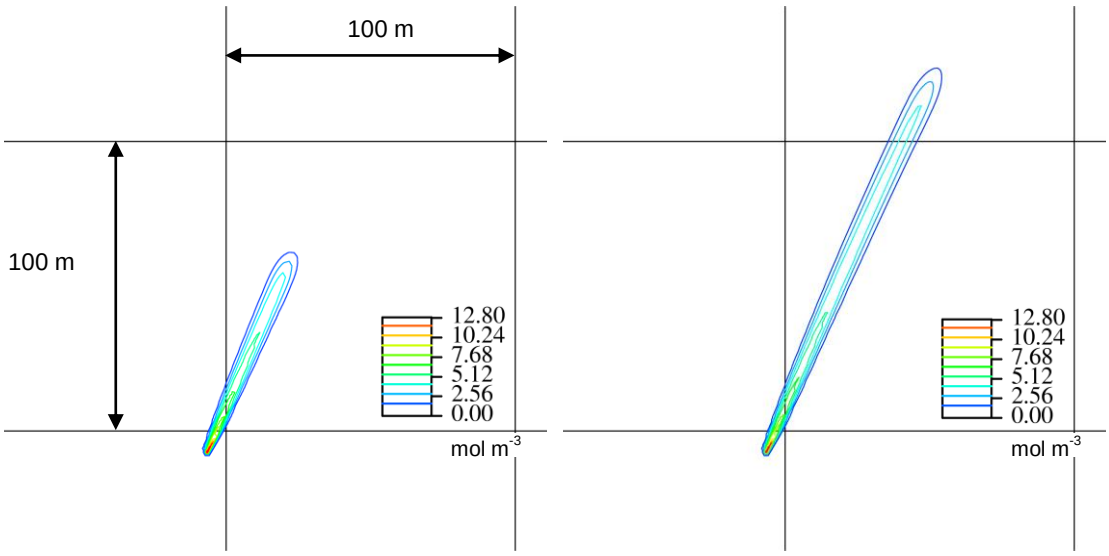

Fig. 7.4: Benzene plume after y 10 (left) and 20 y (right) without degradation
Note: The distances between coordinate lines amounts to 100 m.

In Fig. 7.1 and Fig. 7.5 the extensions of the benzene and ethanol plumes after 10 years and 20 years are depicted. It can easily been recognised that if no degradation is considered, ethanol covers a distance approximately five times larger than that of benzene. This fact is caused by the adsorption. One should pay attention to the different scales in these figures.

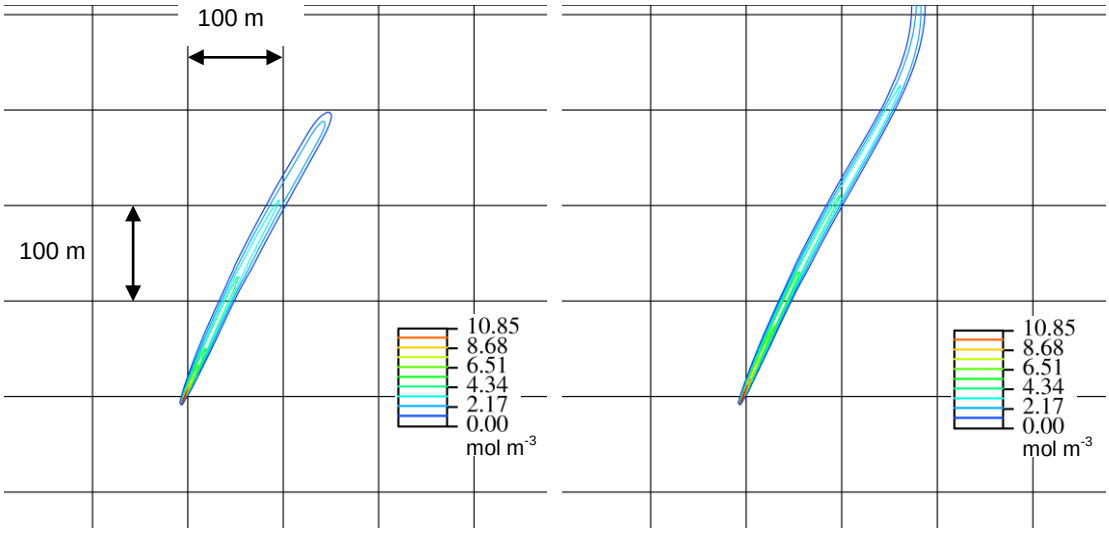

Fig. 7.5: Ethanol plume after 10 y and 20 y without degradation
Note: The distances between coordinate lines amount to 100 m.

7.3.2.2 Transport with Degradation

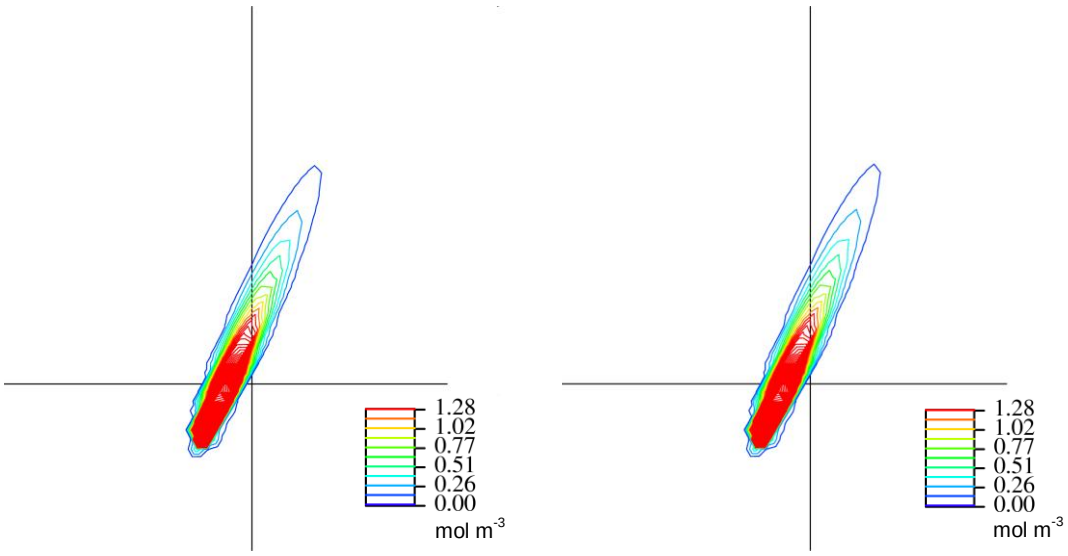

Fig. 7.6: Benzene plume after 10 y and 20 y with degradation

Fig. 7.6 shows the spatial distribution of benzene with degradation. Due to biodegradation and sorption the benzene front migrates at most around 40 m. Taking into account biodegradation ethanol degrades so fast that it is detectable only in the injection point.

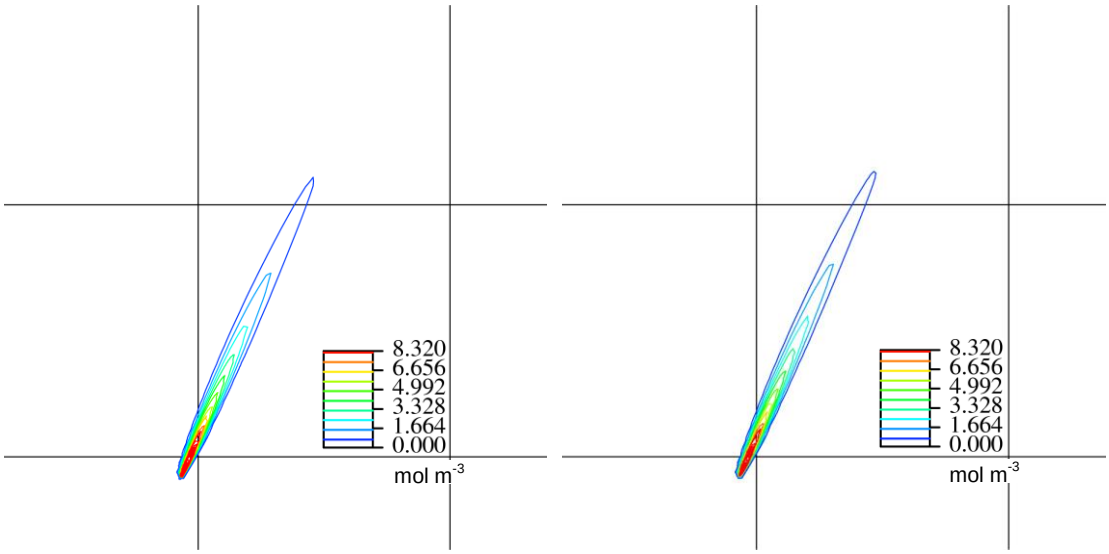

Fig. 7.7. Acetic acid plume after 10 y and 20 y with degradation

Due to degradation of ethanol the acetic acid accumulates and migrates under further degradation, but without sorption. In this case the front covers a distance of about 120 m. This is shown in Fig. 7.7.

7.3.2.3 Transport with Degradation and Interaction

In this model the interaction between presence of ethanol or acetic acid and biodegradation of benzene is taken into account. If ethanol or acetic acid are present with concentrations above 10^{-6} mol m^{-3} the degradation of benzene is suppressed.

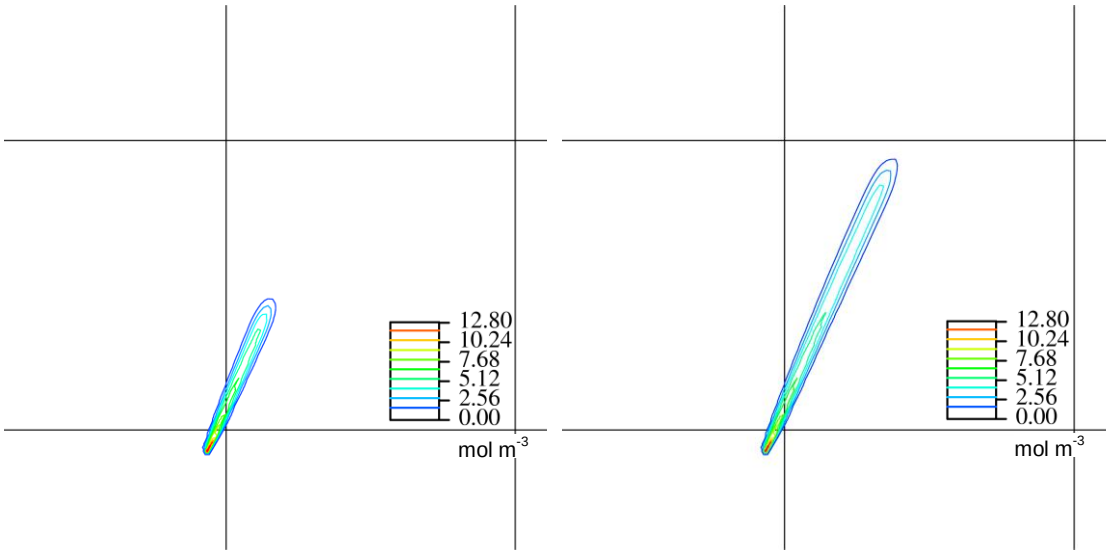

Fig. 7.8: Benzene plume after 10 y and 20 y with degradation and interaction

Fig. 7.8 shows the benzene plume after 10 years and 20 years for the case that biodegradation, sorption, and the above mentioned interaction is taken into consideration. Here the benzene front migrates about 120 m. That means that due to suppression of the biodegradation of benzene the range of coverage becomes trice as large. Fig. 7.9 depicts the temporal development of the benzene concentration at an examination point 25 m downstream the injection point. It can be seen that the benzene concentration increases about a factor of 12 if the interaction is considered.

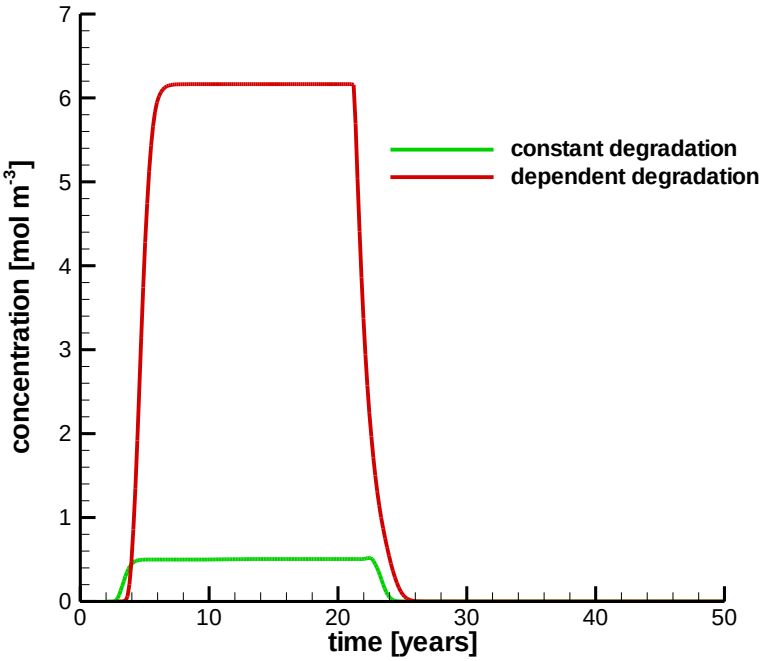

Fig. 7.9: Benzene concentration with constant and dependent degradation

7.3.2.4 Transport with Smaller Ethanol Degradation Constant

To examine the impact of ethanol degradation the simulations were repeated with a degradation constant for ethanol one order of magnitude smaller than the one used in the previous calculations. In Fig. 7.10 one can observe that the degradation constant of ethanol has almost no influence on the range of the benzene plume. This is a consequence of the specific parameter selection.

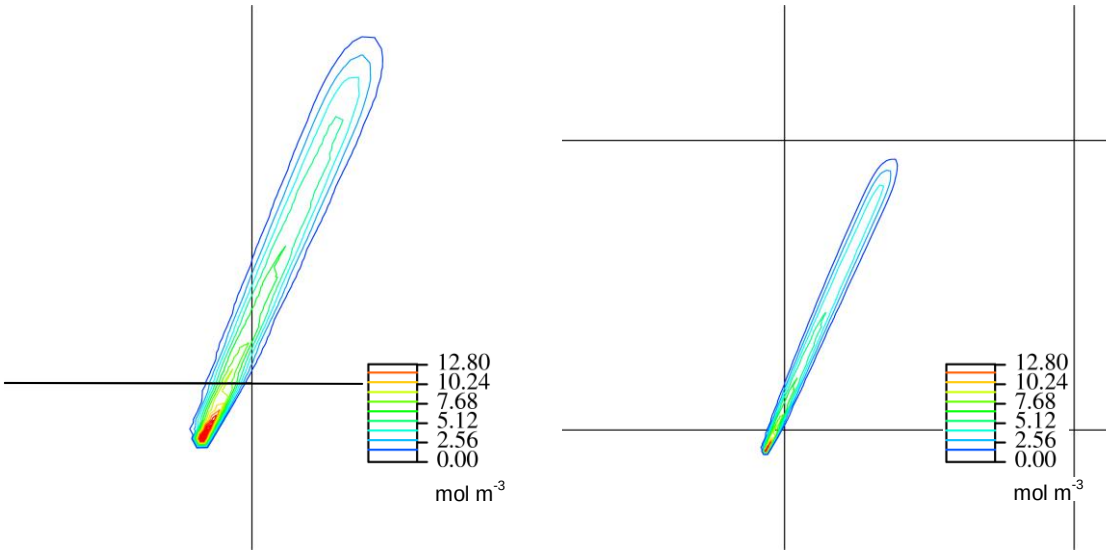

Fig. 7.10: Benzene plume after 10 y and 20 y with smaller degradation constant

Flow as well as transport computations were performed on a triangle grid with about 300 000 nodes. Version 6 of d^3f and version 13 of r^3t were used for these simulations.

7.4 Conclusions

To simulate this test case it was necessary to expand r^3t to take into considerations non-constant decay coefficients. Whereas radioactive decay is characterised by constant decay coefficients, which do not change in any environment, in biodegradation it happens that the degradation coefficients depend on the concentration of some other substances. This means the degradation coefficient may become spatially and temporally dependent. In this case the degradation coefficient of benzene becomes 0 in the presence of ethanol or acetic acid. Otherwise the coefficient has a well defined value which is constant and not equal to 0. It is understood that it is possible to assign also other functions to the degradation coefficients. By implementing this feature into r^3t the application range is enlarged to chemical degradation and biodegradation.

8 Deficiencies, their Elimination, and Improvements

On the strength of past experience we engaged the group of Prof. Wittum, University of Heidelberg, in the frame of a sub-order in the reported project. The main goal of this engagement was the correction of numerical deficiencies and errors.

Amongst others the codes d^3f and r^3t were upgraded to a new and enhanced version of the basis software UG /BAS 97/ with the intention to unify the application of the codes.

Furthermore the three-dimensional hexahedron grid was created by the Heidelberg group. For this purpose an enhancement of the grid generator was carried out. This allows for a much easier data input.

The simulation of benzene transport and the biodegradation demands a new feature of the code r^3t. In contrast to radioactive decay it is necessary to allow for decay coefficients to describe biodegradation of one substance depending on concentrations of other pollutants: This was installed into r^3t.

In order to display stochastically determined permeability fields it was needed to include a software routine which enables to write out the permeability. Subsequently one was enabled to display the results graphically.

Otherwise there existed problems with three-dimensional grid refining, the use of refined grids in simulations, and the declaration of time-dependant boundary conditions. These deficiencies were corrected in the course of this project.

Generally speaking we were strongly supported in problems with numeric, with compilers, and with installations on new computer systems, e.g. parallel computers. Moreover we got assistance when encountering badly or even not documented features of the computer codes d^3f and r^3t.

In addition a sub-order was placed to a small software house for maintenance and further development of the graphical user interfaces (gui) for both d^3f and r^3t.

9 Summary and Conclusions

With the development of the program packages d^{3}f and r^{3}t powerful tools were available to model two- or three-dimensionally density-driven flow and pollutant transport, respectively. In the course of the project some features of d^{3}f and r^{3}t were enhanced which is roughly described in the previous chapter.

Four different test cases were examined in the project MOST. Three of them were field-scaled and close to reality and the modelling was performed three-dimensionally. The fourth which was defined in a late phase of the project is based on a literature review on “Fate and Transport of Ethanol-Blended Gasoline”. This case was field-scaled too and modelled two-dimensionally.

The first test case deals with the freshwater lens below the Langeoog Island. It is one of the East Frisian Islands and is located in the Wadden Sea in north-west Germany. Only a part of 2 km × 1.4 km of the island was modelled. This part includes the Pirola Valley in the central part of Langeoog. This valley is an important area for drinking water supply and is protected against the North Sea by a belt of dunes and dykes. These dunes have often been damaged by storm tides. A three-dimensional model was set-up and the formation of the freshwater lens could be reproduced by calculations with the density-driven flow code d^{3}f. The comparison of the simulated and the measured contour lines of the freshwater/seawater interface show a sufficiently well agreement.

In the next step chloride and potassium transport were modelled using the transport code r^{3}t. In the case of chloride transport the concentrations calculated with d^{3}f and with r^{3}t can be compared directly. The results agree as expected. However, this does not basically show the correctness of the two codes, but it clearly shows the consistence of the two computer programs. Potassium transport with consideration of retardation by adsorption shows the correct delay compared with the chloride transport which is not affected by any adsorption.

Guided by the specification of the OOWV (Oldenburg-East-Frisian Water Association) a flood scenario after a seawater break through into the groundwater catchment area was taken into consideration. Since this region is protected by dunes and dikes after flooding one gets the adverse effect, these dikes hinder a fast seawater run-off after a storm tide. Under the assumption that all seawater is removed from the surface not later than 80 days after the flood event it will take about 10 years until the freshwater

lens is completely restored. Originally it was planned to consider the pumping in the Pirola Valley, too. But even reduced pumping rates provide no satisfying results. In our opinion the lacking feasibility to model free water tables is the cause of this failure of the code. The overcoming of this problem could be performed within forthcoming projects.

The next test case dealt with the modelling of pollutant transport at the Krauthausen groundwater measuring site. It is located on North Rhine Westfalia, approximately 7 km southeast from the research centre in Jülich. The site covers an area of 200 m × 70 m. The uppermost aquifer which is considered here consists of three well characterised layers with a total depth of 10 m. They are extremely heterogeneous and even anisotropic so that it is necessary to model the permeability stochastically.

Experimentally the migration of uranine, lithium, and bromide was examined. Results are given for times of 85 d, 154 d, 365 d, and 449 d after the injection mainly as horizontal plumes. Bromide was not adsorbed while uranine and lithium were retarded, whereas the adsorption was modelled with non-linear Freundlich isotherms. The parameters were fitted to batch experiments with soils from the different layers. Two-dimensional as well as three-dimensional modellings showed an acceptable agreement with the measured plumes. Recovery was about 50% or even less. The experimentally and theoretically observable diving down of the pollutants could be an indication of disappearance of tracer through the bottom of the examined test field. The bottom consists of some clay layers with thickness of decimetres which possibly contain hydraulic windows.

In the third test case the zinc transport at Cape Cod in Massachusetts, USA was modelled. About 59 years of land disposal of sewage effluents resulted in a contamination of the aquifer with zinc and other pollutants. The sewage plant was shut down in 1995. Measurements clearly exhibited a pH-dependence of the zinc plume.

The region under consideration covered an area of 400 m × 14 m and its depth was 14 m. It was assumed that the hydraulic conductivity (permeability) was homogeneous and the anisotropy factor amounted about 2. At the side of the sewage plant the inflow was identified to be 0.16 m d^{-1} whereas the recharge rate amounted to $1.4 \cdot 10^{-3}$ m d^{-1}. The other boundaries were modelled as impermeable except the outflow face where hydrostatic pressure was assumed.

The special feature of this test case was the deduction of the K_d-value from measured and geochemically modelled isotherms. On obtained K_d-values which depended non-linearly on the pH-value. In order to describe the pH-value distribution the proton transport without adsorption was simulated. Within 4 years the proton concentration became steady-state, hence one got a constant but spatially varying pH-distribution.

In contrast to the proton transport the migration of zinc was impeded by adsorption. Qualitatively the model results agreed satisfactorily with the experimental findings. They showed a wedge-shaped plume in the upper part of the examined region and a more or less uniform vertical concentration profile in the lower half.

Up to now no numerical model simulated the zinc transport very well. In so far it was not astonishing that only a qualitative agreement could be attained. But there was evidence that improvements are possible here so we were convinced that it will be feasible to get a much better matching.

The last test case concerns with gasoline additives and the biodegradation of gasoline. In order to replace lead as an octane-enhancing additive ethanol was used. Since the metabolising of ethanol is extremely fast it poses little threat to contaminate potable water. However, there exists a potential for ethanol to decrease the biodegradation of hydrocarbons like benzene. Hence the release of acetic acid during ethanol metabolism requires additional considerations. Some transport modelling was performed to predict the consequences of ethanol on the biodegradation and transport of benzene through contaminated aquifers.

Since the CFB Borden site is presumably the best-characterised sand aquifer in the world it was chosen as test case. The region of interest covered 610 m × 610 m with symmetric boundary conditions. Over a period of 20 years 25 kg y^{-1} benzene and ethanol were injected. After the extension of r^3t to account for biodegradation, i.e. to non-constant decay coefficients, three different models were examined: benzene and ethanol transport without degradation, with degradation but without interaction, and with degradation and interaction. Supplementary degradation and interaction were performed using reduced ethanol degradation constant. Interaction denoted that the degradation of benzene was inhibited if the concentration of ethanol or acetic acid was higher than 10^{-6} mol m^{-3}. The simulations showed that although the benzene concentration at a distance of 25 m downstream to the injection point decreased by a factor

about 12 with interaction the covered distance of the plume increases only by a factor about 3.

Recapitulatory the work performed within this project has shown that

- d^3f enables the modelling of density-driven flow,
- d^3f and r^3t are at least self consistent,
- d^3f enables stochastic flow modelling with subsequent transport modelling using r^3t,
- pH-dependent sorption can be modelled with r^3t, and
- r^3t enables modelling with non-constant decay coefficient (biodegradation).

All of the features listed above provided feasible results. On the other hand it was observed that wells could not be modelled as long as the depth of the modelled region was not sufficiently large. Anyway the confidence in the computer codes d^3f and r^3t is increased by these test cases.

Since some of the features of the program packages d^3f and r^3t were not yet tested, a lot of work has still to be done to qualify the codes. Further developments with respect to free water table, to heat transport and to explicit fracture modelling will tremendously enhance their field of applications.

10 References

/BAS 97/ Bastian, P.; Birken, K.; Eckstein, K.; Johannsen, K.; Lang, S.; Neuss, N.; Rentz-Reichert, H.: UG - A Flexible Software Toolbox for Solving Partial Differential Equations. Computing and Visualization in Science 1, 1, 27-40, 1997.

/BIR 00/ Birthler, H.; Fein, E.; Schneider, A.: Validierung von Einzeleffekten in Grundwassermodellen. Abschlussbericht. Gesellschaft für Anlagen- und Reaktorsicherheit (GRS) mbH, GRS-150, Braunschweig 2000.

/CIO 01/ Ciocanaru, M.; Harms, R.; Nitzsche, O., Englert, A.; Vereecken, H.: Site Characterization of the Jülicher Zwischenscholle area for the PAGASE project. Forschungszentrum Jülich, Germany, 2001.

/COA 64/ Coats, K.H.; Smith, B.D.: Dead-end pore volume and dispersion in porous media. Society of Petroleum Engineers Journal, 4 (3), 73-84, 1964.

/COR 98/ Corseuil, H.X.; Hunt, C.; dos Santos Ferreira, R.C.; Alvarez, J.J.: The influence of the gasoline oxygeneate ethanol on aerobic and anaerobic BTX biodegradation. Water Resources Research 32(7), 2065-2071, 1998.

/DAV 98/ Davis, J.A., Coston, J.A., Kent, D.B., Fuller, C.C.: Application of the Surface Complexation Concept to Complex Mineral Assemblages. Environ. Sci. Technol., 32, 2820-2828, 1998.

/DAV 00/ Davis, J.A., Kent, D.B., Coston, J.A., Hess, K.M., Joye, J.L.: Multispecies reactive tracer test in an aquifer with spatially variable chemical conditions. Water Resources Research, Vol. 36, No. 1, 2000.

/DAW 98/ Dawson, C.N.: Analysis of an upwind-mixed finite element method for nonlinear contaminant transport equations. SIAM J. Numer. Anal. 35(5): 1709-1724 (electronic), 1998.

/DÖR 97/ Döring, U.: Transport der reaktiven Stoffe Eosin, Uranin und Lithium in einen heterogenen Grundwasserleiter. Bericht des Forschungszentrums Jülich, jül-3354, 1997.

/DÖR 99/ Döring, U.; Jaekel, U.; Neuendorf, O.; Seidemann, R.; Vereecken, H.: Analysis of reactive solute transport in a heterogeneous aquifer. 3. Characterization of sorption heterogenity and its impact on solute transport. Internal Report, Forschungszentrum Jülich, 1999.

/ENG 00/ Englert, A.; Hashagen, U.; Jaekel, U.; Nitzsche, O.; Schwarze, H.; Vereecken, H.: Transport von gelösten Stoffen in Grundwasser - Untersuchungen am Testfeld Krauthausen. Grundwasser 3, 115-124, 2000.

/ENG 03/ Englert, A.: Measurement, Estimation and Modelling of Groundwater Flow Velocity at Krauthausen Test Site. Doctoral Thesis. Rheinisch-Westfälische Technische Hochschule Aachen, 2003.

/FEI 99/ Fein, E.; Schneider, A. (eds.): d^3f - ein Programmpaket zur Modellierung von Dichteströmungen. Abschlussbericht. Gesellschaft für Anlagen- und Reaktorsicherheit (GRS) mbH, GRS-139, Braunschweig 1999.

/FEI 04/ Fein, E. (ed.): r^3t - A Program Suite to Model Transport and Retention in Porous Media. Final Report. Gesellschaft für Anlagen- und Reaktorsicherheit (GRS) mbH, GRS-192, Braunschweig 2004.

/GLE 99/ Glenn, U.: The Fate and Transport of Ethanol-Blended Gasoline in the Environment. Governors' Ethanol Coalition, Lincoln, Nabraska, 1999.

/GOO 94/ Goodwin, B.W.; McConell, D.B.; Andres, T.H.; Hajas, W.C.; Le Neveu, D.M.; Melnyk, T.W.; Shermann, G.R.; Stephens, M.E.; Szekely, J.G.; Bera, P.C.; Cosgrove, C.M.; Dougan, K.D.; Keeling, S.B.; Kitson, C.J.; Kummen, B.C.; Oliver, S.E.; Witzke, K.; Wojciechowski, L.; Wikjord, A.G.: The Disposal of Canada's Nuclear Fuel Waste: Postclosure Assessment of a Reference System. AECL-10717. August 1994.

/GRA 94/ GRAPE, **GRA**phics **P**rogramming **E**nvironment, Reference Manual.SFB 256, Bonn, 1994.

/GRU 00/ Grube, A.; Wichmann, K.; Hahn, J.; Nachtigall, K. H.: Geogene Grundwasserversalzung in den Poren-Grundwasserleitern Norddeutschlands und ihre Bedeutung für die Wasserwirtschaft. Veröffentlichungen aus dem DVGW Technologiezentrum Wasser, Band 9, Karlsruhe, Germany, 2000.

/HÄF 92/ Häfner, F.; Sames, D.; Voigt, H.-D.: Wärme- und Stofftransport. Mathematische Methoden. Springer-Verlag Berlin Heidelberg New York, 1992.

/HES 99/ Hess, K.M., Davis, J.A., Coston, J.A., Kent, D.B.: Multispecies Reactive Transport in an Aquifer with spatially Variable Chemical Conditions: Dispersion of Bromide and Nickel Tracers. In: Morganwalp, D.W. und Buxton, H.T. (edts.): U.S. Geological Survey, Water-Resources Investigations Report 99-4018C, 1999.

/HÖL 05/ Hölting, B., Coldewey, W.: Hydrogeologie - Einführung in die Allgemeine und Angewandte Hydrogeologie. 6. Auflage, Elsevier, München, Germany, 2005.

/HUB 94/ Hubbard, C.E.; Barker, J.F.; O'Hannesin, S.F.; Vandegriendt, M.; Gillham,R.W.: Transport and Fate of dissolved methanol, methyl-tertiary–butylether, and monoaromatic hydocarbons in a shallow sand aquifer. Health and Environmental Science Department, API Publication Number 4601, American Petrol Institut, Washington DC, 1994.

/KEM 05/ Kemna, A.: Characterisation of Structures and Transport Processes in Aquifers Using Electrical Methods. Contribution to Workshop "EAGE Near Surface 2005", Palermo (Italy), 2005.

/KEN 99/ Kent, D.B., Abrams, R.H., Davis, J.A., Coston, J.A., LeBlanc, D.R.: Modeling the Influence of Adsorption on the Fate and Transport of Metals in Shallow Ground Water: Zinc Contamination in the Sewage Plume on Cape Cod, Massachusetts. In: Morganwalp, D.W. und Buxton, H.T. (edts.): U.S. Geological Survey, Water-Resources Investigations Report 99-4018C, 1999.

/KEN 00/ Kent, D. B.; Abrams, R. H.; Davis, J. A.; Coston, J. A.; LeBlanc, D. R.: Modeling the influence of variable ph on the transport of zinc in a contaminated aquifer using semiempirical surface complexation models. Water Resources Research 36, 12, 3411-3425, 2000.

/KIN 99/ King, Mark W.G.; Barker, James F.: Migration and natural fate of a coal tar creosote plume: 1. Overview and plume develpement. Journal of Contaminant Hydrology 39, 249-279, 1999.

/KÜH 96/ Kühle, T.; Zude, F.; Lührmann, L.: Das eindimensionale Transportprogramm CHET1 unter Berücksichtigung der Sorption nach dem K_d-Konzept. Gesellschaft für Anlagen- und Reaktorsicherheit (GRS) mbH, GRS-124, Braunschweig 1996.

/LÜH 96/ Lührmann, L.; Noseck, U.: Das eindimensionale Transportprogramm CHET2 unter Berücksichtigung nichtlinearer, elementspezifischer Gleichgewichtssorption. Gesellschaft für Anlagen- und Reaktorsicherheit (GRS) mbH, GRS-125, Braunschweig 1996.

/LÜH 98/ Lührmann, L.; Noseck, U.; Tix, C.: Model of contaminant transport in porous media in the presence of colloids applied to actinide migration in column experiments, Water Resour. Res. 34, 3, 421-426, 1998.

/LÜH 99/ Lührmann, L.: Modellierung des kolloidbeeinflussten Schadstofftransports mit dem Rechenprogramm TRAPIC. Gesellschaft für Anlagen- und Reaktorsicherheit (GRS) mbH, GRS-149, Braunschweig 1999.

/NAG 94/ Nagra: Kristallin I - Safety assessment report. Nagra Technical report 93-22. Wettingen, Juli 1994.

/NAU 05/ Naumann, K.: Eine hydrogeologische Systemanalyse von Süßwasserlinsen als Grundlage einer umweltschonenden Grundwasserbewirtschaftung. Dissertation, TU Braunschweig, Germany, 2005.

/MAC 94/ Mackay, D.; Bianchi-Mosquera, G.; Kopania, A.; Kianjah, H.; Thorbjarnarson, K.: A forced-gradient experiment on solute transport in the Borden aquifer. 1. Experimental methods and moment analyses of results. Water Resources Research 30, 2, 369-383, 1994.
Thorbjarnarson, K.; Mackay, D.: A forced-gradient experiment on solute transport in the Borden aquifer. 2. Transport and dispersion of the conservative tracer. Water Resources Research 30, 2, 385-399, 1994.
Thorbjarnarson, K.; Mackay, D.: A forced-gradient experiment on solute transport in the Borden aquifer. 3. Nonequilibrium transport of the sorbing organic compouds. Water Resources Research 30, 2, 401-419, 1994.

/NEU 96/ Neuendorf, O.: Numerische 3-D Simulation des Stofftransportes in einem heterogenen Aquifer. Dissertation RWTH Aachen, 1996.

/PAR 99/ Parkhurst, D. L.; Appelo, C.A.J.: User's guide to PHREEQC (version 2) – A computer program for speciation, batch-reaction, one-dimensional transport, and inverse geochemical calculations. Water-Resources Investigations Report 99-4259, Denver, Colorado, 1999.

/PET 03/ Petersen, J.; Pott, R.; Janiesch, P.; Wolff, J.: Umweltverträgliche Grundwasserbewirtschaftung in hydrogeologisch und ökologisch sensiblen Bereichen der Nordseeküste. Husum Druck- und Verlagsgesellschaft, 2003.

/RUM 90/ Rumpf, M.; Schmidt, A.: GRAPE, **GRA**phics **P**rogramming **E**nvironment. Report 8, SFB 256, Bonn, 1990.

/SEL 02/ Seliger, A.: Methoden zur Erfassung des regionalen Wasserhaushalts im niedersächsischen Küstengebiet am Beispiel der Insel Langeoog. Diplomarbeit, TU Braunschweig, Germany, 2002.

/SKI 91/ SKI Project-90. Volume I and II. Statens Kärnkraftinspektion Swedish Nuclear Power Inspectorate Stockholm, SWEDEN, SKI Technical Report 91:23, August 1991.

Statens Karnkraftinspektion: SKI Site-94. Deep Repository Performance Assessment Project, Volume I, SKI TR 96:36, Stockholm, Dezember 1996.

Statens Karnkraftinspektion: SKI Site-94. Deep Repository Performance Assessment Project, Volume II, SKI TR 91:23, Stockholm, Dezember 1996.

/STO 96/ Storck, R.; Buhmann, D.; Hirsekorn, R.-P.; Kühle, T.; Lührmann, L.: Das Programmpaket EMOS zur Analyse der Langzeitsicherheit eines Endlagers für radioaktive Abfälle. Version 5. Gesellschaft für Anlagen- und Reaktorsicherheit (GRS) mbH, GRS-122, Braunschweig 1996.

/SVE 92/ Svensk Kärnbränslehantering AB: SKB 91 - Final disposal of spent nuclear fuel. Importance of the bedrock for safety. SKB TR 92:20. May 1992.

/TEN 03/ Tenekoon L.; Boufadel, M.C.; Lavallee, D.; Weaver, J.: Multifractal anisotropic scaling of the hydraulic conductivity. Water Resources Research, 39(7), 1193, 2003.

/VER 99/ Vereecken, H.; Jaekel, U.; Esser, O.; Nitzsche, O.: Solute transport analysis of bromide, uranin and LiCl using breakthrough curves from aquifer sediment. J. Contaminant Hydrol., 39, 7-34, 1999.

/VER 00/ Vereecken, H.; Döring, U.; Hardelauf, H.; Jaekel, U.; Hashagen, U.; Neuendorf, O.; Schwarze, H.; Seidemann, R.: Analysis of solute transport in a heterogeneous aquifer: the Krauthausen field experiment. J. Contaminant Hydrology 45, 329-358, 2000.

/VIE 92/ Vieno T.; Hautojärvi, A.; Koskinen, L.; Nordman,H.: TVO-92 - Safety Analysis of spent Fuel Disposal. YJT-92-33 E. December 1992.

/VIE 96/ Vieno, T.; Nordman, H.: TILA-96 - Interim Report on Safety Assessment of Spent Fuel Disposal. Posiva-96-17, Helsinki, December 1996.

/WOL 98/ Wolff, J.; Müller, H.: Pilotprojekt: Ermittlung einer schonenden Bewirtschaftung der Süßwasserlinsen auf den ostfriesischen Inseln am Beispiel der Insel Norderney. Endbericht. TU Braunschweig, Germany, 1998.

/WOL 04/ Wolff, J.; Naumann, K.; Fuehrboeter, J.: Seawater break-through on Langeoog and the consequences for drinking water resources. Report, TU Braunschweig, Germany, 2004.

/ZHA 98/ Zhang, H., Schwartz, F.W., Warren, W.W., Garabedian, S.P., LeBlanc, D.R.: Simulation of variable-density flow and transport of reactive and non-reactive solutes during a tracer test at Cape Cod, Massachusetts. Water Resources Research, Vol. 34, No. 1, 1998.

Table of Figures

List of Tables

Denotation Index

In this chapter the notation which is used throughout this report and some definitions concerning concentrations are given.

l	superscript for dissolved radionuclides (liquid)
p	superscript for precipitated radionuclides (precipitated)
ad	superscript for sorbed radionuclides (adsorbed)
i	number of the radionuclide i
$k\ i$	numbers of the mothers of the radionuclide i
$e\ i$	element to which the radionuclide i belongs
s	subscript for salt
r	subscript for rock
C_i	concentration of the i^{th} radionuclide referring to the pore volume [mol m^{-3}]
σ_i	concentration of the i^{th} radionuclide referring to the pore volume [kg m^{-3}]
χ_i	mass fraction of the i^{th} radionuclide [kg kg^{-1}]
χ_s	salt mass fraction [kg kg^{-1}]

ξ_i	mass fraction of the i^{th} radionuclide within immobile pore water [kg kg^{-1}]
m_i	mass of the i^{th} radionuclide [kg]
m_r	rock mass [kg]
n_i	mol number of the i^{th} radionuclide [mol]
M_i	molecular weight of the i^{th} radionuclide [kg mol^{-1}]
ρ_f	fluid density [kg m^{-3}]
ρ_r	bulk density [kg m^{-3}]
V_{por}	pore volume = volume of the solution [m^3]
V_{rock}	rock volume [m^3]
C_i^l	concentration of the i^{th} dissolved radionuclide referring to the pore volume [mol m^{-3}]
$C_{e\,i}^l$	concentration of the dissolved element to which the i^{th} radionuclide belongs referring to the pore volume [mol m^{-3}]
C_i^{ad}	concentration of the i^{th} sorbed radionuclide referring to the rock mass [mol kg^{-1}]
C_i^p	concentration of the i^{th} precipitated radionuclide referring to the pore volume [mol m^{-3}]

G_i^l	concentration of the i^{th} radionuclide dissolved within immobile pore water referring to the pore volume [mol m^{-3}]
G_i^{ad}	concentration of the i^{th} radionuclide sorbed within immobile pore water referring to the rock mass [mol kg^{-1}]
$\boldsymbol{q}$	Darcy's velocity [m s^{-1}]
$\boldsymbol{D}^{e\ i}$	element-specific tensor of diffusion or dispersion [m^2 s^{-1}]
$\boldsymbol{D}^s$	specific tensor of diffusion or dispersion for salt [m^2 s^{-1}]
D_m	molecular diffusion constant [m^2 s^{-1}]
α_L	longitudinal dispersion length [m]
α_T	transverse dispersion length [m]
$\boldsymbol{I}$	symmetric unity tensor
$\boldsymbol{qq}$	dyadic product
λ_i	decay constant of the i^{th} radionuclide [s^{-1}]
$T_{1/2}^i$	half-life of the i^{th} radionuclide [s]
$K_d^{e\ i}$	element-specific K_d

$b = b^{e\ i}$	element-specific sorption constant of isotherm after Langmuir [m^3 mol]
$\kappa = \kappa^{e\ i}$	element-specific sorption capacity after Langmuir [mol kg]
$K_{nl} = K_{nl}^{e\ i}$	element-specific sorption constant of isotherm after Freundlich [m^3 kg]
$p = p^{e\ i}$	element-specific exponent of isotherm after Freundlich [-]
$k_{\alpha}^{e\ i}$	element-specific reaction constant for kinetically controlled sorption [s^{-1}]
ϕ	effective porosity (mobile part of aquifer) [-]
ϕ_{im}	porosity of immobile part of aquifer [-] (total porosity $= \phi + \phi_{im}$)
g	factor, which describes the distribution of the available rock surface between mobile and immobile pore space [-], $g \in 0,1$
$\alpha^{e\ i}$	element-specific exchange rate after Coats-Smith [s^{-1}]
s_f	sinks or sources of fluid [kg m^{-3} s^{-1}]
s_s	sinks or sources of salt [kg m^{-3} s^{-1}]
Q_i	sinks or sources of the i^{th} radionuclide [kg m^{-3} s^{-1}]

$\tilde{Q}_i$	sinks or sources of the i^{th} radionuclide [mol m^{-3} s^{-1}]
$\boldsymbol{n}$	unit vector normal to a surface, oriented outward
Γ	surface of a volume

Gesellschaft für Anlagen- und Reaktorsicherheit (GRS) mbH

Schwertnergasse 1
50667 Köln
Telefon +49 221 2068-0
Telefax +49 221 2068-888

Forschungsinstitute
85748 Garching b. München
Telefon +49 89 32004-0
Telefax +49 89 32004-300

Kurfürstendamm 200
10719 Berlin
Telefon +49 30 88589-0
Telefax +49 30 88589-111

Theodor-Heuss-Straße 4
38122 Braunschweig
Telefon +49 531 8012-0
Telefax +49 531 8012-200

www.grs.de

ISBN 978-3-939355-05-2